Preparation of Mesoporous Silica and Its Applications in Hydrogen Storage Materials

by

Yu Zhao

A dissertation submitted to the Graduate Faculty in Chemistry in partial fulfillment of the requirements for the degree of Doctor of Philosophy, The City University of New York

2013

This manuscript has been read and accepted for the
Graduate Faculty in Chemistry in satisfaction of the
dissertation requirement for the degree of Doctor of Philosophy.

Professor Daniel L. Akins

Date

Chair of Examining Committee

Professor Maria C. Tamargo

Date

Executive Officer

Professor Maria C. Tamargo

Professor Hiroshi Matsui

Supervisory Committee

THE CITY UNIVERSITY OF NEW YORK

Abstract

Preparation of Mesoporous Silica and Its Applications in Hydrogen Storage Materials

by

Yu Zhao

Advisor: Professor Daniel L. Akins

The present study investigated the synthesis of mesoporous silica nanospheres (MSNs) and the application of mesoporous silica in hydrogen storage applications.

MSNs with particle sizes ranging from ca. 25 to 150 nm are synthesized via sol-gel chemistry with 80 °C isothermal water bath. Initial pH values of the reactant solution were used as control parameters to tune both the particles and pores size of the products. We modified the syntheses conditions and synthesized MSNs using a microwave-assisted heating approach. The introduction of microwave-assisted heating results in better crystallized MSNs.

After enhanced hydrogen release properties of pretreated AB were study, some AB/MSN nanocomposites were prepared and the hydrogen release properties of these composites were evaluated. It was found that the AB/MSN nanocomposites had faster hydrogen release kinetics.

A critical loading level of ca.0.15 (weigh ratio of AB to MSNs) was found. When the loading level of the nanocomposites is below the critical level, the first two moles hydrogen would be released simultaneously from AB at temperature below 90 °C. Additional, the critical loading level still exists in the AB/mesoporous silica nanocomposite materials of different mesopore sizes, and their critical loading level is affected by the total surface area of the mesopores.

PREFACE

Ammonia borane (AB, NH_3BH_3) has been considered a promising candidate for chemical hydrogen storage due to its high gravimetric storage capacity (19.6 wt. %), moderate dehydrogenation temperatures (with ~13 wt. % hydrogen released below 200 °C), and being a nontoxic, nonexplosive and stable crystalline compound under normal pressures and temperatures. However, utilization of AB as an on-board hydrogen storage medium is impeded by the low rate of dehydrogenation at temperatures below 85 °C, by the formation of gaseous borazine, and by difficulty in regenerating spent AB. Several studies have discussed approaches for accelerating the rate of low-temperature hydrogen release and reducing the yield of borazine, including catalyzing the dehydrogenation over transition metals, dispersing AB in ionic liquids, and forming composites of AB with mesoporous materials. Although the dehydrogenation kinetics of AB nanocomposites is favorable at temperatures < 85 °C, and the release of the first equivalent of hydrogen is relative fast compared with pristine AB, such composites release less than 3.5 wt. % of hydrogen; while for pristine AB, release of 1 mole of hydrogen corresponds to 6.5 wt. % hydrogen—due to the additional weight of the mesoporous materials (usually about half the weight of the nanocomposites). Thus, even without considering the weight of tanks, feed lines, temperature, and pressure control equipment, etc. (which will further decrease the hydrogen storage capacity of the total system by an additional factor), nanocomposites would not be able to achieve the current U.S. Department of Energy (DOE) 2010 system target of 4.5 wt. %.

Ultimately, to meet the above target for on-board applications, it would be advantageous to tune the composition of AB nanocomposites. Nonetheless, it is unclear how the AB loading

level, also known the mass ratio of AB to matrix, affects the dehydrogenation of AB nanocomposites. Clearly, detailed information on the effect of composition is essential in designing novel AB nanocomposites for on-board hydrogen storage.

This dissertation is focused on the application of mesoporous silica in hydrogen storage. Some interesting phenomena, which have been discovered in this research project, are believed to be essential for the hydrogen storage application.

In the first chapter, we reviewed progress in synthesizing and utilization of mesoporous materials. In chapter 2, we have discussed the synthesis of mesoporous silica nanospheres (MSNs) with controlled sized using a water bath heating method. We also determined that gold nanoparticles can be attached to the surface or into the pores of as-prepared MSNs in a controlled manner, which highlights allowing material into the pores or opening the pores and allowing entry of adsorbents into the pores.

In the third chapter, we modified the syntheses conditions and synthesized MSNs using a microwave-assisted heating approach. The introduction of microwave-assisted heating results in better crystallized MSNs. A mathematical model has been proposed to predict parameters such as surface areas and pore volumes. It is suggested that the theoretical approach can also be used to evaluate the pore properties of the final product.

Before the discussion of the application of mesoporous silica nanospheres for hydrogen storage, we first discuss in chapter 4 the hydrogen release properties of ammonia borane, which is the main focus of the present dissertation. We discuss results findings that the first molar hydrogen released from AB can be enhance through a temperature pretreatment process. Using both spectroscopic and quantum chemical calculations (specifically, Gaussian computation), we

deduce that dimers of ammonia borane are formed during the pretreatment process, and that the presence of dimers may be a key factor that leads to the enhanced hydrogen release kinetics.

In chapter 5, we used the MSN sample as the host for preparation of AB-MSNs hybrid materials. It is found that in addition to enhancing hydrogen release at lower temperature, the mechanism for the reaction leads to the release of the first and second mole of hydrogen form AB at the same temperature. We have studied the phenomena, and find that a critical loading level of AB in the pores of MSN pore is applicable to the MSN samples.

In order to enhance our understanding of the thermal release properties for AB load into mesoporous silica, we have use mesoporous silica of a range of pore sizes in forming the hybrid materials. The hydrogen release properties are discussed in chapter 6.

ACKNOWLEDGEMENTS

Over the past several years I have received support and encouragement from a great number of individuals. Prof. Dr. Daniel L. Akins has been my mentor. His guidance and support have provided me an elegant way to buoyant the sea of knowledge. I would like to thank my research and dissertation committee of Dr. Maria C. Tamargo, Dr. Hiroshi Matsui, Dr. Jae W. Lee and Dr. Zhonghua Yu for their support over the past five years from proposing idea to a completed study. In addition, Professor Huijun Jiang and Dr. Shiunchin C. Wang both provided valuable statistical advice.

During the completion of projects, Prof. Jae W. Lee and Dr. Junshe Zhang have been our collaborators in the research of hydrogen storage materials. Prof Michal Kruk and Dr. Liang Cao have helped me on nitrogen adsorption/desorption measurement and they also provide me the large pore mesoporous silica materials for the hydrogen research. Prof. Ruth E. Stark and Dr. Xudong Guan have helped me on the solid state NMR measurement. Prof. Shuiqin Zhou and Dr. Ting Zhou have helped me on the dynamic light scattering measurement. There are also some colleagues have been either participate in my research or spent countless hours proofreading and listening to me talk about my research.

Finally, I want to thank my wife, Ting Zhou, who has been always supportive to both my life and career. She provides me the ultimate motivation to go forward.

Table of Contents

List of Tables

List of Figures

Chapter One: Synthesis and Application of Ordered Mesoporous Materials

1.1 What are porous materials

From a simplistic point of view, solid state materials can be considered as collections of spherical units connected by chemical bonds. Spatial cavities intrinsically exist in this picture. For example, in a closed-packed crystal lattice of solid spherical units, the cavities between the units, between which bonds exist, are generally about the size of the units themselves or even smaller, and are identified with the porosity of the material. For many porous materials, the pores are of larger size than the matrix units. In order to be considered as porous materials, the voids between the linked units have to be a void volume larger than that of a sphere of ca. 0.25 nm diameter. Zeolites, well-known porous materials, are crystalline aluminosilicates with intra-crystalline pores, which have rings formed of tetrahedral atoms (Al and Si). Typical zeolite pores have diameters in the range of 4–12 Å, and are called micropores according to the IUPAC classification. In IUPAC nomenclature, mesoporous materials are defined as porous materials with pore diameters ranging from 2 to 50 nm; while microporous materials have pores of size less than 2 nm; and the designation macroporous materials is used to describe materials with pore size larger than 50nm.[1]

The history of porous materials can be traced all the way back to 1756 when Zeolite was first discovered by the Swedish scientist Cronstedt.[2] As regards mesoporous materials, the earliest documents are patents filed as early as 1970's;[3] however, the importance of the mesoporous materials was not widely recognized until mesoporous silica were investigated by scientists in Japan[4] and at the laboratories of the Mobil Corporation in the 1990's.[5] Research activities related to mesoporous materials have grown steadily with time, principally because of

the great potential of mesoporous materials in fields such as catalysis, separation chemistry, and energy storage, to name just a few.

1.2 Synthesis of ordered mesoporous materials

Mesoporous materials can be ordered or non-ordered. However, in scientific research and many applications, ordered mesoporous structures attract more attentions due to their well-defined structures, narrow pore size distribution, and well-controlled surface area, which would provide better control and selectivity. During the past decades, significant efforts have been devoted to improving synthesis methods for controlled fabrication of ordered mesoporous structures from various materials. In order to classify different preparation methods and to categorize various preparation strategies, various approaches have been used. We discuss herein four major methods: the soft-template approach (1.2.2), the hard-template approach (1.2.3), the combined assembly via a soft and hard template approach (1.2.4), and the non-template approach (1.2.5). As necessary background knowledge for soft- and/or hard-mesoporous materials synthesis, the phase behaviour of the surfactant in the solution (1.2.1) is introduced before the discussion of the synthesis methods.

1.2.1 Phase behavior of surfactants

In order to understand the soft-template self-assembly process that leads to the formation of mesoporous structures, it is vitally important to understand aggregation behavior of surfactants in solution. Here, surfactants are usually organic compounds that are amphiphilic, containing both hydrophobic groups and hydrophilic groups. The phase behavior of surfactants depends on the specific aqueous or oil solutions they were dispersed in. In this section, a simple

surfactant-water binary system[5] has been used as an example to discuss the phase behavior of surfactants.

The limit of solubility of a surfactant is called its critical micelle concentration (CMC). When a surfactant is dispersed in water above its aqueous CMC, it generally aggregates into one of four types of structures: the isotropic micellar phase, the liquid crystalline hexagonal, lamellar, or cubic phases. The actually micellar phase depends not only on the concentration of the surfactant, but also on the geometry and concentration of the surfactant. When the concentration of surfactant increase further above the CMC, there will be changes in aggregate or phase structure. The phase structure formed upon increasing surfactant concentration generally follows a well-defined sequence (including a 'mirror plane' through the lamellar phase; schemes shown in Figure 1.1), such that low concentration phase structures can be considered to be 'oil-in-water', while reverse structures are regard as 'water-in-oil'.

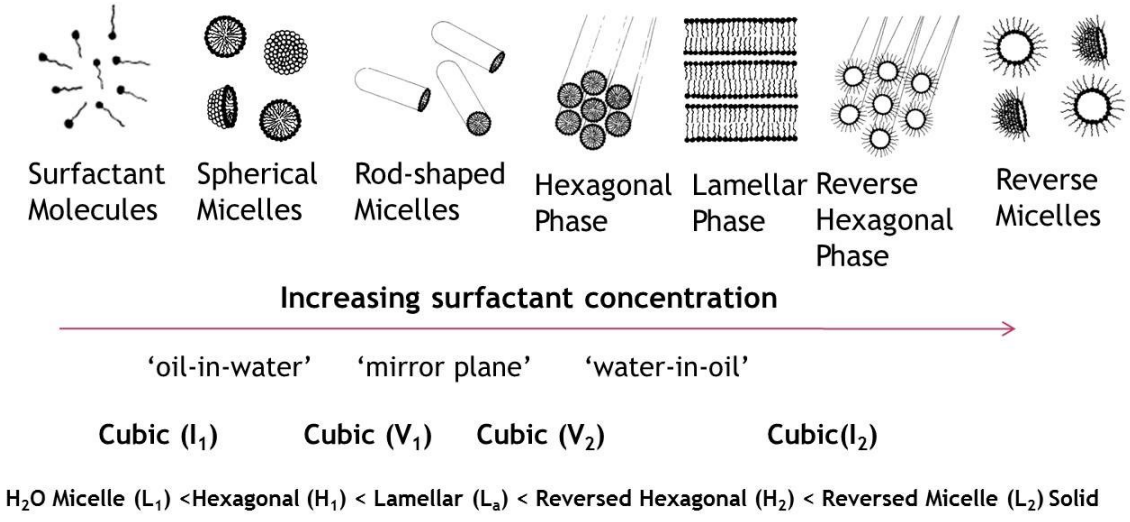

Figure 1.1 Idealized phase sequence in a surfactant-water system.[5]

Most surfactants, however, exhibit only a portion of this sequence, depending on the aggregate type initially formed at the CMC and the resulting inter-aggregate forces experienced. It is to be noted that although the same phase structures can be observed in other non-aqueous polar solvents the sequence of phases is sometimes very different and appears to depend both upon the molecular geometry and the nature of the polar head-solvent interactions. Also, some non-equilibrium and modified surfactant phases, such as vesicles and polymerized aggregates, can be formed in the solutions, which might not be good for the formation of ordered mesoporous structures.

1.2.2 Soft-template approach

The soft-template approach is developed first in the synthesis of ordered mesoporous silica. "Soft" herein infers to the status of template materials during the process—no pre-existing mesoporous structure served as template—instead of after dissolving, crosslinking or co-precipitated processes, i.e., dynamic 'soft' mesostructures will form and serve as template. Some soft-template synthesis examples are discussed here.

1.2.2.1 Surfactant-template method

In the surfactant mediate method, surfactants are dispersed in the solution and form surfactant micelles with certain liquid crystal phases. In the synthesis, these micelles will serve as templates, and also as catalyst for hydrolysis and polymerization in the case of mesoporous silica preparation.[6] Beck *et al.*[7] proposed a liquid-crystal templating (LCT) mechanism for the synthesis of MCM-41. In the LCT mechanism, surfactant micelles, instead of individual molecules and/or ions, serve as the template. After calcination of the precipitates, the final

products are inorganic frames with ordered mesoporous structures, where the mesoporous structure and mesopores derive from the form originally assumed by surfactant micelles. According to this mechanism, the condensation of silicate is not a dominant factor in determining the mesoporous structure.

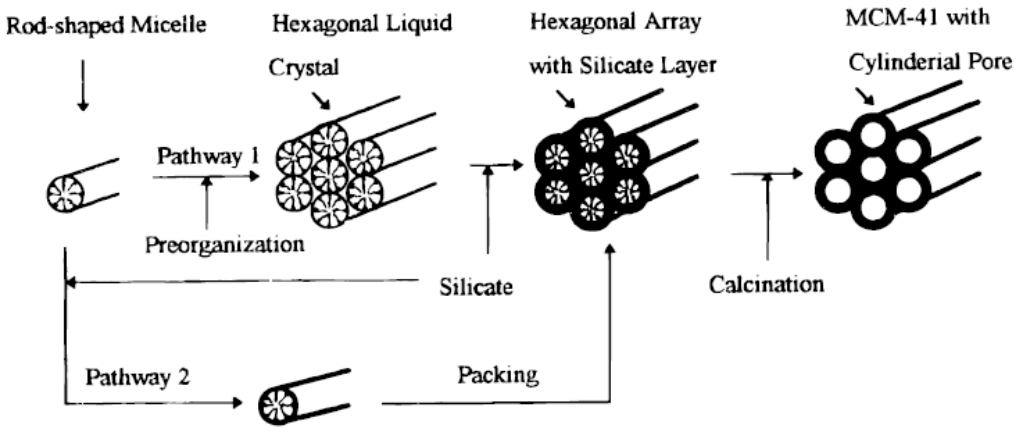

Figure 1.2 Schematic model of LCT mechanism via two possible pathways.[2]

Figure 1.2 schematically shows the structure formation process in LCT mechanism. Gel with mesostructures can form through two possible pathways: (1) the liquid crystal phase of the micelles form in the solution prior to the addition of silicate species; (2) when the silicate species added to the solution, the condensation of silicate may influence the isotropic rod-like micelles to form the liquid crystal phase. Therefore, the structure and morphology of the final mesoporous materials may large depend on the liquid crystal micelles initially formed in the solution.

In order to test the LCT mechanism, Beck *et al*.[7] used surfactants of different chain length, and auxiliary organic agents to prove the role of surfactant in the formation of the mesostructures. It is determined that, if quaternary ammonium surfactants ($CH_{2n+1}(CH_3)_3N^+$) with different alkyl chain lengths (n = 8, 9, 10, 12, 14, 16) were used in the synthesis, the longer chain surfactants will lead to a final product of larger pore size. On the other hand, since the

auxiliary organic agent, mesitylene (MES), can be dissolved to the hydrophobic regions of micelles, when it was added to the reaction aqueous solution, it expands the size of the micelle, so as to increase the pore size of final product. The influence both alkyl chain length and the addition of mesitylene (MES) on the pore size supports the LCT mechanism. Moreover, the method of fine tuning the pore size of the ordered mesoporous materials can be easily deduced from this experiment.

The LCT mechanism fails to apply under the conditions that Monnier *et al.*[8] conducted the reaction, for which the pH ranged from 12 to 14 and silicate concentration ranged from 0.5 to 5%; the explanation being that the surfactant alone does not form a liquid crystal phase and silicate does not condense. Nonetheless, mesoporous silica was still formed. So Monnier *et al.*[8] proposed the phase transformation (PT) mechanism (Figure 1.3).

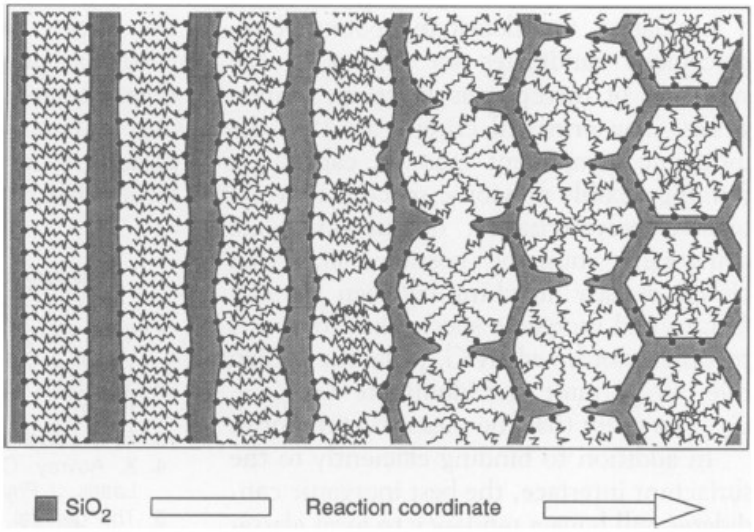

Figure 1.3 Schematic diagram of the mechanism proposed for the transformation of a surfactant-silicate system from the lamellar to the hexagonal phase.[8]

In the PT mechanism, the lamellar surfactant-silicate sheets are first formed in the solution when silicate is condensed in the solution, and the lamellar-to-hexagonal transformation

occurs when the silicate further condenses, which leads to an increase in interfacial area that is achieved through corrugation of the former lamellar sheets. Finally, this corrugation leads to the connection between the sheets, and the hexagonal mesostructure is formed. Theoretically, it is also possible to accommodate the change with tilting the surfactant hydrocarbon chains and maintaining the planar structure. But this kind of transition is entropically not favored and should not occur in the reaction. During the phase transition process, no defined liquid crystal phase for the micelle is required. Instead, the micellar assembly of the organic surfactants will be converted to the inorganic silicate.

Some other mechanisms have also been considered to apply in the synthesis of mesoporous silica.[2] But whatever the mechanism, it is common that in the formation process of mesoporous silica, that the mediation of surfactants plays important roles. Through the mediation of surfactants, silica can be aligned into a variety of mesoporous forms. Huo *et al.*[9] reported a generalized strategy toward the synthesis of ordered mesoporous metal oxides. The mesostructures can be synthesized either by direct pathways or mediated pathways (as shown in figure 1.4), using different charged surfactant molecules and inorganic solutions species for certain pH conditions.

Route 1 involve the direct co-condensation of anionic an inorganic species with a cationic surfactant (S^+I^-); examples include the synthesis of mesoporous silica such as MCM-41 and MCM-48. It is to be noted that lamellar and hexagonal WO_2 mesostructures, and cubic and hexagonal Sn_2O_5 mesostructures have also been synthesized via this route, after adjust the pH to tune the charge density of the metal polyanions.

Route 2 can be used to prepare non-silica structures in a charge-reverse situation involving cooperative condensation of a cationic inorganic species and an anionic surfactant (S^-

I^+). For example, in the synthesis of iron oxide and lead oxide mesostructures, hexagonal phase and lamellar phase can be formed by using n-hexadecane sulfonate ($C_{16}H_{33}SO_3H$) as surfactant.

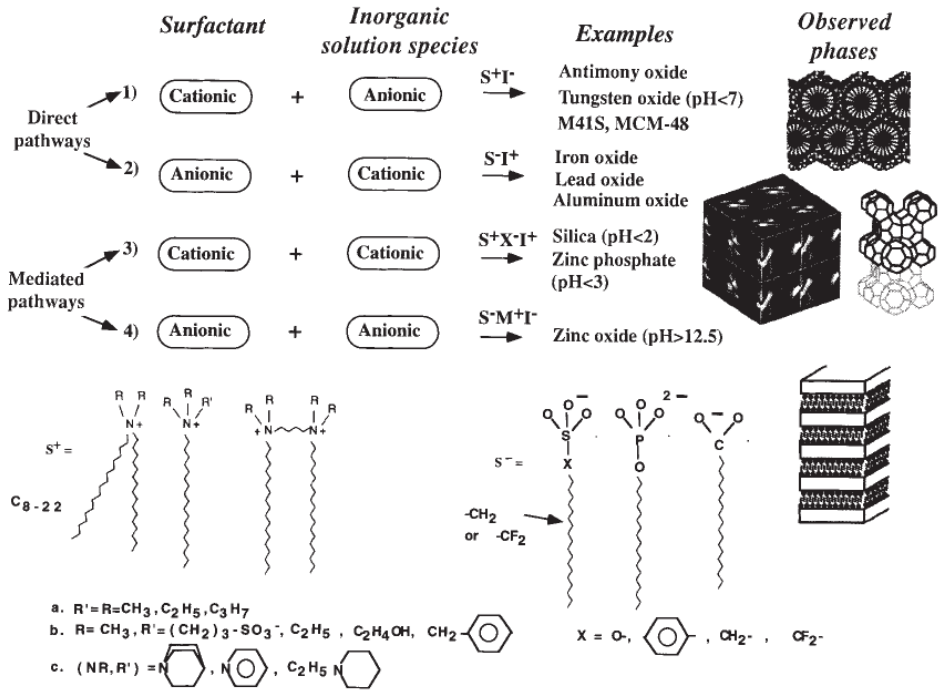

Figure 1.4 A general scheme for different surfactant and inorganic species to form mesostructures via surfactant-mediate template method[9].

In contrast with route 1 and 2, route 3 and 4 involve condensation of ionic inorganic species in the presence of similar charged surfactant molecules. These pathways are mediate by counter ions of opposite charge to that of the surfactant head group. Examples include the formation of zinc phosphate from lamellar $(C_nTMA)^+X^-[HZnPO4]$ (X^- is Cl^-, Br^-) phase and formation of ZnO from $CH_3(CH_2)16COO^-M^+[Zn(OH)_3]^-$ ($M = Na^+, K^+$).

1.2.2.2 Supramolecular self-assembly method

Besides the use of molecular surfactant, block copolymers are also good candidates as structure directing agents because of their mesostructural ordering properties and amphiphilic character. The first reported large-pore ordered mesoporous silica (SBA-15) was synthesized by Zhao *et al.*[10] via a supramolecular self-assembly method. Instead of the commonly used ionic molecular surfactant, non-ionic amphiphilic triblock copolymer, poly(ethylene oxide)-poly(propylene oxide)-poly(ethylene oxide) (PEO-PPO-PEO) was used to direct the organization of polymerizing silica species. With the mediation of block copolymer, the pore size of the hexagonal mesoporous silica can be as large as 300 angstroms.

Supramolecular self-assembly methods utilized a wide range of block copolymers to organize mesostructured composite solids. By controlling the function groups and structure of amphiphilic block copolymers, the interactions between the inorganic and organic species can be rationally adjusted. Such interactions can drive inorganic-organic assembly and organic-organic assembly to form frameworks, which provides more control in the self-assembly process than do low-molecular weight surfactants.

Yang *et al.*[11] successfully extend the supramolecular self-assembly method to the synthesis of ordered, large-pore mesoporous metal oxides, including TiO_2, ZrO_2, Al_2O_3, Nb_2O_5, Ta_2O_5, WO_3, HfO_2, SnO_2, and mixed oxides $SiAlO_{3.5}$, $SiTiO_4$, $ZrTiO_4$, Al_2TiO_5 and ZrW_2O_8. These materials are formed through a mechanism that combines block copolymer self-assembly with complexation of the inorganic species, where amphiphilic poly(alkylene oxide) block copolymers was used as structure-directing agents in non-aqueous solutions for organizing metal-oxide species.

1.2.3 Hard-template approach

The "hard-template" approach is a straightforward preparation strategy in which the growth of a "guest" will be restricted to the surface, cages, channels, and substrate of the mesoporous "host". Ideally, the final products will perfectly replicate the structure and morphology of the host materials. In practical synthesis, the inorganic precursors are filled with mesoporous silica or replicated carbon templates, which is removed at the end of preparation to provide void mesopores in the final products. The advantage of the hard template approach is the product will allow heat treatment at elevated temperatures without structural collapse, so highly crystalline materials can be obtained.

The first example of ordered mesoporous carbon retaining the structural morphology of silica template was reported by Jun *et al*.[12]. The mesoporous carbon materials, CMK-3, were synthesized using mesoporous silica SBA-15 as templates and sucrose as the carbon source. The ordered structure of the CMK-3 carbon is exactly an inverse replica without involving structural transformation during the removal of the silica template. Further research have been conducted byYu *et al.*[13], using SBA-15 nanorods as the template, it is found that the carbon replica CMK-3 will not only keep the phase structure, the morphology of the carbon mesostucture are also nanorods of the similar size.

Using mesoporous carbon CMK-3 as template, Roggenbuck *et al.*[14] successfully prepared ordered mesoporous magnesium oxide (MgO). It is found that the as-prepared mesoporous MgO has the same phase structure of the original mesoporous silica material, and showed excellent thermal stability, which is good for potential applications. Jiao *et al.*[15] also use mesoporous carbon as a hard template in syntheses, they obtained mesoporous Fe_3O_4 and Fe_2O_3 with mesoporous structures, and further investigation showed that the pore wall could be crystallized

after processing. The crystallized wall was also achieved in the synthesis of mesoporous copper oxide (CuO) by the hard template method of Lai *et al.*[16]

1.2.4 Combined assembly of soft- and hard-template (CASH) approach

The combined assembly by the soft- and hard-template (CASH) approach is basically derived from the soft template method, with the soft template converted to a hard template by a high temperature crystallization process before removal. The CASH method is as an effective method to synthesize thermally stable and well-ordered crystalline mesoporous transition-metal oxides directly. Lee *et al.*[17] first designed this method to prepare mesoporous metal oxides with crystallized walls. The process is schematically shown in figure 1.5. The first step is a supramolecular self-assembly, where the block copolymers with sp^2-hybridized carbon-containing hydrophobic block is used as structure-directing agents. Then, the heat treatment, under an inert environment, converts the copolymer to a sturdy, amorphous carbon material. This carbon material is strong enough to serve as a hard template, keeping the pores of the oxides intact while crystallizing at temperatures as high as 1000 $^{\circ}$C. In the end, the carbon template can be removed by heating the material in air, and highly crystalline ordered mesoporous transition-metal oxide, in this case N_2O_5 and TiO_2, are formed.

The key to the CASH method is the double functional character of the block copolymer; an example of which is the amphiphilic diblock copolymer poly(isoprene-block-ethylene oxide) (PI-b-PEO). PEO decomposes easily upon heating, while PI, with two sp^2 carbons per monomer unit are more thermally stable, and can be converted to a sturdy, amorphous carbon material when heat treated under an inert environment. The resultant carbon structure finally acts as a

rigid support to the mesostructured oxide walls, preventing collapse when heat treated to temperatures required for obtaining highly crystalline materials.

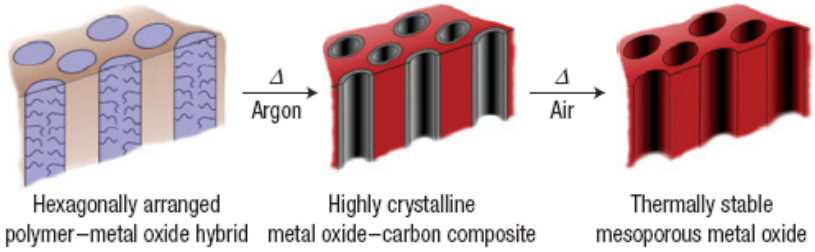

Figure 1.5 Schematic representation of CASH method.[17]

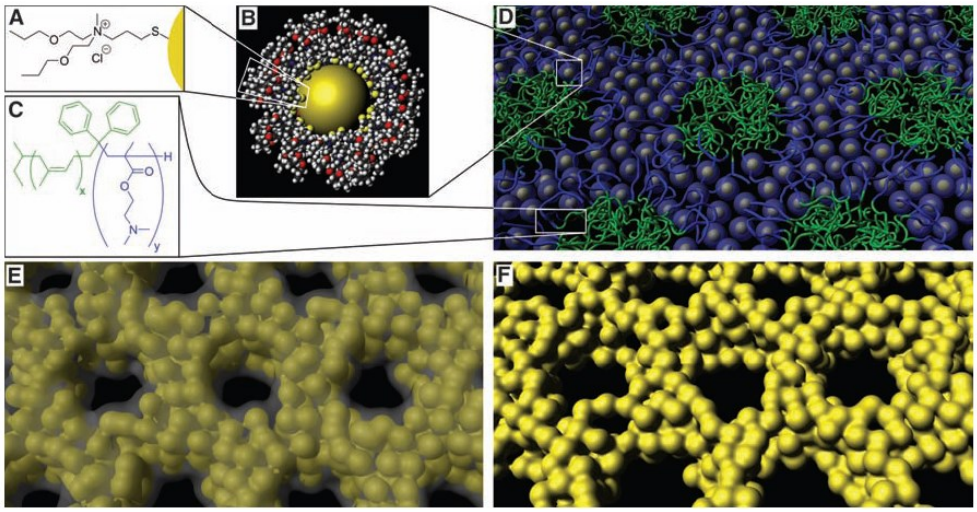

Figure 1.6. Illustration of Platinum mesoporous structure produced after each stage of the synthesis.[18]

Warren *et al.*[18] extended the strategy for preparation of metallic mesoporous materials using the block copolymer poly(isoprene-blockdimethylaminoethyl methacrylate) (PI-b-PDMAEMA). As illustrated in figure 1.6, ligand-stabilized Pt NPs (Fig. 1.6A and B) can co-assemble with block copolymers (Fig. 1.6C) during the evaporation of organic solvents. The intermediate products are metal-rich NP-block copolymer hybrids (Fig. 1.6D) with

mesostructures. These hybrids were then pyrolized under an inert atmosphere to form ordered mesostructured Pt-C composites (Fig. 1.6E). Finally, the carbon can be removed through use of an Ar-O plasma or by way of acid etch to produce ordered mesoporous Pt (Fig. 1.6F). Because polymer-NP interactions are largely mediated via the nanoparticle ligands in this method, the present approach are extendable to other metals for which similarly sized ligand-stabilized NPs can be synthesized. Thus, it is possible to prepare ordered mesoporous metals of other elements, disordered alloys, or even ordered intermetallics.

1.2.5 Non-template approach

Although templates are really important in most synthesis to the formation of ordered mesoporous structures, there are also some synthetic strategies that do not employ template materials. These synthetic methods are either utilize the properties of some special materials or depended on special technics, as indicated below.

1.2.5.1 Electrochemical anodic oxidation

Porous alumina membrane can be produced by means of electrochemical anodic oxidation of high purity aluminum foil.[19] A typical membrane preparation can be summarized as follows: aluminum foil (A99) is first treated in a water solution of 2% CrO_3 + 4.5% H_3PO_4, then anodic oxidation is performed by using oxalic solution 3% (w/w) under bias voltage. After the reaction, the anodic alumina film will separates from the aluminum electrode by immersed in a solution of $HClO_4$ (72% w/w) and $(CH3CO)_2$ (98%) 1:1 and application of a voltage of 15V for 1 to 3 seconds, during which the barrier layer would be removed from the film. An open pore membrane finally is formed. In the constant voltage anode oxidation process, the larger the

voltage applied, the larger the pore diameters achieved. The pore size of porous alumina can be as large as several hundred nanometers, but by controlling of the experimental conditions, mesos-sized alumina containing from 5 to 50 nm tubular pores can be achieve, and the pores are formed aligned in a 2d hexagonal pattern.

1.2.5.2 Spontaneous self-assembly

In many chemical processes, even without a structure directing agent, the packing of the microcrystals and/or nanoparticles or the etching on the surfacing of the bulk materials will provide some mesoporous structure. In most of the cases, the spontaneously formed mesostructures are randomly orientated. But there are some special conditions with proper environmental control in which ordered mesopores can be formed.

In the preparation of hierarchically structured alumina, Deng *et al.*[20] found that the alumina particles that were prepared had parallel arrays of macropores interconnected with mesopores. In order to clarify the role of surfactant in their synthesis, alternate surfactant were used to investigate synthesis processes. It was determined that the mesostructures do not correlated to the choice of surfactant. The mesopores were not created by a template of the surfactant, instead nanoparticle assembly of alumina would be the reason for the formation of the mesostructures.

Yuan *et al.*[21] reported a special strategy for synthesizing ordered mesoporous NiO/carbon nanotubes (CNTs) composites without use of a template and surfactant. They utilize poly (sodium-4-styrene sulfonate) (PSS) functionalized CNT to oriented growth of $Ni(OH)_2$ along the CNTs. Then after calcination the $Ni(OH)_2$/CNTs precursor, NiO nanoparticles with quadrate morphology with a length of 50-70 nm and a width of 30-60 nm were achieved. High

magnification TEM images clearly demonstrate that the NiO phase has ordered mesoporous channels of ca. 3-4 nm diameter.

Recently, Xue *et al.*[22] reported an ordered mesoporous zeolite LTA via a template-free synthesis method. The synthesis is based on the incorporation of the hydrophobic moiety of organosilane into the framework of zeolite through a Si–C covalent bond; the presence of the Si–C covalent bonds hindered the growth of the zeolite crystal in the Si-C bonded direction. As a result, defects were generated inside the zeolite crystals and are converted into meso-channels and intracrystalline nano-cages after calcination. The final product mesoporous zeolite LTA has nano-cages of 3 nm interconnected to each other through 0.8-1.2 nm channels.

1.3 Application of ordered mesoporous materials

Ordered mesoporous materials are of interest in many fields due to their large surface area, well-defined pores size, and periodical framework structures. There are already some industrial applications, and more are under development, that utilize ordered mesoporous materials in next generation applications and devices. Here, some typical applications are presented as examples.

1.3.1 Catalysis

One of the most popular applications of the mesoporous materials is in field of catalysis. The application of ordered mesoporous materials in catalysis occur from two different arenas: mesoporous catalyst materials and mesoporous support materials.

1.3.1.1 Mesoporous catalyst materials

In the traditional heterogeneous catalysts applications, the catalysts with larger surface area will provide better catalysis activities. When the catalysts is fabricated into the mesoporous framework, the large and specific surface area of the catalyst undoubtly improves the catalytic activities.

Takahara *et al.*[23] synthesized mesoporous Ta_2O_5 and used it as a photocatalyst. Although the pore wall of mesoporous Ta_2O_5 is amorphous, the photocatalytic activity achieved was still higher than that of the crystallized Ta_2O_5. Recently, Noda *et al.*[24] synthesized mesoporous Ta_2O_5 with crystalized wall. It was found that by changing the solid phase structure from amorphous to crystalline the photocatalytic activity in water decomposition improved by nearly 1 order of magnitude.

Yang *et al.*[25] reported the synthesis of mesoporous vanadium oxide and used it as the catalyst for liquid-phase selective oxidation of diphenylmethane to benzophenone in acetic acid. It is found that mesoporous vanadium oxide catalyst exhibits better catalytic performance than bulk V_2O_5 in selective oxidation process.

Tagusagawa *et al.*[26] synthesized several mesoporous Ta_xW_{10-x} mixed oxides and compared them as potential solid acid catalysts. It is found that the acid strength increased with addition of W for mesoporous Ta_xW_{10-x} oxides, and mesoporous Ta_3W_7 oxide exhibited the highest acid catalytic activity for the Friedel−Crafts alkylation of anisole and the hydrolysis of disaccharides. The mesoporous structure shows an advantageous environment for the strong acid sites comparing with nonporous Ta_2O_5-WO_3, $HTaWO_6$ nanosheets and a range of conventional solid acid catalysts, which may be due to of the high surface area and ease of reactant accessibility via the mesoporous frameworks.

1.3.1.2 Mesoporous support materials for catalyst

As mentioned earlier, another application of mesoporous materials in the catalysis field is as a support for catalysis materials. In order to improve the efficiency and reduce the use of expensive catalyst, several methods have been developed to support the catalysis on mesoporous frameworks. In the framework substitute method, the catalyst materials are co-precipitated with the mesoporous material in the synthesis. The final framework will contain a highly distributed catalytic species.

Chaliha *et al.*[27] modified the mesoporous MCM41 by incorporation of Mn(II). The mesoporous Mn-MCM41materials successfully acted as a catalyst for oxidation of phenol, 2-chlorophenol, and 2-nitrophenol in water with H_2O_2. Samuel *et al.*[28] synthesized several tin-modified mesoporous materials and studied the catalytic activity of these mesoporous materials in the Meerwein–Ponndorf–Verley reduction of carbonyl compounds. The comparison of catalytic activities of tin-containing mesoporous materials indicates that MCM-41provides better catalytic results than the other supports like MCM-48 and SBA-15.

Surface modification is also used to disperse catalysis materials into mesoporous frameworks. In this method, the mesoporous materials are first functionalized with designated functional groups, and then the catalytic materials are immobilized by the functional group on the surface. Lee *et al.*[29] claimed that immobilization of catalytic metal ion $(VO)^{2+}$ on a functionalized surface has the advantages of better control of available reactive sites and site isolation. They first functionalized mesoporous silica MCM-41 with 3-aminopropyltrimethoxysilane (APTS); the amino groups of the mesoporous MCM-41 solids were then used to immobilize $(VO)^{2+}$ ions. This anchored vanadium complexes were found to

show even better catalytic activities and higher stability than the framework-substituted V−MCM-41 materials in the catalytic oxidation of benzene.

Surface modifications of supported catalysis on mesoporous materials can further improve the catalysis activities. Brutchey *et al.*[30] first introduced site-isolated Ti(IV) centers onto the surface of a mesoporous SBA-15, then a series of (*N*,*N*-dimethylamino)trialkylsilanes, Me_2N-$SiMe_2$(R) (where R = Me, ^{n}Bu, or ^{n}Oc) were used to modify the former surface Si-OH/Ti-OH sites of the Ti-SBA-15 catalysts. Compared with the unmodified catalysts, the surface-modified catalysts were more active in the oxidation of cyclohexene with H_2O_2 and exhibited a significantly higher selectivity for cyclohexene oxide formation.

Corma *et al.*[31] studied the hydrogenation activity of Pt supported on mesoporous MCM-41 samples. Compared with Pt supported on a mesoporous amorphous silica-alumina (MSA) and other conventional supports, such as commercial amorphous silica-alumina (ASA), zeolite USY, γ-alumina, and silica, the two mesoporous MCM-41 and MSA materials have very high surface areas allowing for better dispersion of the Pt particles, and they showed a superior overall hydrogenation activity for hydrogenation of naphthalene as compared to the other supports.

In electrochemical applications, the catalysts are supported on conductive materials. Su *et al.*[32] used ordered graphitic mesoporous carbon (GMC) as the support for Pt catalyst in room-temperature methanol oxidation. The catalytic performance of the mesoporous carbon supported Pt was compared with that of commercial Pt catalyst from E-TEK. It was found that the specific activity of the Pt catalyst supported on the mesoporous carbon is improved.

Qi *et al.*[33] studied the performance of Pt/Ru catalyst also using GMC as the support, and comparison was made for Vulcan XC-72 as the support. The results indicated that the electrochemical activity of the PtRu/GMC for the methanol oxidation reaction (MOR) is higher

than that of the PtRu/XC in both half-cell and single-cell measurements. Also, a 1500 h stability test of a single cell suggests that the PtRu/GMC has excellent stability.

1.3.2 Sorption and separation

Ordered mesoporous materials have unique properties including a highly regular structure, uniform pore sizes and a high surface area, thus offering potential for separations based on size exclusion and targeted surface chemistry

Ordered mesoporous materials can be applied as an adsorbent since it exhibits both hydrophobic and hydrophilic character depending upon the framework composition and surface modification. Moura *et al.*[34] reported the adsorption of aromatic compounds such as benzene, toluene, o-, and p-xylenes (BTX), under both column and batch processes, by periodic mesoporous organosilica (PMO). It is found that the adsorption capacity decreases in the order benzene > o-xylene > p-xylene > toluene. Absorption results indicate the prospect of applying PMO for the removal of BTX from aqueous solution.

Kisler *et al.*[35] investigated mesoporous molecular sieves for the separation of biological molecules. Adsorption experiments involving proteins (lysozyme and trypsin) and a vitamin (riboflavin), as model biological solutes, have been conducted to assess the potential of MCM-41 and MCM-48 as selective adsorbents. The results demonstrate the potential of these materials for use in size exclusion separations.

Eliseev *et al.*[36] proposed a separation technique based on the size-selective adsorption of nanoparticles by mesoporous silica sieves. The system provides a narrow size distribution of PbSe nanocrystals incorporated into the pores.

Mekawy *et al.*[37] designed mesoporous silica hybrid membranes for precise size-exclusive separation of silver nanoparticles (AgNP). In the membranes, the hexagonal mesoporous silica materials are vertically aligned in the anodic alumina membrane (AAM) channels with a predominantly columnar orientation, and hydrophobic trimethylsilyl (TMS) groups were grafted onto the inner pores of the mesoporous silica hybrid AAM. The immobilization of the TMS groups allowed the columnar mesoporous silica inside AAM to retain this inner pore order without distortion during the separation of solution-phase AgNPs in organic solvents that may cause tortuous-pore membranes. These mesoporous TMS-silicas inside 1D AAM channels were found to be applicable as a size-exclusive separation system to isolate organic solution-phase AgNPs of uniform morphology and size.

1.3.3 Optics

Konjhodzic *et al.*[38] investigated the properties of the mesoporous silica films synthesized by dip-coating in evaporation-induced self-assembly. A strong dependence of the formed structure on the processing conditions, especially humidity, has been revealed allowing an appreciable structure tuning. At low humidity conditions, crack-free, transparent, thermally stable, smooth, low refractive index films formed and they can be used as optical waveguide supports.

Fiorilli *et al.*[39] synthesized mesoporous silica SBA-15 impregnated with Reichardt's dye. The composite is white if still covered with hydroxyls, while a pink coloration is observed by exposing the sample to NH_3 and primary amines. The process is fully reversible. Such systems are applicable as possible ammonia sensors.

Balaji *et al.*[40] reported a low cost, solid optical sensor for the rapid detection of low concentrations of Hg^{2+} in aqueous media based on monolayer functionalized mesoporous silica. The detection is based on the color change of TPPS from orange to green as a result of the formation of a charge-transfer complex with Hg^{2+}. The lower detection limit observed for Hg^{2+} concentration is 1.75×10^{-8} mol dm^{-3}. The material exhibits good chemical and mechanical stability, and did not show any degradation of TPPS for a period of eight months.

1.3.4 Drug delivery

Vallet-Regi *et al.*[41] have reported that MCM-41 is capable of accepting and releasing organic compounds. As an example, the uptake of ibuprofen can be investigated in the MCM-41 mesopores when the MCM-41 was immersed into the hexane solution of drug. And when the ibuprofen-loaded samples are immersed into a simulated body fluid, drug can diffuse out of the pores.

Many drug-candidates coming from drug discovery efforts suffer from poor water solubility. An insufficient dissolution of the mostly hydrophobic drugs in the gastrointestinal fluids strongly limits the oral bioavailability. Ordered mesoporous silica shows potential to boost the *in vitro* and *in vivo* dissolution of poorly water soluble drugs. Lu *et al.*[42] incorporated the hydrophobic anticancer drug, camptothecin, into fluorescent mesoporous silica nanoparticles. The particles successfully delivered the drug to various cancer cells to induce cell death. The results suggest that this method can overcome the insolubility problem of many anticancer drugs, which is considered to be one of the major challenges in cancer therapy.

Besides utilizing pore size and electrostatic interactions for controlled release of drugs, scientists, recently, have developed more complex systems in which stimuli responsive capping

agents, supramolecular assemblies, or polymers are employed to control the release of guest molecules. Zhao *et al.*[43] developed a drug delivery system based on boronic acid-functionalized mesoporous silica nanoparticles (BA-MSNs) for glucose-responsive controlled release of both insulin and cyclic adenosine monophosphate (cAMP). On the exterior surface of BA-MSN, fluorescein isothiocyanate-labeled, gluconic acid-modified insulin (FITC-G-Ins) proteins were immobilized and served as caps to encapsulate cAMP molecules inside the mesopores of BA-MSNs. This glucose-responsive double-release system could be applied to in vivo controlled-release biomedical applications as a new generation of self-regulated insulin-releasing devices.

Cauda *et al.*[44] synthesized an effective pH-dependent delivery system based on functionalized colloidal mesoporous silica (CMS) nanoparticles. At acidic pH, the ionic interactions between amino functionalities and sulfonate groups, leads to a gating system. The mesopores were effectively sealed under acidic condition (pH 2 and 4), thus preventing the release of the model drug ibuprofen from the inner volume of the modified CMS particles. At neutral pH, the unprotonated amino groups engage in weaker interactions with the SULF moieties, thus gradually opening the mesopores. A sustained release behavior was observed for the small pore gated sample. In contrast, fast release of the drug was shown from the unfunctionalized mesopores and the large-pore gated sample. These findings show that drug release rate can be finely controlled by changing the pH value of the release medium, as long as the size of the gating system is matched to the mesopore diameter.

1.3.5 Energy storage

Nanostructured materials have shown promising advantages as electrode materials for lithium ion batteries because of their high storage capacity and high rate performance; while the

disadvantage of nanocrystalline electrode materials is their low power density due to the low kinetics limited by the slow solid-state lithium-ion diffusion. In this regard, mesoporous electrode materials offer a clever solution to achieve high volumetric energy densities for lithium-ion batteries. Electrodes of mesoporous materials for lithium batteries have short transport lengths for Li^+ ions due to their nano-sized grains, and easy access for electrolytes due to their mesopores. Luo *et al.*[45] successfully prepared a well-ordered mesoporous spinel-structured $LiMn_2O_4$ that shows high rate capability and excellent cycling ability as a cathode for lithium-ion batteries.

In practice lithium ion battery applications, electronic conduction over micrometre-sized mesoporous particles limits the rate performance of mesporous materials. Occasionally, conductive thin layers of carbon or RuO_2 have been used to overcome such kinetic limitations and to achieve high storage performances. Saravanan *et al.*[46] found that mesoporous TiO_2 showed superior storage performance without such conductive surface layers. The storage performance and the packing density of the as-synthesized mesoporous TiO_2 is nearly 5 times and 6.6 times, respectively, higher than the commercially available TiO_2 nanoparticles. In addition, battery testing using mesoporous TiO_2 electrodes, without additive, exhibits nearly the same performance at low rate as the mesoporous TiO_2 with 15% carbon additives.

Independently, Shi *et al.*[47] prepared highly ordered mesoporous crystalline MoO_2 materials with mesoporous silica KIT-6 as a hard template. These mesoporous MoO_2 materials showed a typical metallic conductivity with a low resistivity, and primary test found that the mesoporous MoO_2 exhibit a reversible electrochemical lithium storage capacity as high as 750 mA h g^{-1} at C/20 after 30 cycles, rendering it as a promising anode material for lithium ion batteries.

The significant improvement of the electrochemical Li storage performance is attributed to the unique mesoporous structure of MoO_2, which has a variety of favorable properties. First, the hierarchical mesoporosity makes facile the liquid electrolyte diffusion into the bulk of the electrode material and hence provides fast conductive ion transport channels for the conductive ions. These mesostructured channels are also expected to buffer well against the local volume change during the Li uptake/removal reactions and thus to enhance the structural stability. Second, the MoO_2 wall with thickness of <10 nm greatly reduces the solid-state transport length for Li diffusion. Finally, the well-interconnected wall network matrix has a high electronic conductivity, which is different from other mesoporous metal oxide materials. This ensures the good electrical contact of the electrode during cycling.

Capacitive energy storage is distinguished from other types of electrochemical energy storage by short charging times and the ability to deliver significantly more power than batteries. A key limitation to this technology is its low energy density, and for this reason there is considerable interest in exploring pseudocapacitive materials where faradaic mechanisms offer increased levels of energy storage.

Wang *et al.*[48] prepared mesoporous carbon within the channels of anodic alumina membranes and used them as electrode materials for electrochemical capacitors. These mesoporous carbon nanofibers have proved to be promising electrode materials for electrochemical supercapacitors in high-rate charge/discharge operations. Compared to mesoporous carbon prepared from the same precursor sol, these one-dimensional nanofibers may provide a shortened diffusion distance for electrolyte ions. The better performance of these mesoporous nanofibers greatly benefited from their high specific surface area, shortened diffusion distance, mesoporous openings on the outer surface, and well-controlled pore size.

Brezesinski *et al.*[49] have shown that the capacitive charge-storage properties of mesoporous films of iso-oriented α-MoO_3 are superior to those of either mesoporous amorphous material or non-porous crystalline MoO_3. Whereas both crystalline and amorphous mesoporous materials show redox pseudocapacitance, the iso-oriented layered crystalline domains enable lithium ions to be inserted into the van der Waals gaps of the α-MoO_3. They propose that this extra contribution arises from an intercalation pseudocapacitance, which occurs on the same timescale as redox pseudocapacitance. The result is increased charge-storage capacity without compromising charge/discharge kinetics in mesoporous crystalline MoO_3. Brezesinski *et al.*[50] also synthesized and compared the electrochemical properties of highly ordered mesoporous T-Nb_2O_5, L-Ta_2O_5 and $TaNbO_5$ solid solution thin films with iso-oriented layered nanocrystalline domains. After thermal treatment, all the materials employed become highly crystalline and possessed an ordered cubic pore-solid architecture. Mesoporous T-Nb_2O_5 films were found to exhibit high levels of pseudocapacitive charge storage and much higher capacities than mesoporous amorphous films of the same initial Nb_2O_5 composition.

References

1. McCusker, L. B.; Liebau, F.; Engelhardt, G., Nomenclature of structural and compositional characteristics of ordered microporous and mesoporous materials with inorganic hosts. *Pure and Applied Chemistry* **2001,** *73* (2), 381-394.

2. Zhao, X. S.; Lu, G. M.; Graeme, J. M., Advance in Mesoporous Molelular Sieve MCM-41. *Ind Eng Chem Res* **1996,** *35* (7), 2075-2090.

3. (a) Hanns, B.; Gottfried, K. Process for producing silica in the form of hollow spheres. US3383172, 1968; (b) Page, M. L.; Beau, R.; Duchene, J. Porous silica particles containing a crystallized phase and method. US3493341, 1970; (c) Chiola, V.; Ritsko, J. E.; Vanderpool, C. D. Process for producting low-bulk density silica. US 3556725, 1971.

4. Yanagisawa, T.; Shuimizu, T.; Kuroda, K.; CKato, C., The Preparation of Alkyltrimethylammonium-Kanemite Complexes and Their Conversion to Microporous Materials. *Bull Chem Soc Jpn* **1990,** *63* (4), 988-992.

5. Lawrence, M. J., Surfactant systems: their use in drug delivery. *Chem Soc Rev* **1994,** *23* (6), 417-424.

6. Cheng, C.-F.; Luan, Z.; Klinowski, J., The Role of Surfactant Micelles in the Synthesis of the Mesoporous Molecular Sieve MCM-41. *Langmuir* **1995,** *11* (7), 2815-2819.

7. Beck, J. S.; Vartuli, J. C.; Roth, W. J.; Leonowicz, M. E.; Kresge, C. T.; Schmitt, K. D.; Chu, C. T. W.; Olson, D. H.; Sheppard, E. W., A new family of mesoporous molecular sieves prepared with liquid crystal templates. *J Am Chem Soc* **1992,** *114* (27), 10834-10843.

8. Monnier, A.; Schüth, F.; Huo, Q.; Kumar, D.; Margolese, D.; Maxwell, R. S.; Stucky, G. D.; Krishnamurty, M.; Petroff, P.; Firouzi, A.; Janicke, M.; Chmelka, B. F., Cooperative Formation of Inorganic-Organic Interfaces in the Synthesis of Silicate Mesostructures. *Science* **1993,** *261* (5126), 1299-1303.

9. Huo, Q.; Margolese, D. I.; Ciesla, U.; Feng, P.; Gier, T. E.; Sieger, P.; Leon, R.; Petroff, P. M.; Schuth, F.; Stucky, G. D., Generalized synthesis of periodic surfactant/inorganic composite materials. *Nature* **1994,** *368* (6469), 317-321.

10. Zhao, D.; Feng, J.; Huo, Q.; Melosh, N.; Fredrickson, G. H.; Chmelka, B. F.; Stucky, G. D., Triblock Copolymer Syntheses of Mesoporous Silica with Periodic 50 to 300 Angstrom Pores. *Science* **1998,** *279* (5350), 548-552.

11. (a) Yang, P. D.; Zhao, D. Y.; Margolese, D. I.; Chmelka, B. F.; Stucky, G. D., Generalized syntheses of large-pore mesoporous metal oxides with semicrystalline frameworks. *Nature* **1998,** *396* (6707), 152-155; (b) Yang, P. D.; Zhao, D. Y.; Margolese, D. I.; Chmelka, B. F.; Stucky, G. D., Block copolymer templating syntheses of mesoporous metal oxides with large ordering lengths and semicrystalline framework. *Chemistry of Materials* **1999,** *11* (10), 2813-2826.

12. Jun, S.; Joo, S. H.; Ryoo, R.; Kruk, M.; Jaroniec, M.; Liu, Z.; Ohsuna, T.; Terasaki, O., Synthesis of New, Nanoporous Carbon with Hexagonally Ordered Mesostructure. *J Am Chem Soc* **2000,** *122* (43), 10712-10713.

13. Yu, C.; Fan, J.; Tian, B.; Zhao, D.; Stucky, G. D., High-Yield Synthesis of Periodic Mesoporous Silica Rods and Their Replication to Mesoporous Carbon Rods. *Adv Mater* **2002,** *14* (23), 1742-1745.

14. Roggenbuck, J.; Tiemann, M., Ordered Mesoporous Magnesium Oxide with High Thermal Stability Synthesized by Exotemplating Using CMK-3 Carbon. *J Am Chem Soc* **2005,** *127* (4), 1096-1097.

15. (a) Jiao, F.; Jumas, J.-C.; Womes, M.; Chadwick, A. V.; Harrison, A.; Bruce, P. G., Synthesis of Ordered Mesoporous Fe3O4 and γ-Fe2O3 with Crystalline Walls Using Post-Template Reduction/Oxidation. *J Am Chem Soc* **2006,** *128* (39), 12905-12909; (b) Jiao, F.; Harrison, A.; Jumas, J.-C.; Chadwick, A. V.; Kockelmann, W.; Bruce, P. G., Ordered Mesoporous Fe2O3 with Crystalline Walls. *J Am Chem Soc* **2006,** *128* (16), 5468-5474.

16. Lai, X.; Li, X.; Geng, W.; Tu, J.; Li, J.; Qiu, S., Ordered Mesoporous Copper Oxide with Crystalline Walls. *Angewandte Chemie International Edition* **2007,** *46* (5), 738-741.

17. Lee, J.; Orilall, M. C.; Warren, S. C.; Kamperman, M.; Disalvo, F. J.; Wiesner, U., Direct access to thermally stable and highly crystalline mesoporous transition-metal oxides with uniform pores. *Nat Mater* **2008,** *7* (3), 222-228.

18. Warren, S. C.; Messina, L. C.; Slaughter, L. S.; Kamperman, M.; Zhou, Q.; Gruner, S. M.; DiSalvo, F. J.; Wiesner, U., Ordered mesoporous materials from metal nanoparticle-block copolymer self-assembly. *Science* **2008,** *320* (5884), 1748-1752.

19. (a) Itoh, N.; Kato, K.; Tsuji, T.; Hongo, M., Preparation of a tubular anodic aluminum oxide membrane. *Journal of Membrane Science* **1996,** *117* (1-2), 189-196; (b) Lira, H. d. L.; Paterson, R., New and modified anodic alumina membranes - Part III. Preparation and characterisation by gas diffusion of 5 nm pore size anodic alumina membranes. *Journal of Membrane Science* **2002,** *206* (1), 375-387.

20. (a) Deng, W.; Shanks, B. H., Synthesis of Hierarchically Structured Aluminas under Controlled Hydrodynamic Conditions. *Chemistry of Materials* **2005,** *17* (12), 3092-3100; (b) Deng, W.; Toepke, M. W.; Shanks, B. H., Surfactant-Assisted Synthesis of Alumina with Hierarchical Nanopores. *Advanced Functional Materials* **2003,** *13* (1), 61-65.

21. Yuan, C.; Xiong, S.; Zhang, X.; Shen, L.; Zhang, F.; Gao, B.; Su, L., Template-free synthesis of ordered mesoporous NiO/poly(sodium-4-styrene sulfonate) functionalized carbon nanotubes composite for electrochemical capacitors. *Nano Research* **2009,** *2* (9), 722-732.

22. Xue, Z.; Ma, J.; Hao, W.; Bai, X.; Kang, Y.; Liu, J.; Li, R., Synthesis and characterization of ordered mesoporous zeolite LTA with high ion exchange ability. *Journal of Materials Chemistry* **2012**.

23. Takahara, Y.; Kondo, J. N.; Takata, T.; Lu, D.; Domen, K., Mesoporous Tantalum Oxide. 1. Characterization and Photocatalytic Activity for the Overall Water Decomposition. *Chemistry of Materials* **2001,** *13* (4), 1194-1199.

24. Noda, Y.; Lee, B.; Domen, K.; Kondo, J. N., Synthesis of Crystallized Mesoporous Tantalum Oxide and Its Photocatalytic Activity for Overall Water Splitting under Ultraviolet Light Irradiation. *Chemistry of Materials* **2008,** *20* (16), 5361-5367.

25. Yang, Y.-H.; Wang, Y.; Ko, A.-N., Mesoporous vanadium oxide as catalyst for liquid-phase selective oxidation of diphenylmethane to benzophenone. *Journal of Porous Materials* **2011,** *18* (6), 735-742.

26. Tagusagawa, C.; Takagaki, A.; Iguchi, A.; Takanabe, K.; Kondo, J. N.; Ebitani, K.; Tatsumi, T.; Domen, K., Synthesis and Characterization of Mesoporous Ta−W Oxides as Strong Solid Acid Catalysts. *Chemistry of Materials* **2010,** *22* (10), 3072-3078.

27. Chaliha, S.; Bhattacharyya, K. G., Using Mn(II)−MCM41 as an Environment-Friendly Catalyst to Oxidize Phenol, 2-Chlorophenol, and 2-Nitrophenol in Aqueous Solution. *Industrial & Engineering Chemistry Research* **2008,** *47* (5), 1370-1379.

28. Samuel, P. P.; Shylesh, S.; Singh, A. P., Catalytic properties of tin-containing mesoporous molecular sieves in the selective reduction of carbonyl compounds (Meerwein–Ponndorf–Verley (MPV) reaction). *Journal of Molecular Catalysis A: Chemical* **2007,** *266* (1–2), 11-20.

29. Lee, C.-H.; Lin, T.-S.; Mou, C.-Y., (VO)2+ Ions Immobilized on Functionalized Surface of Mesoporous Silica and Their Activity toward the Hydroxylation of Benzene. *The Journal of Physical Chemistry B* **2003,** *107* (11), 2543-2551.

30. Brutchey, R. L.; Ruddy, D. A.; Andersen, L. K.; Tilley, T. D., Influence of Surface Modification of Ti−SBA15 Catalysts on the Epoxidation Mechanism for Cyclohexene with Aqueous Hydrogen Peroxide. *Langmuir* **2005,** *21* (21), 9576-9583.

31. Corma, A.; Martínez, A.; Martínez-Soria, V., Hydrogenation of Aromatics in Diesel Fuels on Pt/MCM-41 Catalysts. *Journal of Catalysis* **1997,** *169* (2), 480-489.

32. Su, F.; Zeng, J.; Bao, X.; Yu, Y.; Lee, J. Y.; Zhao, X. S., Preparation and Characterization of Highly Ordered Graphitic Mesoporous Carbon as a Pt Catalyst Support for Direct Methanol Fuel Cells. *Chemistry of Materials* **2005,** *17* (15), 3960-3967.

33. Qi, J.; Jiang, L.; Wang, S.; Sun, G., Synthesis of graphitic mesoporous carbons with high surface areas and their applications in direct methanol fuel cells. *Applied Catalysis B-Environmental* **2011,** *107* (1-2), 95-103.

34. Moura, C. P.; Vidal, C. B.; Barros, A. L.; Costa, L. S.; Vasconcellos, L. C. G.; Dias, F. S.; Nascimento, R. F., Adsorption of BTX (benzene, toluene, o-xylene, and p-xylene) from aqueous solutions by modified periodic mesoporous organosilica. *Journal of colloid and interface science* **2011,** *363* (2), 626-34.

35. M. Kisler, J.; Dähler, A.; W. Stevens, G.; J. O'Connor, A., Separation of biological molecules using mesoporous molecular sieves. *Microporous and Mesoporous Materials* **2001,** *44–45* (0), 769-774.

36. Eliseev, A. A.; Kolesnik, I. V.; Lukashin, A. V.; Vasiliev, R. B.; Tretyakov, Y. D., Nanoparticle separation by mesoporous molecular sieves. *Mendeleev Communications* **2004,** *14* (4), 173-174.

37. Mekawy, M. M.; Yamaguchi, A.; El-Safty, S. A.; Itoh, T.; Teramae, N., Mesoporous silica hybrid membranes for precise size-exclusive separation of silver nanoparticles. *Journal of Colloid and Interface Science* **2011,** *355* (2), 348-358.

38. Konjhodzic, D.; Bretinger, H.; Marlow, F., Structure and properties of low-n mesoporous silica films for optical applications. *Thin Solid Films* **2006,** *495* (1–2), 333-337.

39. Fiorilli, S.; Onida, B.; Macquarrie, D.; Garrone, E., Mesoporous SBA-15 silica impregnated with Reichardt's dye: a material optically responding to NH3. *Sensors and Actuators B: Chemical* **2004,** *100* (1–2), 103-106.

40. Balaji, T.; Sasidharan, M.; Matsunaga, H., Optical sensor for the visual detection of mercury using mesoporous silica anchoring porphyrin moiety. *Analyst* **2005,** *130* (8), 1162-1167.

41. Vallet-Regi, M.; Rámila, A.; del Real, R. P.; Pérez-Pariente, J., A New Property of MCM-41: Drug Delivery System. *Chemistry of Materials* **2000,** *13* (2), 308-311.

42. Lu, J.; Liong, M.; Zink, J. I.; Tamanoi, F., Mesoporous Silica Nanoparticles as a Delivery System for Hydrophobic Anticancer Drugs. *Small* **2007,** *3* (8), 1341-1346.

43. Zhao, Y.; Trewyn, B. G.; Slowing, I. I.; Lin, V. S. Y., Mesoporous Silica Nanoparticle-Based Double Drug Delivery System for Glucose-Responsive Controlled Release of Insulin and Cyclic AMP. *J Am Chem Soc* **2009,** *131* (24), 8398-8400.

44. Cauda, V.; Argyo, C.; Schlossbauer, A.; Bein, T., Controlling the delivery kinetics from colloidal mesoporous silica nanoparticles with pH-sensitive gates. *Journal of Materials Chemistry* **2010,** *20* (21), 4305-4311.

45. Luo, J.-y.; Wang, Y.-g.; Xiong, H.-m.; Xia, Y.-y., Ordered Mesoporous Spinel LiMn2O4 by a Soft-Chemical Process as a Cathode Material for Lithium-Ion Batteries. *Chemistry of Materials* **2007,** *19* (19), 4791-4795.

46. Saravanan, K.; Ananthanarayanan, K.; Balaya, P., Mesoporous TiO2 with high packing density for superior lithium storage. *Energy & Environmental Science* **2010,** *3* (7), 939-948.

47. Shi, Y.; Guo, B.; Corr, S. A.; Shi, Q.; Hu, Y.-S.; Heier, K. R.; Chen, L.; Seshadri, R.; Stucky, G. D., Ordered Mesoporous Metallic MoO2 Materials with Highly Reversible Lithium Storage Capacity. *Nano Letters* **2009,** *9* (12), 4215-4220.

48. Wang, K.; Wang, Y.; Wang, Y.; Hosono, E.; Zhou, H., Mesoporous Carbon Nanofibers for Supercapacitor Application. *The Journal of Physical Chemistry C* **2008,** *113* (3), 1093-1097.

49. Brezesinski, T.; Wang, J.; Tolbert, S. H.; Dunn, B., Ordered mesoporous [alpha]-MoO3 with iso-oriented nanocrystalline walls for thin-film pseudocapacitors. *Nat Mater* **2010,** *9* (2), 146-151.

50. Brezesinski, K.; Wang, J.; Haetge, J.; Reitz, C.; Steinmueller, S. O.; Tolbert, S. H.; Smarsly, B. M.; Dunn, B.; Brezesinski, T., Pseudocapacitive Contributions to Charge Storage in Highly Ordered Mesoporous Group V Transition Metal Oxides with Iso-Oriented Layered Nanocrystalline Domains. *J Am Chem Soc* **2010,** *132* (20), 6982-6990.

Chapter Two: Size Controlled Synthesis of Mesoporous Silica Nanospheres

2.1 Introduction

Before the synthesis of the mesoporous silica, Stöber *et al.*[1] had conducted in 1968 comprehensively research on the chemistry that occurs during the growth of mono-dispersed silica spherical particles. The researchers obtained spherical silica particles upon hydrolysis of alkyl silicates followed by condensation of silicic acid in alcoholic solution. The chemical reactions involved in the so-called "Stöber method" can be summarized as the following:

(a) Hydrolysis: $Si(OR)_4 + nH_2O \rightarrow Si(OR)_{4-n}(OH)_n + nROH$

(b) Alcohol Condensation: $Si\text{-}OR + HO\text{-}Si \rightarrow Si\text{-}O\text{-}Si + ROH$

(c) Water Condensation: $Si\text{-}OH + HO\text{-}Si \rightarrow Si\text{-}O\text{-}Si + H_2O$

In their research, the diameters of resulting silica particles can been controlled from less than 50 nm up to 2000 nm, depending type of silicate ester, type of alcohol, and volume ratio of alcohol to water that is used. Subsequent to the initial synthesis of mesoporous silica, a modified Stöber method was introduced to prepare monodispersed spherical mesoporous silica particles of controlled size. Grün *et al.*[2] in 1997 were the first group to report the synthesis of micrometer and submicrometer sized spheres of ordered mesoporous silica MCM-41 with a modified Stöber method. A few years later, Yano *et al.*[3] successfully synthesized monodispersed mesoporous silica spheres with particle sizes range from 0.52 to 1.25 μm using tetramethoxysilane and n-decyltrimethylammonium bromide. It is found that the size of spherical mesoporous silica particles can be controlled by variation of the synthesis temperature, methanol/water ratio of the solvent, and silica the source. Since these submicron mesoporous silica spheres had particle diameters equivalent to the wavelength of visible light, they were promising for the applications

such as photonic crystals. Moreover, mesoporous silica nanospheres (MSNs) of particle sizes from 50 to 300 nm are known to be able to allow facile endocytosis by living animal and plant cells without causing any significant cytotoxicity.[4] Consequently, MSNs of proper sizes can be designed to be used as vehicles for the delivery of drugs, since mesoporous structures have promising loading and release properties.

In the author's research, pH has been used as a control parameters to acquire different sizes of MSNs. These MSNs with mono-distributed particle sizes ranging from c.a. 30 to 150 nm were successfully synthesized at pH values between round 11.86 and 12.59. However, when the initial pH values was higher than 12.59, the product was found to be a mixture of two different sizes of mesoporous silica particles. Close investigation indicates, that besides the particle sizes, surface area and pore sizes of the MSNs are also depend on the reaction pH values. Expanded research efforts have also shown that gold nanoparticles can be selectively grown inside the mesopores or attached on the external surface of the MSNs.

2.2 Experiments

2.2.1 Materials

Sodium hydroxide (NaOH) with a purity of 98.7% was obtained from J. T. Baker. Cetyltrimethylammonium bromide (CTAB) with a purity of 99+% was purchased from Alfa-Aesar. Tetraethoxysilane (TEOS) with 98% purity was purchased from Acros. HPLC grade ethanol was supplied by Sigma-Aldrich. All chemicals were used as received without further purification. Triply distilled water was utilized for the solution preparation and washing procedure.

2.2.2 Synthesis of MSNs

The synthesis of MSNs was based on the surfactant mediated, soft template approach, and the modified Stöber method was used to control the morphology and the particle sizes. In the synthesis, the only parameter applied to control the particle size was the pH value. The experimental conditions in various reactions are listed in Table 2.1.

Table 2.1 The experimental conditions in the synthesis of MSNs.

Sample name	H_2O	NaOH (1M)	Before reaction	CTAB	TEOS	EtOH	After reaction
	ml	ml	pH	G	ml	ml	pH
YZ0921	960	4.0	11.86@24.1	2.000	13.0	14.0	7.38@25.1
YZ0922	960	8.0	12.15@24.1	2.000	13.0	14.0	10.27@20.7
YZ0923	960	12.0	12.33@24.0	2.000	13.0	14.0	10.72@18.4
YZ0924	960	16.0	12.46@24.0	2.000	13.0	14.0	10.83@21.2
YZ0925	960	20.0	12.55@24.0	2.000	13.0	14.0	10.84@25.8
YZ0928	960	24.0	12.59@24.3	2.001	13.0	14.0	11.14@26.4
YZ0927	960	28.0	12.64@24.1	2.000	13.0	14.0	11.12@28.3
YZ0910	960	30.0	12.79@19.9	2.002	13.0	14.0	11.39@21.7

*pH values are noted in the format of pH value @ temperature by Celsius degree

A typical experimental procedure might be described as followed: A 1.0 M solution of NaOH was prepared in advance by dissolving 40.0 g NaOH in 1000 mL distilled water. In the experiment, 4.0 to 30.0 mL of 1.0 M NaOH (various amount in different experiments) and 960 mL distilled water were first added to a 2 L-Erlenmeyer flask, and then stirring with a magnetic

stirring bar at about 600 rpm. 2.0 g CTAB was then added to the flask, follow by heating the solution to 80.0 ºC. After the temperature of the solution was stabilized, 13.0 mL TEOS and 14.0 mL ethanol were added to the solution. The mixed solution was stirred at 80.0 ºC for 2 hours to complete the reaction. Large amount of white precipitate was observed during the reaction procedure. After the reaction, the suspension was cooled in air, then filtered, and the solid precipitate was washed with methanol 3 times and dried in the air. This as-prepared white powder was collected, then calcined at ~540 °C for 12 hours to remove organic template CTAB. The calcined samples were stored in 20mL vial sealed with parafilm for future investigation.

2.3 Characterization

2.3.1 Low-angle powder X-ray diffraction (XRD)

The samples before calcination and after calcination were characterized by low-angle powder X-ray diffraction (XRD). The low-angle XRD measurements were performed using a PANalytic X-ray diffractometer with voltage of 45 kV and current of 40 mA; 2θ angles ranged from 1 to 7 º with step size at 0.005 º. The X-ray source was monochromatic Cu Kα (λ=1.54 Å) radiation with a nickel filter.

2.3.2 Dynamic light scattering (DLS)

Dynamic lights scattering data were recorded using a Brookhaven Instrument Co. BIC 90Plus particle size analyzer at 90° detection angle. For this instrument, the analytical range of the particle size is < 1 nm to 6 μm. Samples for DSL measurement were prepared as follows: a small amount of powdered sample was first dispersed in double distilled water, and then the suspension was sonicated for at least 5 minutes in order to get well-dispersed suspension. After

letting the suspension settle for 5 minutes, several drops of upper suspension was transferred to sample curvet for the DSL measurement.

2.3.3 Transition electron microscopy (TEM)

Transition electron microscopy (TEM) investigations were performed using a Zeiss EM 902 thermionic (tungsten) transmission electron microscope at an accelerating voltage of 80 kV. The samples used for TEM observations were prepared by dispersing them in ethanol followed by ultrasonic vibration for 5 min, and then placing a drop of the suspension onto a copper grid coated with a layer of amorphous carbon. Finally the solvent was evaporated in air.

2.3.4 Nitrogen adsorption-desorption measurement

Nitrogen adsorption-desorption measurements were carried out on a Micrometrics ASAP 2020 volumetric adsorption analyzer at -196 $^{\circ}$C. Before the adsorption analysis, calcined samples were outgassed under a vacuum at 200 $^{\circ}$C in the port of the adsorption analyzer.

2.4 Results and discussion

Ordered mesoporous silica nanospheres have been synthesized via the surfactant-mediate soft template approach with CTAB as the surfactant. Spherical morphology of the particles was controlled by the amount of ethanol via the Stöber method. The pH values have been controlled in the different experiments, which leads to various MSNs particle sizes and surface conditions. Some important parameters have been investigated to characterize the properties of the as-prepared and calcined MSNs.

2.4.1 Calcination temperatures

There are two typically methods commonly used to remove the surfactants from mesoporous silica, including calcination and acid-extraction.[5] The acid-extraction method helps to preserve surface functional groups. While, calcination at low temperature (100 to 400 ºC) also removes the template and maintains the surface functional groups, the higher temperature calcination destroys the functional groups and improve the crystallinity of the framework, which would help strengthen the mesoporous structure. In this research, calcination was selected in order to get more stabilized mesoporous silica frameworks.

To investigate the effect of calcination, we extend the calcination period to ~12 hours in order to completely remove the surfactant templates. Low-angle XRD was used to investigate the changes in mesostructures before and after calcinations; changes in d-spacing were compared for different samples (shown in figure 2.1). It was observed that for all samples, longer calcination resulted to smaller d-spacing and lower peak intensities, where smaller d-spacing after calcination is due to shrinkage of the silica framework during processing and the shrinkage of the framework requires physically removal of the template from mesopores and/or channels. At the same time, the lower peak intensities are due to the reduced order in the mesoporous framework after the removal of the template.

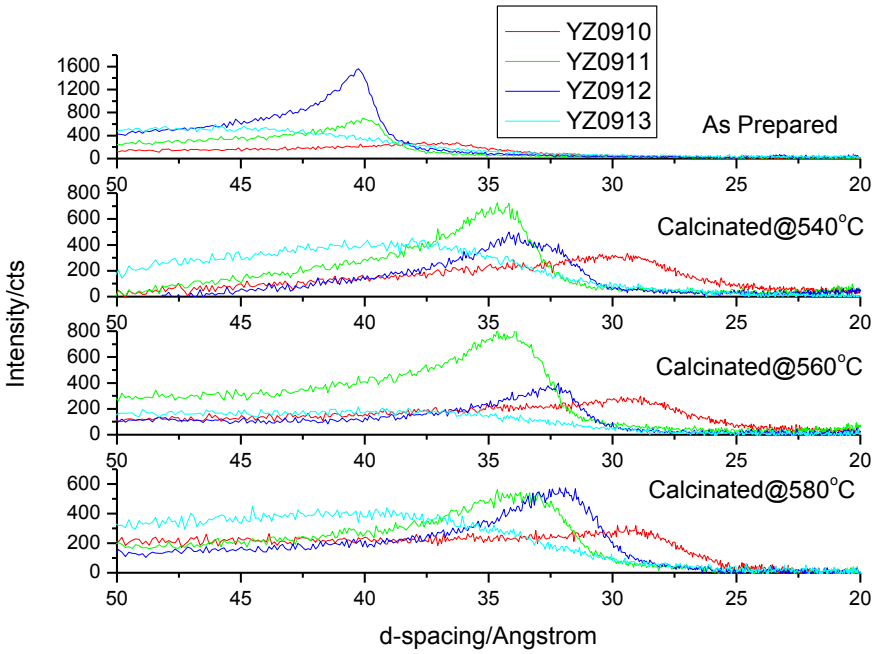

Figure 2.1 d-spacing of MSNs calcinated at different temperatures (sample YZ0910, YZ0911, YZ0912, and YZ0913 are prepared from initial pH 12.76, 12.55, 12.66, and 12.34, respectively).

Comparing different calcination temperatures, only slight shrinkage in the d-spacing are found in the framework. This indicates the structure parameters are decided by the silica frameworks themselves, due to the effective removal of the template for all temperatures. The residual slight differences are due to the better packing of the silica framework. It was also found that after calcination at 580 ºC, the peak intensities are lower than those of 540 ºC and 560 ºC; this indicates destruction occurred in the silica framework. So calcination at 580 ºC or higher temperature should be avoided. Base on this result, the calcination temperature 540 ºC, at which the template can be totally removed and the framework is still stable, was used in the extended work.

2.4.2 Morphology and structure of MSNs

TEM was used to characterize the morphology and structure of products. It is to be noted that the 80 kV electron beam is powerful enough to pass through small MSN particles, so that mesoporous structures can be directly investigated using the TEM in our case. Figure 2.2 to figure 2.10 shows TEM graphs of the calcined MSNs prepared from various experiments. Rough estimations of the particle sizes have been provided in order to clarify the trend of particle size with the change of pH values.

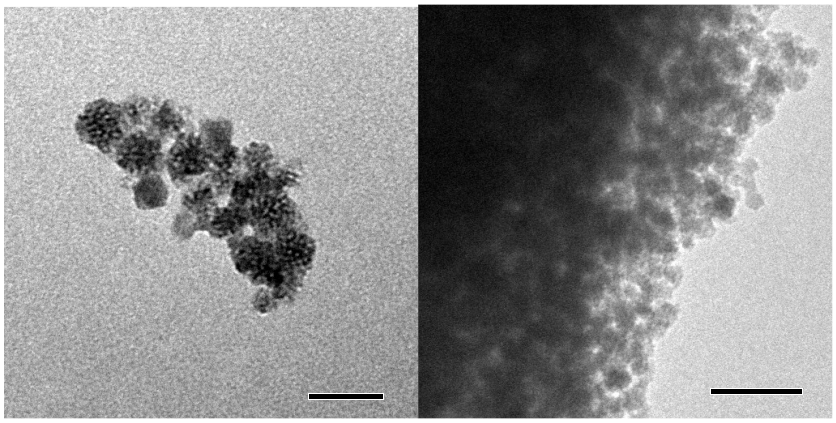

Figure 2.2 TEM graphs of sample YZ0921a (average particles size ~25 nm).

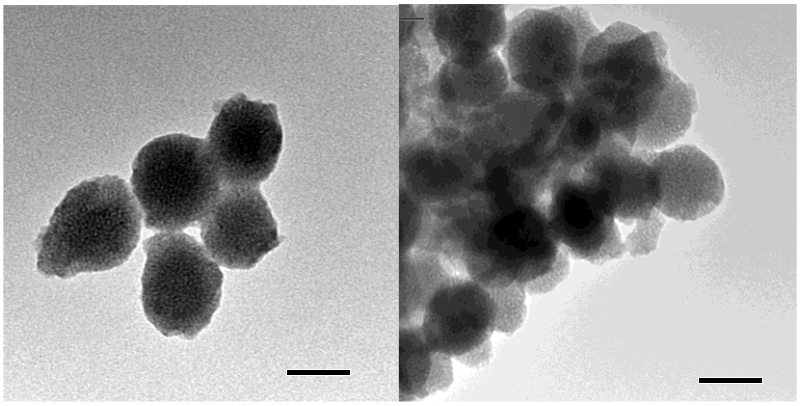

Figure 2.3 TEM graphs of sample YZ0922a (average particles size ~60 nm).

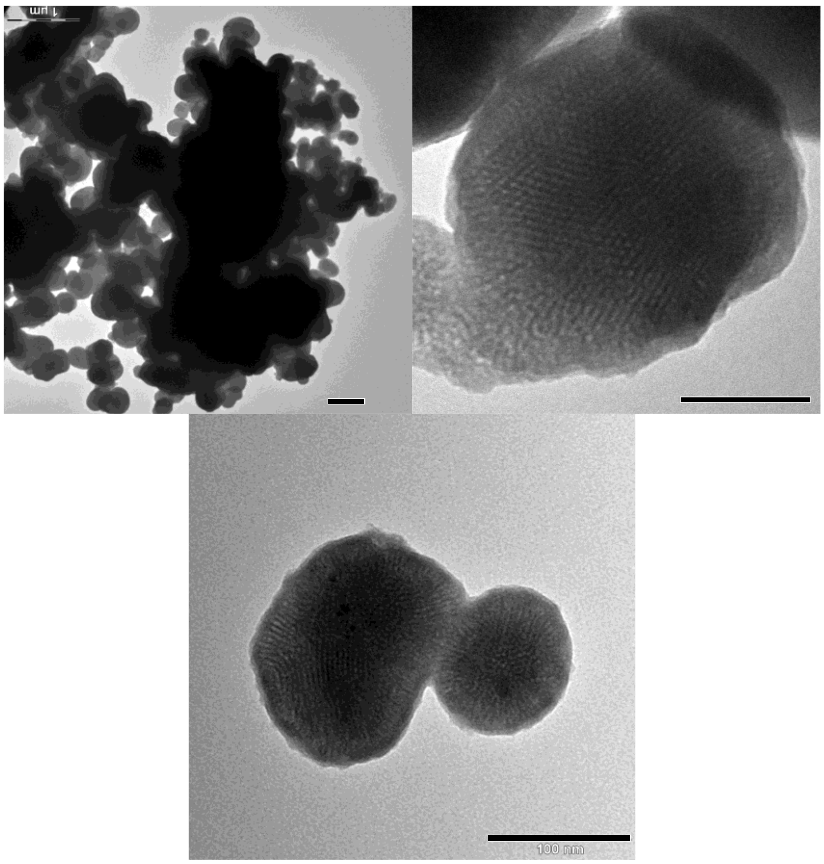

Figure 2.4 TEM graphs of sample YZ0923a (average particles size ~150 nm).

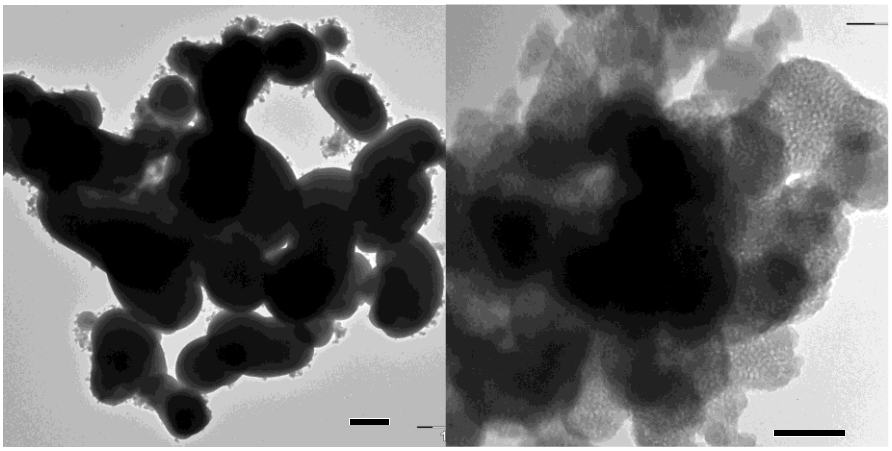

Figure 2.5 TEM graphs of sample YZ0924a (two different particles size ~80 nm and ~700nm can be investigated).

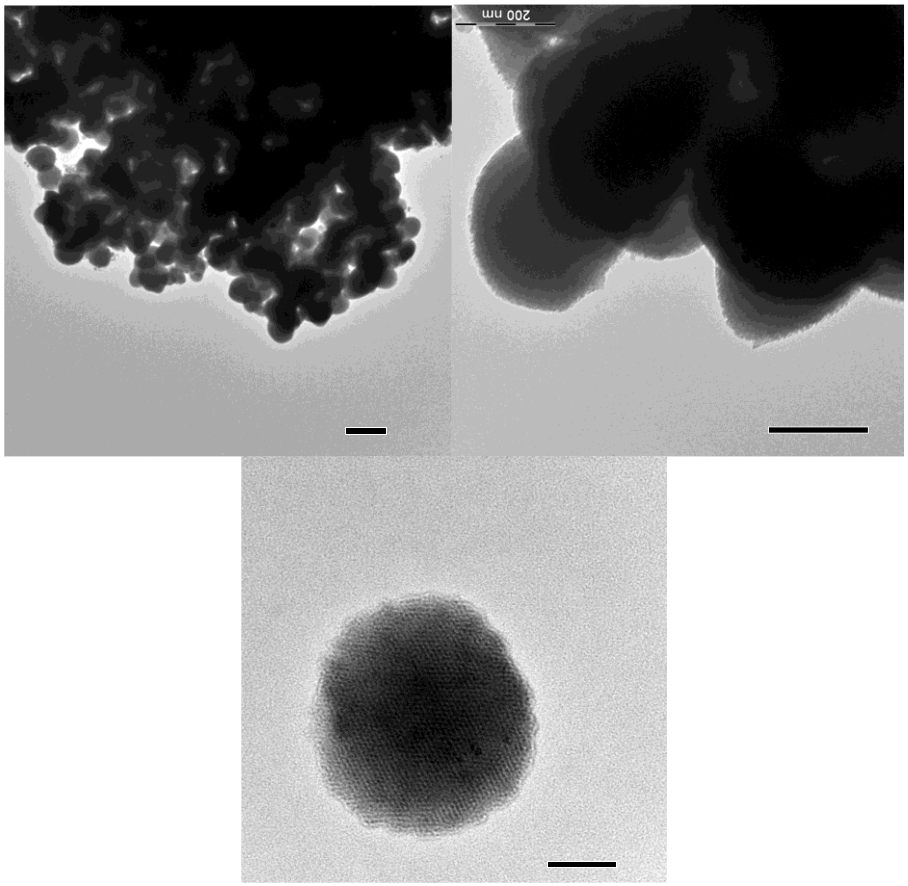

Figure 2.6 TEM graphs of sample YZ0925a (average particles size ~200 nm).

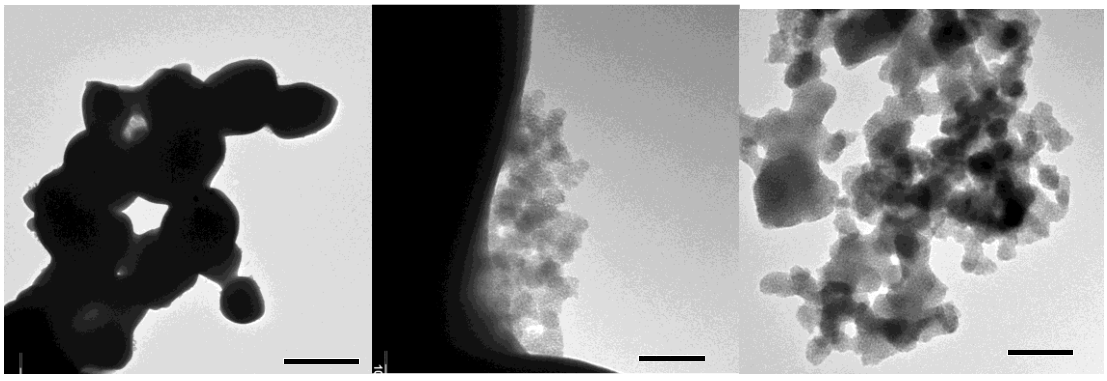

Figure 2.7 TEM graphs of sample YZ0928a (two different particles size ~20 nm and ~2μm can be investigated).

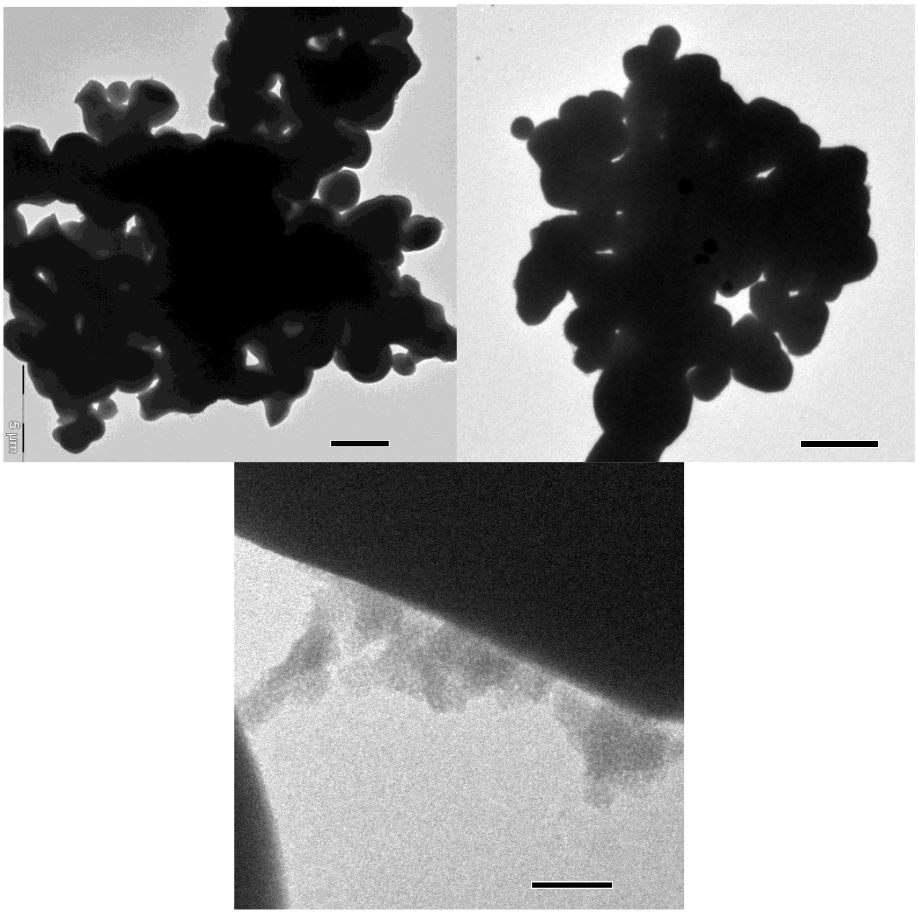

Figure 2.8 TEM graph of sample YZ0927a (two different particles size ~20 nm and ~2µm can be investigated).

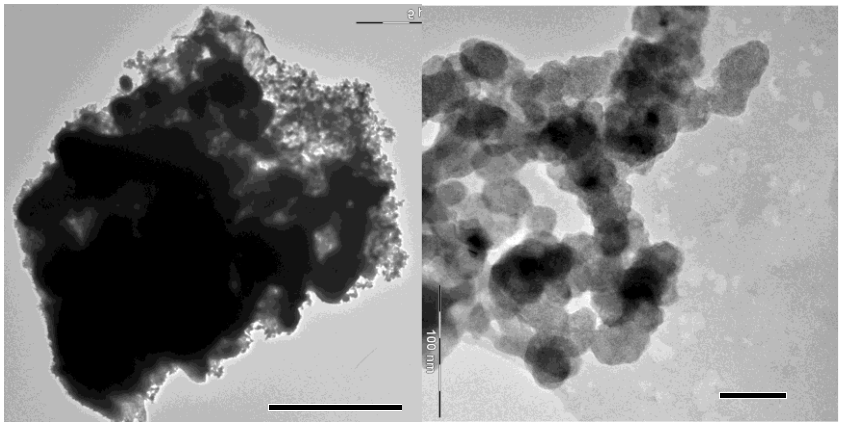

Figure 2.9 TEM graph of sample YZ0910a (two different particles size ~20 nm and ~4µm can be investigated).

Base on TEM micrographs, it is determined that spherical mesoporous silica particles have been formed. The size distributions estimated from different synthetic conditions are as follows: sample YZ0921a was synthesized at pH 11.86, which has a particle size of around 25 nm (figure 2.2); sample YZ0922a was prepared at pH 12.15, has particle size around 60 nm (figure 2.3); sample YZ0923a was prepared at pH 12.33, has particle size around 150 nm (figure 2.4); sample YZ0924a was prepared at pH 12.46, has two particle sizes 80 nm and 700 nm (figure 2.5); sample YZ0925a was prepared at pH 12.55, has particle sizes around 200 nm (figure 2.6); sample YZ0928a was prepared at pH 12.59, has two particle sizes 20 nm and 2 μm (figure 2.7); sample YZ0927a was prepared at pH 12.64, has two particle sizes 20 nm and 2 μm (figure 2.8); and sample YZ0910a was prepared at pH 12.79, has two particle sizes 20 nm and 4 μm (figure 2.9). At large pH values, the as-prepared MSN particles are no longer possess a single-size distribution. A change of the synthesis mechanism likely has occurred.

2.4.3 Phase analysis of MSNs

Due to instrumental restriction and the poor ordering of samples, no phase information can be derived in the XRD results. However, the size of the MSN mesopores are in the range of ca. 4 nm and the sample particle sizes are generally sub-micron range. Base on the TEM graph, it is sufficient to exploit the good resolution to visualize the ordered mesoporous lattice.

In order to get phase information of the ordered mesostructure silica, more analysis was done with the TEM measurements. Figure 2.10 shows the TEM image of one MSN particle and the calculated diffraction pattern converted by Gatan Digital Micrograph software. The diffraction spot can be indexed by the 2D hexagonal lattice. This indicates that the MSN

particles synthesized in our experiments are 2D hexagonal, well-ordered mesoporous silica nanosphere.

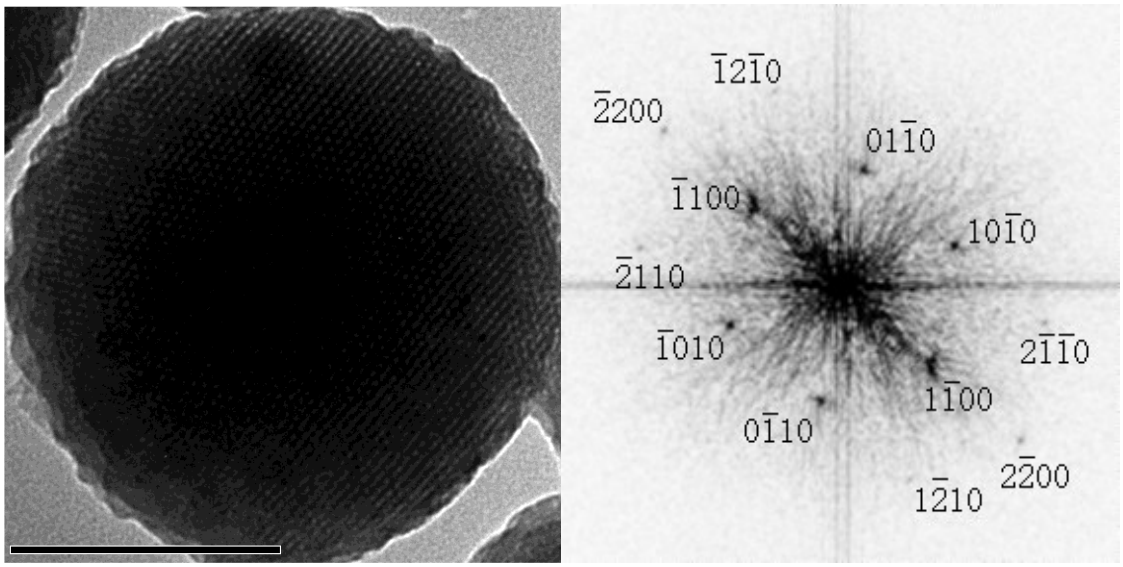

Figure 2.10 TEM of a MSN particle of sample YZ0923 (left) and calculated diffraction pattern; hexagonal phase with z=[0001] (right).

2.4.4 Lattice parameters at different synthesis pHs

Figure 2.11a and 2.11c show the low-angle XRD patterns of the MSN samples before and after calcination. Figure 2.11b and 2.11d are the d-spacing converted from the XRD patterns. It is clear that products prepared from higher pH values give smaller d-spacing in the hexagonal lattice. Base our phase analysis, we know the peaks are the diffraction by d_{100} of the mesostructured lattice; hence we can make a plot based on the d_{100} spacing verses pH value. The result is shown in figure 2.12.

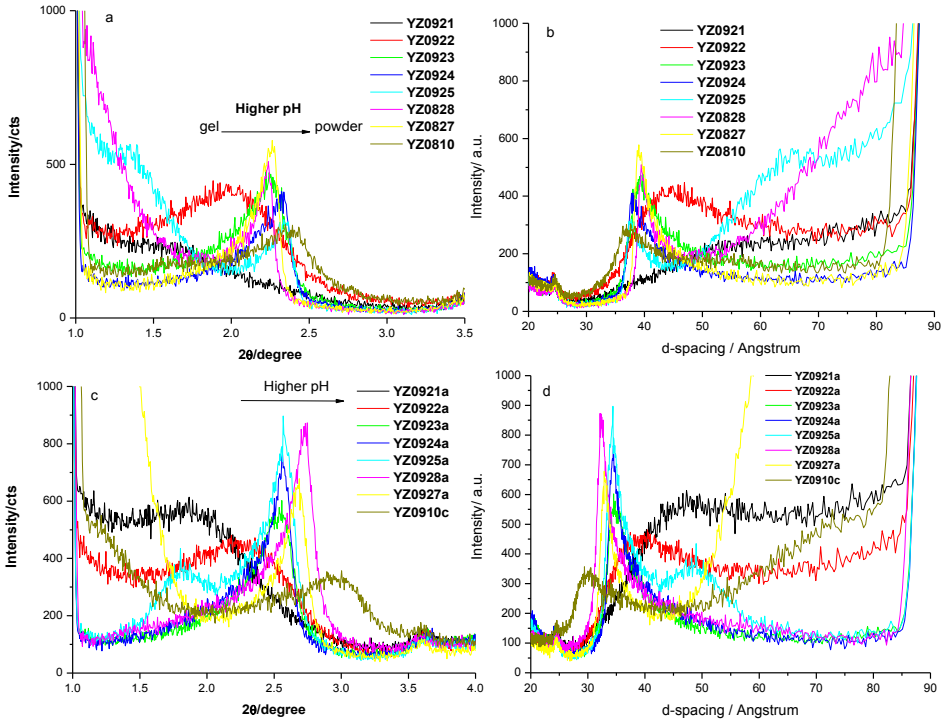

Figure 2.11 The XRD patterns of the MSN samples before calcination (a, b) and after calcination (c, d) at different pHs.

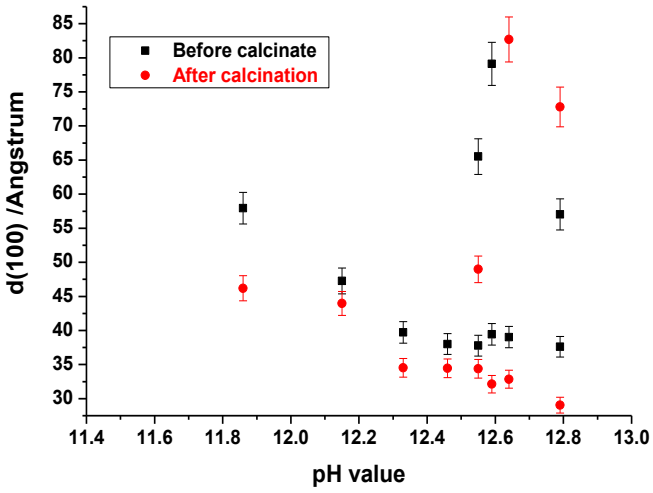

Figure 2.12 d-spacing of MSNs before and after calcinations.

As we have investigate in TEM graphs, there are two different particle size in the high pH conditions; corresponding XRDs shows two d(100) features at high pHs. We deduce that the particle size can be directly correlated to the d_{100} spacing in the synthesis. The small particles are formed with less order and larger d-spacing; on the other hand, the larger particles are more ordered with smaller d-spacing.

2.4.5 Particle size analysis

Size distributions of the MSN samples were also obtain from DLS measurement, as shown in figure 2.13 to figure 2.19. The sizes of the particles showed the same trend as indicated by XRD and TEM. When the pH is greater than 12.60, there are two different sizes of MSN particles co-existing in the sample. When the pH values are smaller than ca. 12.33, the sizes of the MSN are dependent on the pH values, where the smaller pH provides smaller particles.

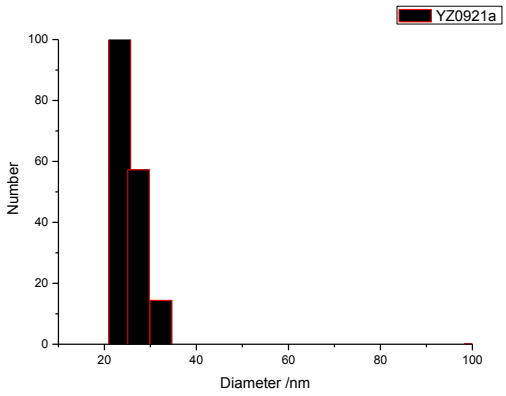

Figure 2.13 DLS data for sample YZ0921a size distribution by numbers.

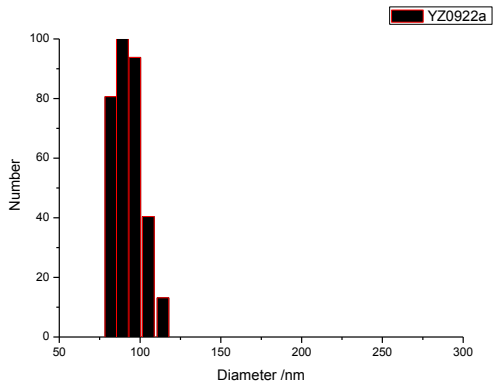

Figure 2.14 DLS data for sample YZ0922a size distribution by numbers.

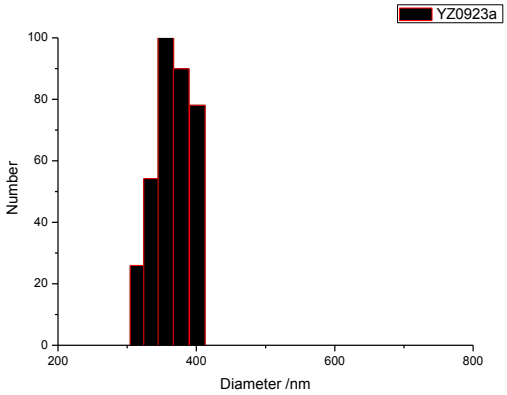

Figure 2.15 DLS data for sample YZ0923a size distribution by numbers.

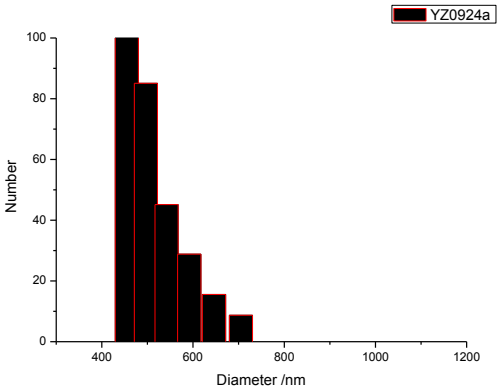

Figure 2.16 DLS data for sample YZ0924a size distribution by numbers.

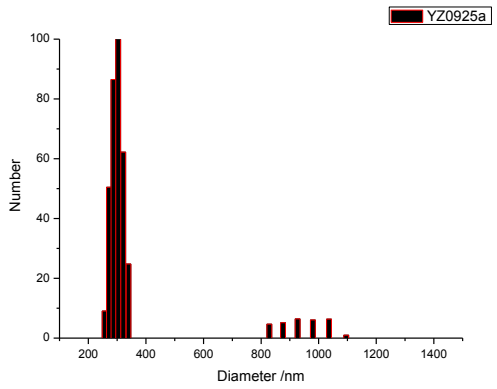

Figure 2.17 DLS data for sample YZ0925a size distribution by numbers.

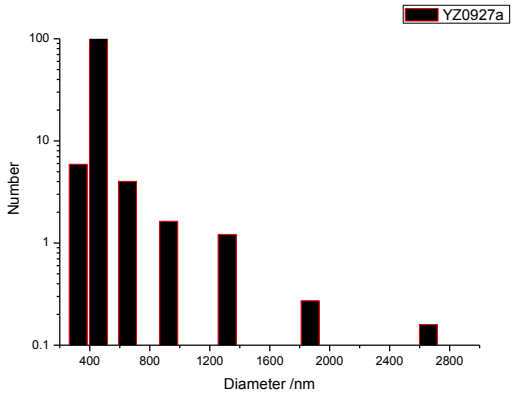

Figure 2.18 DLS data for sample YZ0927a size distribution by numbers.

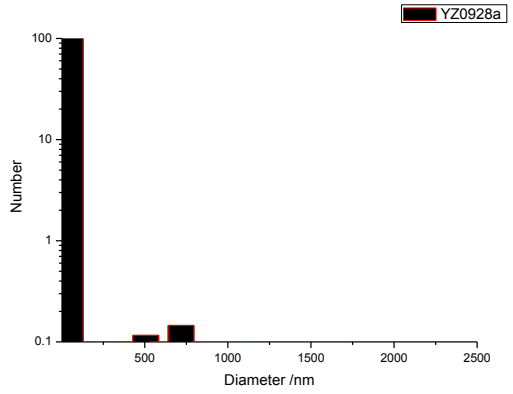

Figure 2.19 DLS data for sample YZ0928a size distribution by numbers.

Table 2.2 Average particle size determined using DLS

Sample	YZ0921a	YZ0922a	YZ0923a	YZ0924a	YZ0925a
pH	11.86	12.15	12.33	12.46	12.55
Size (nm)	25.4±1.3	92.5±4.6	366±18	507±25	299±15

2.4.6 Surface area and pore size distribution

Nitrogen adsorption-desorption was measured in order to exam the surface conditions of the mesoporous particles. The isotherm plots are shown in figure 2.20 and the corresponding structure parameters calculated by the BJH method[6] are listed in Table 2.3.

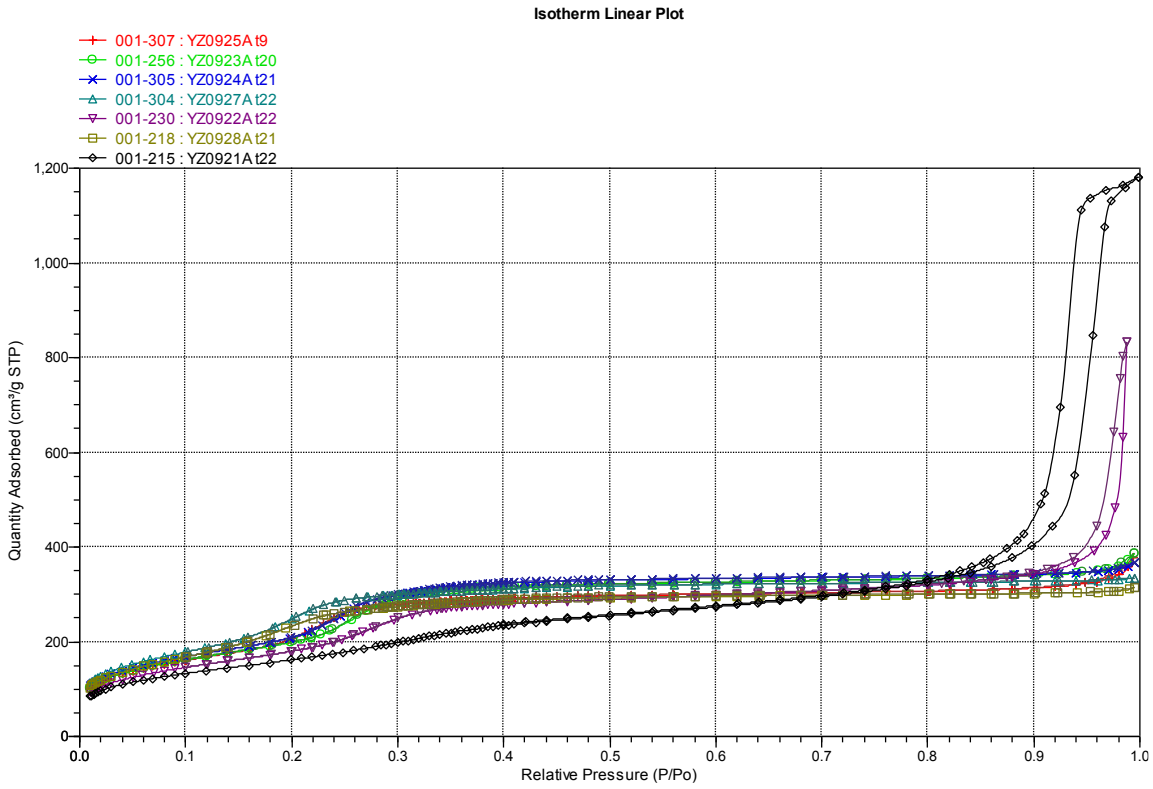

Figure 2.20 N_2 adsorption/desorption isotherm linear plot of the calcinated samples.

Table 2.3 Mesoporous structure parameters from nitrogen adsorption method.

Sample	S_{BJH} (m^2/g)	V_d (ml/g)	W_d (nm)	S_d (m^2/g)	*α-S slope* (m^3/g STP)
YZ0921a	590.1	1.930	11.827	650.0	236.8± 4.5
YZ0922a	656.0	1.399	7.533	742.8	289.1± 11.5
YZ0923a	726.6	0.724	3.457	837.8	329.9± 18.1
YZ0924a	759.5	0.691	2.932	858.0	364.0± 22.1
YZ0925a	739.0	0.553	3.477	794.3	346.2± 21.7
YZ0928a	852.8	0.604	2.886	837.6	387.3± 13.2
YZ0927a	908.2	0.643	2.879	893.2	416.7± 18.4

* ***S_{BJH} = surface area calculated using the BJH method; V_d = primary mesopore volume; W_d = primary pore size calculated from BJH model ; S_d = Surface area of primary mesopores calculated from V_d and W_d;***

To get better pore size results of the MCM-41, Kruk *et al.*[7] introduced correction to the BJH method, known as the KJS correction. Base on the BJH-KJS correction, we can get the corrected pore size distributions. As plotted in figure 2.21, the corrected pore size distribution is more consistent with the XRD and TEM results.

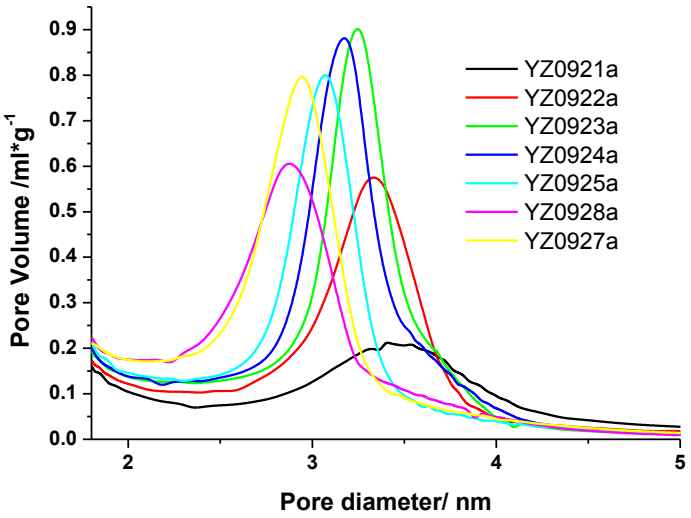

Figure 2.21. BJH-KJS pore size distribution for calcinated samples.

2.4.7 D-spacing, pore sizes and wall thicknesses for different pHs

Base on the pore size and the lattice spacing result, we can calculate the wall thickness—which is believe to related to the stability of the mesoporous silica particles. In figure 2.22, d-spacing, pore size and wall thickness of the MSNs under different synthetic conditions are compared. Higher pH environments lead to smaller lattice pore size and thinner silica framework wall thickness. Lower pHs lead to larger d-spacing. When the initial pH value is 12.56 or larger, the reaction undergoes a different mechanism; the final product is composed of two different particle sizes and the result of the averaging pore size and wall thickness leads to a slightly increasing pore size at high pHs.

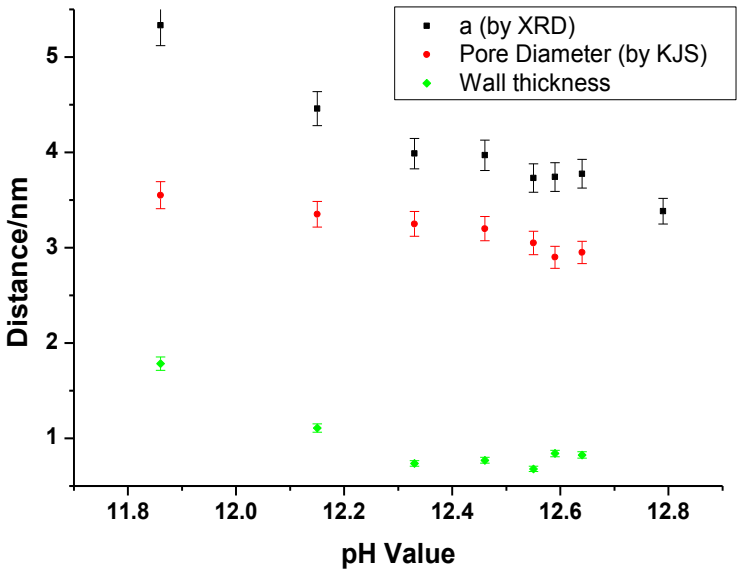

Figure 2.22 The compare of d-spacing, pore size and wall thickness.

2.5 Extended work - gold nanoparticles decorated MSNs

The experiments on the decoration of gold nanoparticles (AuNP) are investigated on samples both before calcination and after calcination. Experiments are briefly as follows: first, 0.3g MSNs and 900µL 3-Aminopropyltriethoxysilane (APTES) was mixed in 19mL toluene; the suspension was then stirred for 24 hours; filtered and dried to get samples surface functionalized with amino groups; the mixing of 15mg of functionalized MSNs with 150µL 25mM $HAuCl_4$ aqueous solution in 15mL EtOH; followed by stirring the mixture under room light for several days to get the AuNP/MSNs composites.

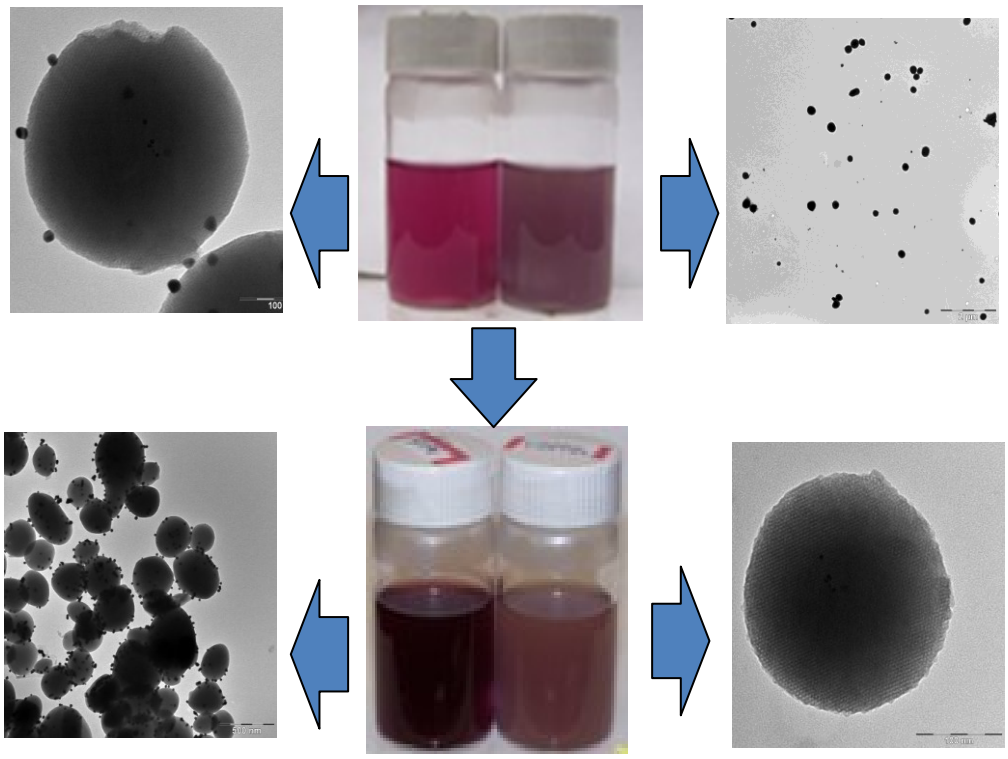

Figure 2.23 Gold decorated outside of uncalcinated MSNs (left) and inside the pores of calcinated MSNs (right) with different reaction time 7days (up) and 18 days (down).

When $HAuCl_4$ solution first mixed with the functionalized MSNs, the color of the solution immediately became a darker yellow than the original yellowish color of $HAuCl_4$ solution. This phenomenon might indicate the complexion of $AuCl_4^-$ with the amino group. After 7 days stirring the mixture under room light (figure 2.23 up-row), $AuCl_4^-$ became partially reduced, with the surface of the MSNs serving as nucleation sites. AuNPs are selectively grown on the surface of the uncalcinated MSNs (figure 2.23 top left). And in the case of calcinated MSNs, AuNPs are also formed based on the color change, while no gold nanoparticles are found outside of the MSNs particles (figure 2.23 up right). We conclude that all the AuNPs are formed in the pore channels. After 18 days of reaction (figure 2.3 bottom-row), the composite system was stable, with more gold nanoparticles formed.

We also investigated the XRD and UV-Vis of the system to confirm the formation of the formation of AuNPs.

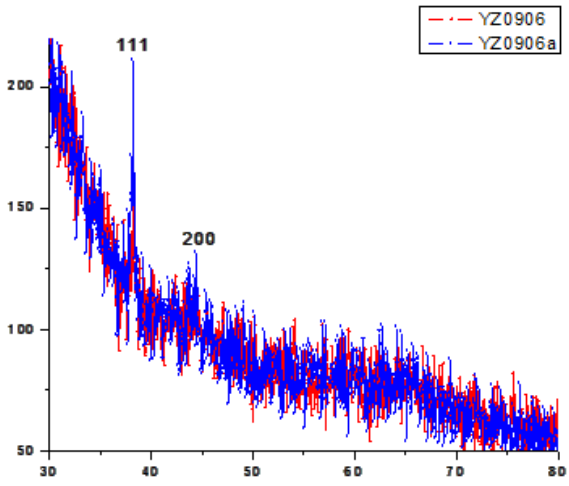

Figure 2.24 XRD pattens of AuNPs out of the particles (YZ0906) and in the pore(YZ0906a) after 18 days of reaction.

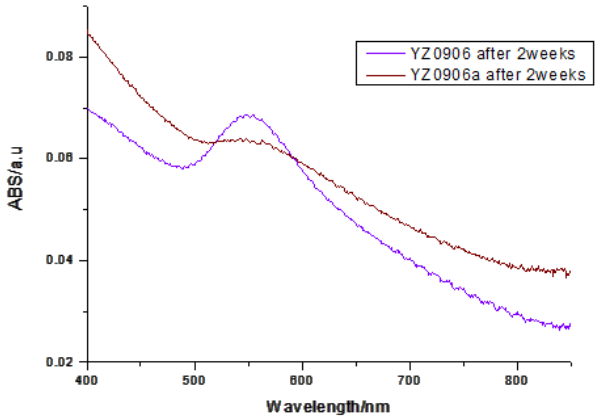

Figure 2.25 UV-Vis transmission spectra of AuNPs out of the particles (YZ0906), and in the pore (YZ0906a) after 18 days of reaction.

2.6 Conclusion

In this chapter, we report how ordered mesoporous silica nanospheres (MSNs) were successfully synthesis with a surfactant mediated approach and a modified Stöber method. We synthesized monosized MSNs with control the pH in the range between 11.8 and 12.55. The particle size can be controlled between 30 to 200 nm through the tuning of initial pH values. A mixture of two-size MSNs is formed for pHs higher than 12.6, and various sizes are found for different pHs. The decoration of gold nanoparticles (AuNPs) can be controlled at the surface or into the pores of MSNs.

References

1. Stöber, W.; Fink, A.; Bohn, E., Controlled growth of monodisperse silica spheres in the micron size range. *Journal of Colloid and Interface Science* **1968,** *26* (1), 62-69.

2. Grün, M.; Lauer, I.; Unger, K. K., The synthesis of micrometer- and submicrometer-size spheres of ordered mesoporous oxide MCM-41. *Adv Mater* **1997,** *9* (3), 254-257.

3. Yano, K.; Fukushima, Y., Particle size control of mono-dispersed super-microporous silica spheres. *Journal of Materials Chemistry* **2003,** *13* (10), 2577-2581.

4. Slowing, I.; Vivero-Escoto, J.; Wu, C.; Lin, V., Mesoporous silica nanoparticles as controlled release drug delivery and gene transfection carriers. *Advanced Drug Delivery Reviews* **2008**, 1278-1288.

5. Kumar, R.; Chen, H.-T.; Escoto, J. L. V.; Lin, V. S. Y.; Pruski, M., Template Removal and Thermal Stability of Organically Functionalized Mesoporous Silica Nanoparticles. *Chemistry of Materials* **2006,** *18* (18), 4319-4327.

6. Barrett, E. P.; Joyner, L. G.; Halenda, P. P., The Determination of Pore Volume and Area Distributions in Porous Substances. I. Computations from Nitrogen Isotherms. *J Am Chem Soc* **1951,** *73* (1), 373-380.

7. Kruk, M.; Jaroniec, M.; Sayari, A., Application of Large Pore MCM-41 Molecular Sieves To Improve Pore Size Analysis Using Nitrogen Adsorption Measurements. *Langmuir* **1997,** *13* (23), 6267-6273.

Chapter Three: Microwave Assisted Synthesis of Mesoporous Silica Nanospheres

3.1 Microwave dielectric heating

Microwave irradiation is electromagnetic radiation in the frequency range 0.3 to 300 GHz, which corresponds to wavelengths of 1 mm to 1 m. For domestic microwave ovens, the frequency used for microwave dielectric heating is 2.45 GHz, which corresponds to a wavelength of 12.2 cm. Microwaves, as all electromagnetic waves, contain electric and magnetic field components. The heating mechanism involves two main processes, namely dipolar polarization and ionic conduction.[1] The electromagnetic radiation of microwave produces an oscillating field that forces the dipoles or ions to oscillate in synchrony with the electric field. Heat is generated through molecular frictional and dielectric losses associated with the oscillation. The 2.45 GHz microwave photon energy is around 1×10^{-5} eV, which is comparable to molecular rotational energy. If the frequency of the field is much higher than the response time of the dipoles or if the time required to change the direction of the electric field is longer than the response time of the dipoles, then there can be no heating.

Microwave irradiation as a heating method has found a number of applications in organic[2] and inorganic[1] syntheses. Microwave irradiation has exhibited very rapid growth in its applications to materials sciences because of its unique reaction mechanisms, e.g., a rapid volumetric heating which results in a dramatic increase in reaction rates. Recently, microwave heating has also been used in the synthesis of ordered mesoporous materials such as chloropropyl functionalized mesoporous silica SBA-15,[3] cubic mesoporous silica SBA-16,[4] and mesoporous anatase TiO_2.[5]

In this chapter, a microwave-assisted heating procedure has been used to synthesize mesoporous silica nanospheres (MSNs). As a result of microwave assisted synthesis, well crystallized MSNs with narrow size distribution have been formed. Additionally, for MSN particles, we proposed in this chapter a mathematical technique, based on particle size and pore structure, to calculate the anticipated surface area of mesoporous nanospheres. We compare calculated and measured surface areas by the BJH-KJS experimental approach.

3.2 Experiments

3.2.1 Materials

Sodium hydroxide with a purity of 98.7% was obtained from J. T. Baker. Cetyltrimethylammonium bromide (CTAB) was purchased from Alfa-Aesar with a purity of 99+%. Tetraethoxysilane (TEOS) with 98% purity was purchased from Acros. HPLC grade ethanol was supplied by Sigma-Aldrich. All chemicals were used as received without further purification. Triply distilled water was utilized for the solution preparation and washing procedure.

3.2.2 Microwave-assisted synthesis of MSNs

The microwave heating system that was used consists of a modified standard home microwave unit, which is schematically represented in figure 3.1, a round bottom flask that is shown supported by a Teflon block, and a reflux tube attached outside of the microwave oven. Detailed experiments parameters for reactions are shown in Table 3.1. The experimental procedure consisted of first preparing 1.0 M NaOH in advance by dissolving 40.0 g NaOH in 1000 mL of distilled water. In this pre-step, the 10.0 ml of 1.0 M NaOH solution was first added

to 490 mL of distilled water with constant stirring. Next, 1.0 g cetyltrimethylammonium bromide (CTAB) was added to solution mentioned above. After the CTAB was totally dissolved in the solution, 6.0 mL of tetraethoxysilane and 7.0 mL ethanol were added to the solution. The resultant homogenous solution was transferred to a 1L round-bottom bottle and placed in a microwave refluxing system and irradiated at 500 W for 30 min. The microwave induced reaction was conducted using ambient air. Following the reaction, the suspension was cooled in air, then the precipitate was filtered and washed with methanol 3 times and dried in air. The as-prepared white powder was calcined at ~540°C for 3 hours to remove any residual CTAB.

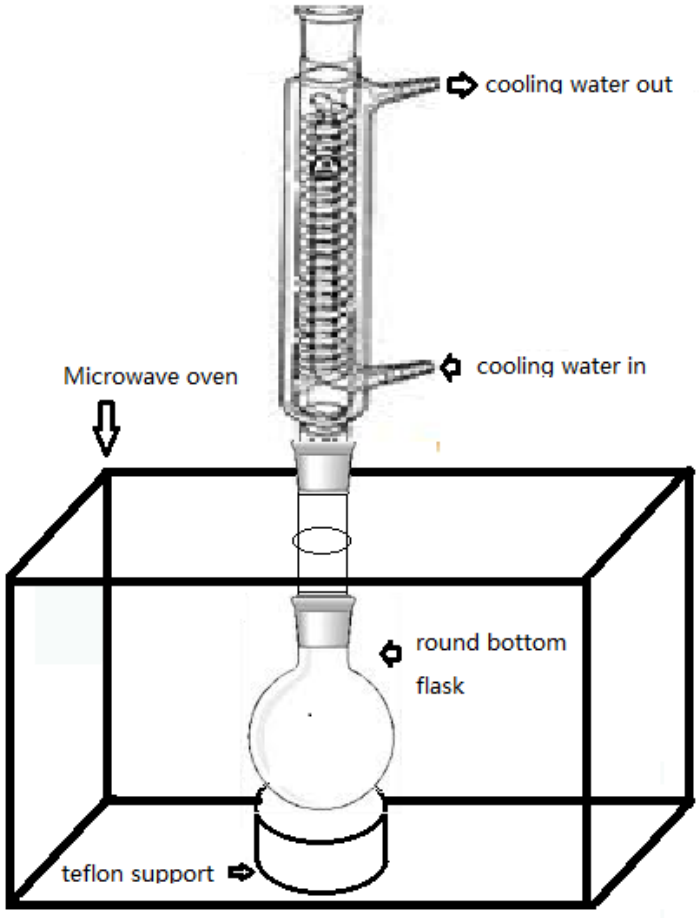

Figure 3.1: Diagram of the microwave-assisted heating apparatus.

Table 3.1: Experiments performed using microwave-assisted synthesis of MSNs.

	H_2O	NaOH 1M	Before Reaction	CTAB	TEOS	EtOH
Sample	mL	mL	pH	g	mL	mL
YZ0941	490	14.0	12.58@23.0	1.005	6.0	7.0
YZ0940	490	12.0	12.45@22.9	1.010	6.0	7.0
YZ0935	490	10.0	12.35@20.5	1.019	6.0	7.0
YZ0936	490	8.0	12.26@20.5	1.010	6.0	7.0
YZ0937	490	6.0	12.15@20.5	1.027	6.0	7.0
YZ0938	490	4.0	11.97@20.5	1.006	6.0	7.0
YZ0939	490	2.0	11.72@20.5	1.019	6.0	7.0

* PH value are provided in the format "pH value @ temperature," in Celsius degrees.

3.3 Characterization

3.3.1 Low-angle powder X-ray diffraction (XRD)

The powder samples before calcination and after calcination were investigated by low-angle powder X-ray diffraction (XRD). Low-angle XRD measurements were performed using a PANalytic X-ray diffractometer with voltage of 45 kV and current of 40 mA; scattering angle range from 1-7º, and step size 0.005º. Monochromatic Cu Kα (λ=1.54 Å) radiation was used with a nickel filter.

3.3.2 Dynamic light scattering (DLS)

Dynamic lights scattering data were recorded using a Brookhaven Instrument Co. BIC 90Plus particle size analyze at 90° detection angle. For this instrument, the analytical range of particle sizes is < 1 nm to 6 μm. Sample for DSL measurement were prepared as follows: a small amount of powder sample was first dispersed in double distilled water, then the suspension was sonicated for at least 5 minutes in order to form a well-dispersed suspension. After letting the suspension settle for 5minutes, several drops of upper part of the suspension is transferred to a sample cuvette for DSL measurements.

3.3.3 Transition electron microscopy (TEM)

Transition electron microscopy (TEM) investigations were performed using a Zeiss EM 902 thermionic (tungsten) transmission electron microscope at an accelerating voltage of 80 kV. The samples used for TEM observations were prepared by dispersing samples in ethanol followed by ultrasonic vibration for 5 min, and then a drop of the suspension was placed onto a copper grid coated with a layer of amorphous carbon. Finally the solvent was evaporated in air.

3.3.4 N_2 adsorption-desorption measurement

Nitrogen adsorption-desorption measurements were carried out on a Micromeritics ASAP 2020 volumetric adsorption analyzer at -196 $^{\circ}$C. Before the adsorption analysis, calcined samples were outgassed under a vacuum at 200 $^{\circ}$C in the port of the adsorption analyzer.

3.4 Result and discussion

In our experiments, MSNs with size ranging from 30 to 500 nm have been synthesized using the microwave-assist heating method. Similar conditions as to the water bath heating procedure described in the previous chapter were applied in the microwave assisted synthesis process. PH values ranged from 11.72 to 12.58 were used in the synthesis in order to get monosized nanoparticles. Similar analyses as conducted for the corresponding water bath heating samples (WB-MSNs) were performed on the microwave heating samples (MW-MSNs) and the results compared.

3.4.1 Lattice parameters for synthesis at different pHs

When the pH values were varied in different synthesis, the final products have different values for the various lattice parameters for the XRD measurements performed. In figure 3.2, resultant low-angle XRD patterns are plotted for comparison. Figure 3.2a show the results for samples that have not been calcined. The XRD peak positions are shown to shift to lower angles as the pH value of the reacting solution is increased. Figure 3.2b is converted from figure 3.2a, where now all the 2θ angles are converted into d-spacing. In figure 3.2b, it is easy to see that the d-spacing increases as the pH increases. Figure 3.2c and figure 3.2d show the corresponding XRD and d-spacing converted XRD patterns of the calcined MSN samples, respectively. The same trend in the d-spacing are shown in the calcinated samples as the pH is varied. Comparing the d-spacing of the sample before and after calcination, it is found that all the sample d-spacing become smaller after calcination. This same phenomenon as found for the WB-MSN samples indicates the removal of the template from the pore channels.

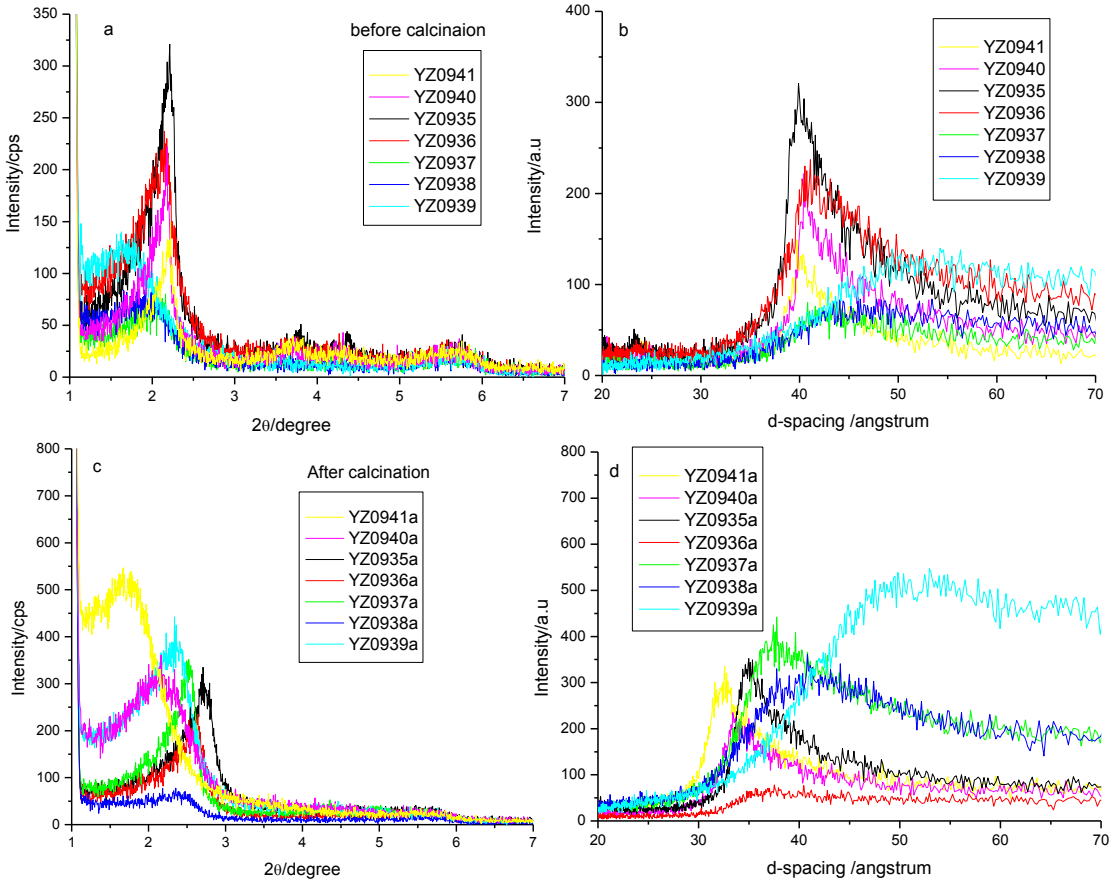

Figure 3.2 XRD patterns of MSN samples synthesis at different pHs: before calcination (a, b) and after calcination (c, d).

3.4.2 Particle size by DLS measurement

The DSL characterizations provide the hydrodynamic particle size distribution of the samples. As table 3.2 shows, the average particle size determined by measuring a number of particles is provided.

Table 3.2 Hydrodynamic particles size for the calcinated samples

Sample name	Initial pH	DSL particle sizes (nm)
YZ0935a	12.35	144.8±7.2
YZ0936a	12.26	100.0±5.0
YZ0937a	12.15	82.0±4.1
YZ0938a	11.97	53.8±2.7
YZ0939a	11.72	28.8+1.4

It is found that the pH value of the synthetic solution provides good control over the resultant particles size. We observed that for an initial pH of the solution lower than 12.35, the particle size monotonically grow larger with pH increase from 11.72 up to the 12.35 value. For pH values greater than 12.35 the hydrodynamic size does not increase with increasing pH value. This indicates a change in the reaction mechanism.

3.4.3 Morphology analysis through TEM measurements

We investigated the morphology of the MSNs samples after calcinations. The results are shown in figure 3.3 to figure 3.9. Spherical particles were found for all syntheses conditions, although some flakes are also present when high pH conditions were used (figure 3.8 and 3.9). Similar to the result from DSL, we know that when the synthetic pH values are higher than 12.35, more than one particle formation mechanisms is active. While, on the other hand, when the reaction pH is lower than 12.35, only a monosized distribution is found in both the TEM and DSL measurements. We roughly estimated the particles size by TEM as follows: sample

YZ0939a that was synthesized at pH 11.72, has a particle size of about 25 nm (figure 3.3); Sample YZ0938a that was prepared at pH 11.97 has a particle size around 50 nm (figure 3.4); Sample YZ0937a that was prepared at pH 12.15 has a particle size around 80 nm (figure 3.5); Sample YZ0936a that was prepared at pH 12.26 has a particle size around 100 nm (figure 3.6); Sample YZ0935a that was prepared at pH 12.35 with particle size around 110 nm (figure 3.7). Although the sized estimated by TEM graphs are very approximate with errors estimated to be more than 10%, they still are in good agreement with the DSL result.

We have also investigated the pore structure directly from the TEM graphs. The ordering of the mesopores is 2D hexagonal phase, which is also the know structure for the well-known mesoporous silica material MCM-41. We found that the ordering in the smaller particles is not as consistent as with larger particles, and we found that the pore sizes of the mesopores are directly correlated to the d-spacing in our synthesis conditions. We note that the smaller d-spacing leads to better ordering.

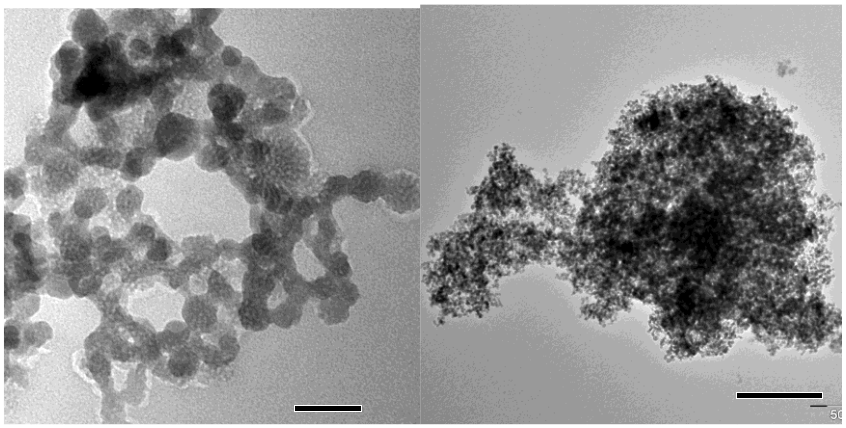

Figure 3.3: TEM graphs of sample YZ0939a. (Average particles size ~25 nm).

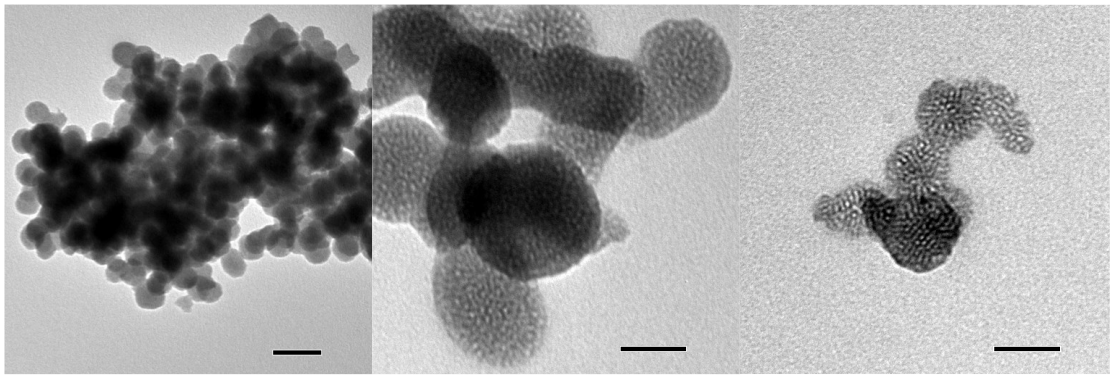

Figure 3.4: TEM graphs of sample YZ0938a. (Average particles size ~50 nm).

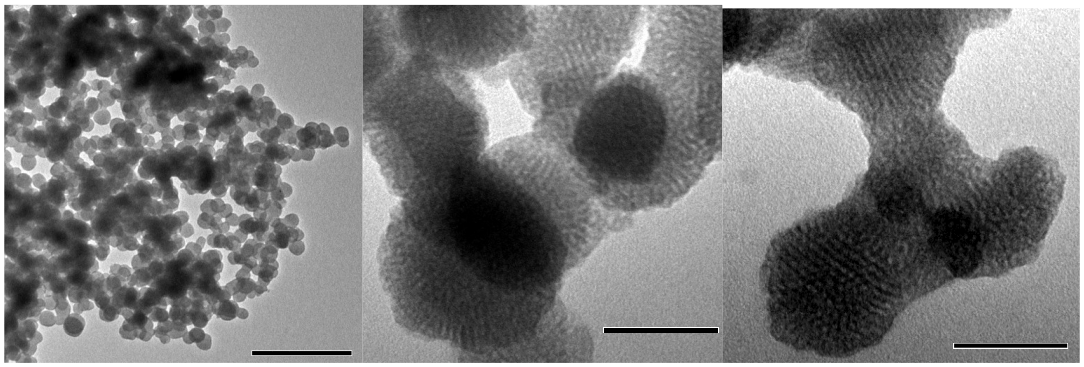

Figure 3.5: TEM graphs of sample YZ0937a. (Average particles size ~80 nm).

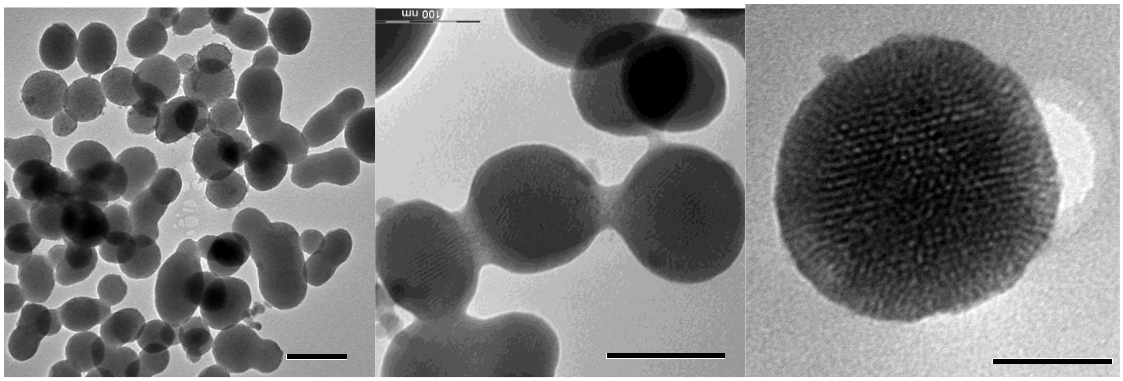

Figure 3.6: TEM graphs of sample YZ0936a. (Average particles size ~100 nm).

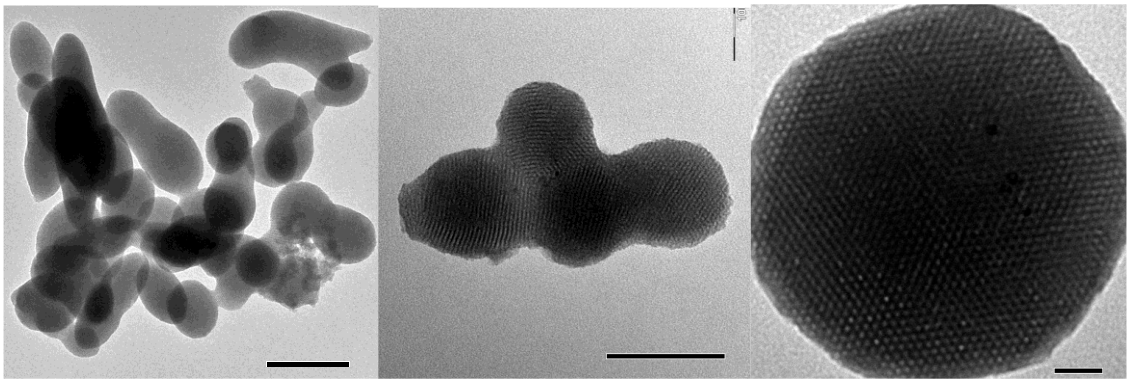

Figure 3.7: TEM graphs of sample YZ0935a. (Average particles size ~110 nm).

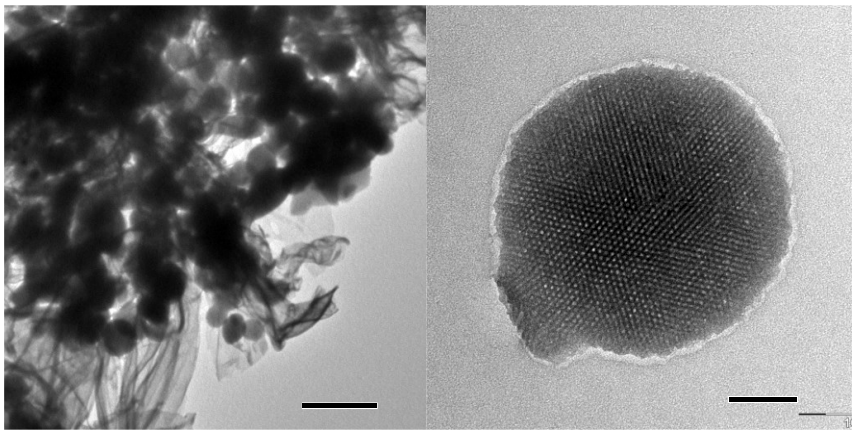

Figure 3.8: TEM graphs of sample YZ0940a.

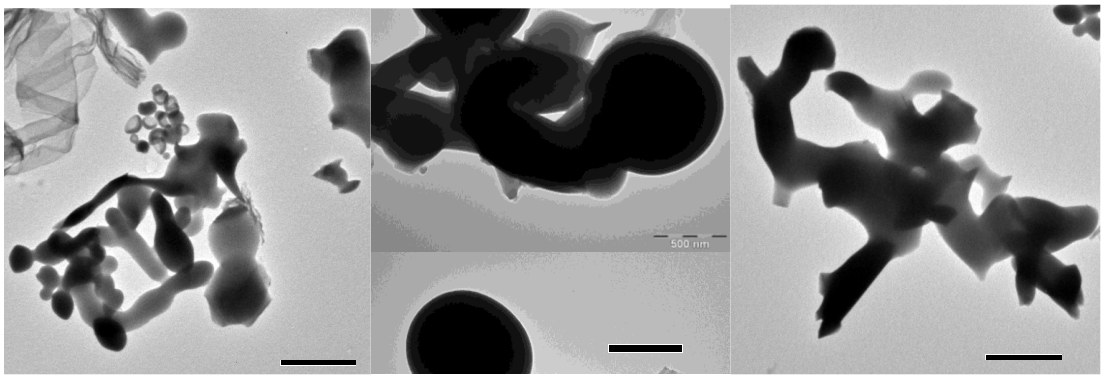

Figure 3.9: TEM graphs of sample YZ0941a.

3.4.4 Surface area and pore size distribution

Nitrogen adsorption-desorption isotherms were measured in order to investigate the surface properties of the calcinated MSN samples. The isotherm plots of all the samples are collected in figure 3.10; and the corresponding structure parameters calculated by BJH method.

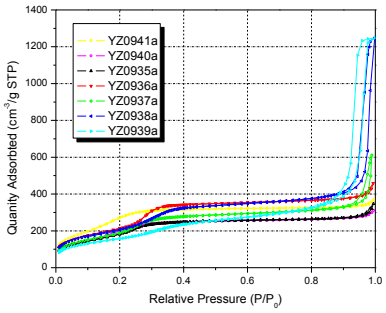

Figure 3.10: N_2 adsorption/desorption isotherm plots for calcinated samples.

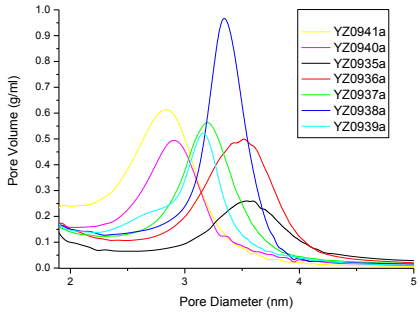

Figure 3.11: BJH-KJS pore size distributions for of calcinated samples.

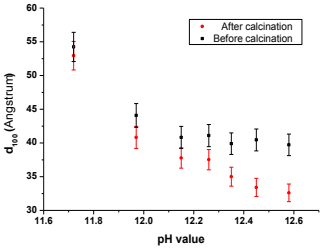

Figure 3.12: d_{100} of MSNs before and after calcinations.

3.4.5 D-spacing of the samples prepared from different pHs

The hexagonal phase d_{100} (d-spacing of (100) lattice structure) of MSNs for different synthesis pHs are plotted in figure 3.11. As found for the WB-MSN samples, calcinations at 540ºC leads to shrinkage of the d-spacing of all the MW-MSN samples. Lower initial pH value leads to larger d-spacing of the sample. The MW-MSNs are found to have essentially the same d_{100} as the WB-MSNs after calcinations, however larger d_{100} observed in the WB-MSNs compared to the d_{100} of MW-MSNs are found after calcination. This is reasonable since the reaction sample is boiled using microwave heating, which means the reaction was carried out at about 100 ºC, while the WB-MSNs reaction temperature was about 80 ºC. This factor might lead to the smaller d_{100} value of the MW-MSNs before calcination, and this difference would vanish after calcination.

3.4.6 Particle size and crystallization

The particles size of the MW-MSNs were analysed by DSL. Similar to WB-MSNs, the particles sizes are smaller at lower pHs, for pHs smaller than 12.35, while for pH higher than 12.35 some ribbon like silica films are formed. This indicates a different mechanism of formation at pH above 12.35. From the TEM images of the MW-MSNs, the framework of the hexagonal ordered pores are observed, and shows much better ordering in the images. This indicates better ordering of the MW-MSNs than the WB-MSNs base on the TEM images.

3.5 Extended work – Improved surface analysis by spherical particle model

Pore structures are well-defined in the MW-MSNs samples, which mean it is possible to use the MW-MSNs as a model system to improve the understanding of the MSNs particles including the surface area, pore size, et al., via a structural model of the mesoporous particle.

3.5.1 The model of spherical particle with cylinder pores.

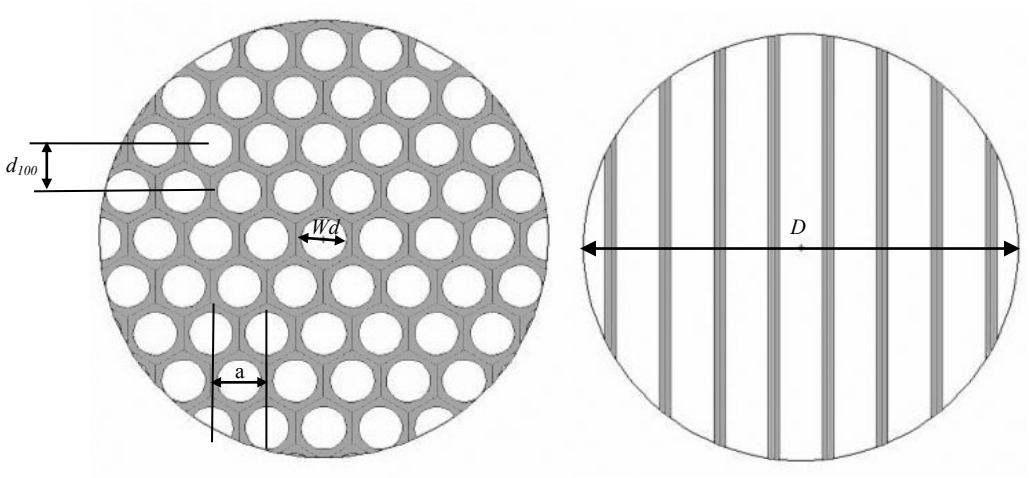

Figure 3.13: Schematic cross-sectional model of a spherical particle with cylinder pores viewed vertically (left) and horizontally (right).

As shown in figure 3.13, we assume there is spherical particle of diameter *D*. The total surface area of the sphere S_o before introducing the pores are can be represent by equation (1):

$$S_o = \pi D^2 \qquad (1)$$

When parallel cylindrical pores with diameter W_d present in the sphere, part of the external surface from the spherical will be taken along with new surface created by the cylinders. We define the number of the pores in a sphere to be *N* and average height of the pores as $\hbar$. Then the new surface area S_{d1} introduced by the cylinder pores can be expressed as follows:

$$S_{d1} = \mathrm{N} \times \pi W_d \times \bar{h} \qquad (2)$$

The pores are aligned with a 2D hexagonal pattern. The virtue domain of one single pore is a hexagon with unit cell parameter *a* in vertical projection (shown in the vertical projection in

figure 3.13). Parameter *a* is equal to the distance between nearest center of cylindrical pores. The area of one virtual hexagon unit A_h can be expressed as:

$$A_h = \frac{\sqrt{3}}{2}\mathrm{a}^2 \qquad (3)$$

So the number of cylinders in one spherical particle *N* can be calculated by the following equation:

$$N = \frac{\pi \mathrm{D}^2}{4} / A_h \qquad (4)$$

Introduced equation (3) to equation (4) we get:

$$N = \mathrm{b}(D/a)^2 \qquad (5)$$

Where the constant $\mathrm{b} = \sqrt{3}\pi/6$.

In order to simply the problem we assume $D \gg W_d$, then every hexagon unit can be approximately regarded as a plain surface. In every unit, the height pore will be the same as the remained surface. So the average height of the pores $\hbar$ can be represented by the average height of the sphere, when viewed as a cylinder with diameter D.

The volume of the perfect sphere V_o should be:

$$V_o = \frac{1}{6}\pi D^3 \qquad (6)$$

Then, we have

$$\bar{h} = V_o / \left(\frac{\pi \mathrm{D}^2}{4}\right) = \frac{2}{3} D \qquad (7)$$

So we can now get total cylinder area S_{dl} by applying equation (4) and (7) to equation (2).

$$S_{d1} = \frac{2}{3} b\pi \frac{D^3 W_d}{a^2} \quad (8)$$

Using the same assumption $D \gg W_d$, the surface area loss from the cylinders are ratio n to the total surface, which can be expressed by following equation:

$$\mathrm{n} = \frac{\pi \mathrm{W_d}^2}{4} / \mathrm{A}_h \quad (9)$$

So we can get the total surface area of the external surface S_{e1} and total surface area of the porous sphere S_t .

$$S_{e1} = (1-n)S_o = \pi D^2 (1 - \mathrm{b}\left(\frac{W_d}{a}\right)^2) \quad (10)$$

$$S_{t1} = S_{d1} + S_{e1} \quad (11)$$

The total pore volume V_{d1} and framework volume V_1 can be expressed as follows

$$V_{d1} = N \times \bar{h} \times \frac{\pi {W_d}^2}{4} = \frac{\pi b D^3}{6} (\frac{W_d}{a})^2 \quad (12)$$

$$\mathrm{V_1} = \mathrm{V_o} - \mathrm{V_{d1}} = \frac{1}{6} \pi D^3 \frac{a^2 - b\mathrm{W_d}^2}{a^2} \quad (13)$$

3.5.2 Spherical particle model in MSNs

Before the mesoporous silica nanospheres are applied to the model, we have the measureable parameters that includes d_{100} from XRD, total surface area S_t and pore volume V_d from N_2 adsorption, Particle size D from DSL.

When the density of the silica ρ is introduced, we have weight of particle G as follows:

$$G = \rho V_1 \quad (14)$$

Then the pore volume V_d of the MSN is

$$V_d = V_{d1}/G = \frac{bW_d{}^2}{\rho(a^2 - bW_d{}^2)} \quad (15)$$

We can get $W_d{}^2$ from equation (15)

$$W_d{}^2 = \frac{a^2 \rho V_d}{b(1+\rho V_d)} \quad (16)$$

In the hexagonal unit, we have

$$a = \frac{2\sqrt{3}}{3} d_{100} \quad (17)$$

Then

$$W_d = \frac{2}{\sqrt{3b}} d_{100} \sqrt{\frac{\rho V_d}{1+\rho V_d}} \quad (18)$$

Where the constant $2/\sqrt{3b} = 2\sqrt{2}/(\sqrt[4]{3}\sqrt{\pi}) = 1.213$

This W_d is the same as the pore size calculated by BJH-KJS model[6], which assumed an infinite structure of uniformed cylindrical pores.

Accordingly, the framework wall thickness is defined as: $t_w = a - W_d$

The total surface area provides by the cylindrical pores S_d is

$$S_d = \frac{S_{d1}}{G} = 4b \frac{W_d}{(a^2 - bW_d{}^2)\rho} \quad (19)$$

We can also simply the equation into

$$S_d = \frac{4V_d}{W_d} \quad (20)$$

Due to the flat surface approximation, the surface area of provide by the pores are independent from the particles size. But the outer surface area S_e will be controlled by the particles size. We have

$$S_e = S_{e1}/G = 6/\rho D \qquad (21)$$

So the diameter of the particle can be derived as

$$D = \frac{6}{\rho} \frac{W_d}{S_t W_d - 4V_d} \qquad (22)$$

So the surface area of the MSNs can be calculated. As shown in table 3.3, the pore size, wall thickness, and surface area are calculated using the spherical particle model. Surface area calculated by BET method is also listed in order for comparison. It is found that surface area calculated from BET method are quite different with the one derived from our model. It is interesting to find out the reason. First, we know that the adsorption data are measured on the powder samples. In the stacking condition is a factor that may affect largely on the surface area because the aggregation of the particles will take the out surface area of the particles. In the meantime, some pores would be generated in the stacking intervals, which means over estimate in the pore volume and pore surface area. Aslo the calcinate conditions are not always perfectly remove the organic surfactant, the remaint of the surfactant might carbonized and stay in the pore, which will largely reduce the pore volume for the samples.

Base on the factors we have analyzed, it is clear that the pore contribute all the pore volume and most of the surface area. We suggest that a factor defined as f=$S_{o,cal}$/ $S_{o,BET}$ can be used to evaluate the pore opening and/or calcination completion for the mesoporous materials. Where when the valve f=1 means a perfect pore opening and best dispersed sample conditions,, and

when f<<1 indicates that the pore are largely filled with either carbonated surfactant or other impurities.

Table 3.3 Pore diameter and wall thickness calculated by the model

Sample	D (nm)	d_{100} (nm)	V_d (ml/g)	W_d (nm)	t_w (nm)	S_d (m^2/g)	S_e (m^2/g)	S_o (m^2/g)	BET S_o (m^2/g)
YZ0935a	144.8	3.50	0.6171	3.22	0.82	766.2	18.8	785.1	669.6
YZ0936a	100.0	3.75	0.8377	3.66	0.67	914.5	27.3	941.7	781.7
YZ0937a	82.0	3.78	1.0522	3.83	0.53	1099.3	33.3	1132.6	689.6
YZ0938a	53.8	4.08	2.0518	4.48	0.23	1832.0	50.7	1882.7	755.0
YZ0939a	28.8	5.29	2.0304	5.80	0.31	1399.2	94.7	1493.8	575.2

***** Density of the silica ρ applied for calculation is 2.2 g/ml; D: particle size from DSL; d_{100}: interplanar spacing from XRD; V_d: pore volume from adsorption data; W_d: primary mesopore size calculated using eq 18; t_w: wall thickness; S_d: surface area of primary mesopores calculated from Vp S_e: external surface area; S_o : total surface area; BET S_o : total surface area derived from BET method.

3.6 Conclusion

We have synthesized mesoporous silica nanosphere with controlled particle size and pore condition with a microwave assisted heating method. The MW-MSNs are showed better crystallization as to the WB-MSNs. pH value in the synthesis can be applied as the only control parameter to tune the particle size and pore size. Also a mathematical model have been pro proposed to calculate the surface are and pore volume of the MSN. A factor f=$S_{o,cal}$/ $S_{o,BET}$ evaluation of the pore opening condition of the as- prepared MSNs.

References

1. Bilecka, I.; Niederberger, M., Microwave chemistry for inorganic nanomaterials synthesis. *Nanoscale* **2010,** *2* (8), 1358-1374.

2. de la Hoz, A.; Diaz-Ortiz, A.; Moreno, A., Microwaves in organic synthesis. Thermal and non-thermal microwave effects. *Chem Soc Rev* **2005,** *34* (2), 164-178.

3. Eko, S.; Prasetyanto, A.; Lee, S.-C.; Park, S.-E., Microwave synthesis of large pored chloropropyl functionalized mesoporous silica with p6mm, Ia-3d, and Im3m structures. *Microporous Mesoporous Mater* **2009,** *118*, 134-142.

4. Hwang, Y. K.; Chang, J.-S.; Kwon, Y.-U.; Park, S.-E., Microwave synthesis of cubic mesoporous silica SBA-16. *Microporous and Mesoporous Materials* **2004,** *68* (1–3), 21-27.

5. Jia, X.; He, W.; Zhang, X.; Zhao, H.; Li, Z.; Feng, Y., Microwave-assisted synthesis of anatase TiO 2 nanorods with mesopores. *Nanotechnology* **2007,** *18* (7), 075602.

6. Kruk, M.; Jaroniec, M.; Sayari, A., Application of Large Pore MCM-41 Molecular Sieves To Improve Pore Size Analysis Using Nitrogen Adsorption Measurements. *Langmuir* **1997,** *13* (23), 6267-6273.

Chapter Four: Hydrogen Release Properties of Pretreated Ammonia-borane

4.1 Introduction

Ammonia-borane (borazane, AB, NH_3BH_3) has been considered as a promising on-board hydrogen storage medium due to its high storage capacity (19.6 wt. %) and moderate dehydrogenation temperatures. The thermal decomposition of solid AB includes three consecutive steps, occurring at around 110, 150, and > 500 °C, with about 6.5 wt. % (with respect to the mass of AB) hydrogen released in each step.[1] However, utilization of AB as a chemical hydrogen storage material for mobile applications is impeded by the formation of borazine and unfavorable dehydrogenation kinetics, e.g., long induction period and low hydrogen release rate at low temperatures (< 85 °C).[2] Several approaches have been discussed to accelerate the thermal decomposition of solid AB; including compositing AB with micro- or mesoporous materials[2-3], catalyzing the thermolysis over transition metals,[4] adding chemical promoters likes NH_4Cl and LiH,[5] and dispersing AB in ionic liquids.[6] These options bring additional species, which itself does not release hydrogen at temperatures less than 85 °C, to the system and thus they cause a reduction in the hydrogen storage capacity.

Autrey and co-worker[7] found that the formation of diammoniate of diborane (DADB, $[(NH_3)_2BH_2]^+[BH_4]^-$) is a first step for hydrogen release from solid AB. Also, they observed that the induction period for hydrogen release is lowered dramatically for the sample that is obtained by quickly cooling AB down to room temperature from a high temperature. The latter finding provides an option to accelerate the dehydrogenation kinetics of solid AB without introducing other components. However, no detailed studies on this approach are available. Moreover,

information on the thermal decomposition of AB preheated at high temperatures will advance our understanding of the dehydrogenation mechanism of solid AB.

In this study, we investigated the effect of thermal treatments on dehydrogenation kinetics in detail and provide new insights into the mechanism of hydrogen release from solid AB. Thermal pre-treatment and hydrogen release measurements were performed in a high-pressure differential scanning calorimeter (DSC). The preheated AB was characterized by X-ray diffraction (XRD) and Fourier transform infrared–attenuated total reflectance (FTIR-ATR) spectroscopy. We found that thermal treatment significantly enhances the rate of hydrogen release and is comparable to the AB doped with NH_4Cl in regards to desorption of the first mole of hydrogen. Also, the induction period is decreased as the preheating period is increased; new species, including linear dimers of aminoborane (LDAB, $NH_3BH_2NH_2BH_3$) and other oligomers or polymers, form during the thermal treatment. Additionally, we observed that only LDAB is formed for a preheating period of less than 3 hours, whereas other oligomeric or polymeric species are detected for longer preheating periods. We surmise that oligomers or polymers (or both) form a solid solution with AB and DADB, causing a depression in the melting temperature of AB. These findings confirm the occurrence of linear dimers in the thermal decomposition of solid AB and provide a strategy to accelerate the thermolysis kinetics of solid AB at low temperatures without any additives.

4.2 Experiments

4.2.1 Materials

Ammonia-borane (AB) with a purity of 97 % was obtained from Sigma-Aldrich. Ammonia chloride was purchased from Sigma-Aldrich with a purity of 99.99 %. Methanol with

a purity of 99.9 % was supplied by Fisher Scientific. All chemicals were used as received without further purification. Deionized (D. I.) water was produced in our lab with a resistivity of 18 MΩ cm^{-1}.

4.2.2 Thermal pre-treatment

Thermal pre-treatment was performed using a high-pressure differential scanning calorimeter (DSC), specifically; the instrument used is the Micro-DSC VII (SETARAM). High-pressure cells with a volume of 0.33 mL were made of Hastelloy and can be operated at temperatures between -40 to 120 °C. The pressure of sample cell was measured using a CET9005GY7 pressure transducer (SensorTechnics, 0 to 5 bar). Approximately 70 mg of AB was put in the sample cell; the reference cell was kept empty. The cells were maintained at 25 °C for 5 minutes and then heated to 80 °C at 1 °C/min, followed by maintaining this temperature for 2 to 4 hours. Finally, they were cooled down to 25 °C at 3 °C/min. The temperature, heat flow, and pressure of the sample cell were collected by the SETSOFT interface. The pressure in the sample cell was predominantly dependent on the release of gases from AB and hardly affected by the temperature of the cell, because the volume of gas phase in the cell is relative small compared with that in external pipelines and fittings. Unless noted elsewhere, preheated samples were kept in a refrigerator for two weeks before use.

4.2.3 NH_4Cl-doped AB.

Typically, 40 mg of NH_4Cl was dissolved in 15 mL methanol. Then, 50 mg of AB was added to 1 mL of the methanolic NH_4Cl solutions, followed by keeping the solution under ambient temperature and pressure overnight to evaporate most of the methanol. Finally, the

sample was vacuum dried at room temperature for 3 hours to remove residual methanol, and then it was placed in a refrigerator.

4.3 Measurement and simulations

4.3.1 Wide angle XRD and FTIR-ATR measurements

Wide angle XRD measurements were performed using a PANalytic X'Pert RPO X-ray diffractometer equipped with a Cu Kα radiation source, graphite monochromator, and nickel filter, in a 2θ range of 20° to 80°, at a step of 0.05°. FTIR-ATR analyses were recorded on a Varian 7000 FTIR using MIRacle ATR accessory, the internal reflection element of which is a Ge single reflection plate. FTIR-ATR spectra were recorded at 2 cm^{-1} resolution from 850 to 4000 cm^{-1}.

4.3.2 DFT simulations

The DFT calculation of AB and linear oligomers was based on the linear zigzag structure, which was discussed previously by Li et al.[8] The geometry of ground-state molecular AB and its derivatives were optimized with no restriction on the symmetry of the initial structure. Both structural optimization and vibrational analysis were implemented using density functional theory (DFT) with functional, specifically, B3LYP.[9] The basis set of split valence type 6-31+G(d), as contained in the Gaussian 03W software package, was used. The charges on all the molecules were set to zero and their spin states to singlet and all the molecules were calculated without considering solvation.

4.3.3 Thermal analysis

A combined TGA-DSC (Q600) technique from TA Instruments was employed to simultaneously detect the weight loss and heat flow during the thermolysis of solid AB. After loading AB (less than 2 mg) into the sample cup (alumina crucible), the sample and reference cups were heated from room temperature to 45 °C at 1 °C/min, and then they were kept at this temperature for 1 hour. Finally, they were heated up to 200 °C at 1 °C/min. All experiments were performed under a nitrogen flow of 100 mL/min. For NH_4Cl-doped AB and pretreated AB (80 °C for 3 hours), triplicate measurements were carried out, and both the weight loss rate and heat flow were reproducible.

4.3.4 Dehydrogenation kinetics

The kinetics of thermal decomposition was conducted using the same DSC instrument described above. The total volume of gas in the sample cell and pipelines with fittings is 2.57 mL. About 12 mg of AB was loaded to the sample cell, while the reference cell was kept empty. The sample and reference cells were maintained at 25 °C for 5 minutes, then they were heated up to 85 °C at 1 °C/min, followed by maintaining at this temperature for 3 hours. A representative experiment involved loading the sample cell with about 12 mg of pristine AB; the sample and reference cells were maintained at 25 ºc for 5 minutes, then heated to 115 °C, and then cooled down to 25 °C at 1 °C/min. For NH_4Cl-doped AB and pretreated AB (80 °C for 3 hours), triplicate measurements were conducted, and the kinetics of thermal decomposition was reproducible.

4.3.5 H_2 release measurements.

Hydrogen release measurements were conducted on the Micro-DSC VII (SETARAM). The total volume of gas in the sample cell and pipelines with fittings is 6.38 mL. First, 3.6 mg of AB was loaded to the sample cell, while the reference cell was kept empty, and then 5.0 mL of ethane at room temperature was injected to the sample cell. The sample and reference cells were maintained at 25 °C for 5 minutes, then they were heated up to 85 °C at 1 °C/min, followed by maintaining at this temperature for 3 hours. After that the cells were cooled down to -40 °C at 3 °C/min, and they were kept at the above temperature for 20 minutes before withdrawing around 10 mL gas from the sample cell. The reason to maintain the cells at -40 °C is to minimize the effect of borazine on the hydrogen measurement, because it could reacts with sulfuric acid to generate extra hydrogen. The gas sample was bubbled through concentrated sulfuric acid in a sealed 30 mL vial that was manually vacuumed using a 10 mL syringe. The gas composition was analyzed using an HP 5890 SII GC equipped with a MolSieve 5A Plot capillary column (30m×0.53mm, Sigma-Aldrich). The carrier gas was argon and its flow rate was set to 3.74 mL min^{-1}. The column temperature was maintained at 35 °C for 4 minutes, and then it was programmed to 255 °C at 10 °C min^{-1}. The total mole number of gas after the thermal Wdetermined after the GC analysis for the given amount of ethane that was provided into the micro-DSC just before the AB thermal decomposition. The uncertainty in moles of hydrogen released was estimated to be within 8 % based on triplicate measurements.

4.4 Results and discussion

4.4.1 Pristine AB

Profiles of temperature, heat flow, and pressure during the thermal decomposition of pristine AB at temperatures between 25 and 115 °C are presented in Figure 4.1.

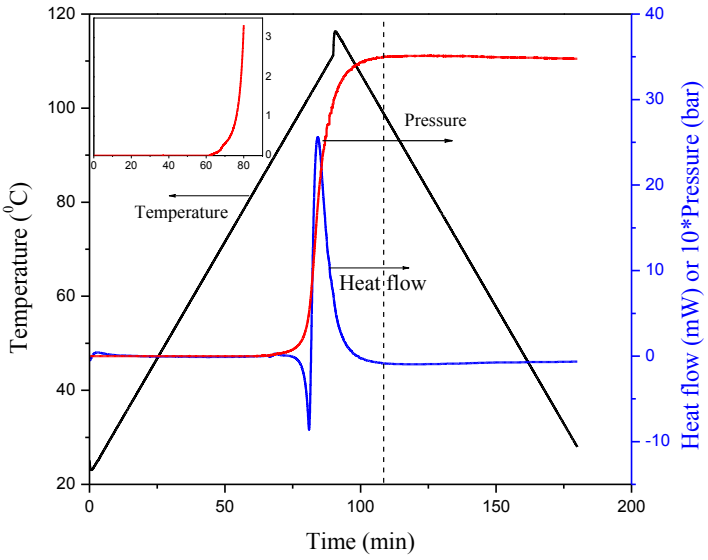

Figure 4.1 Variation of temperature, heat flow, and pressure with time for pristine AB thermal decomposition.

The endothermic process, related to AB melting, starts around 90 °C and maximizes at 102.4 °C, while the exothermic process that corresponds to AB decomposition reaches a maximum at 105.4 °C. Also, it is noted that the pressure starts to increase at a temperature below the onset of AB melting (inset in Figure 4.1); however, the change is relatively small in the first 80 minutes, and then it dramatically increases from 0.34 to 3.43 bars in 20 minutes, followed by asymptotically approaching 3.5 bars. The decomposition is complete after the temperature decreases from 115 to 99 °C (dotted line in Figure 4.1). The pressure increase is mainly due to

the hydrogen release, because previous studies have found that the predominant gas product of AB decomposition at temperatures below 115 °C with a heating rate of 1 °C/min is hydrogen.[1c, 2] Additionally, our measurements suggest that the mole fraction of hydrogen in the gas phase is around 0.92. It should be note here that AB sublimation probably also contributes to the pressure increase besides other volatile products like hydrogen and borazine from AB decomposition.

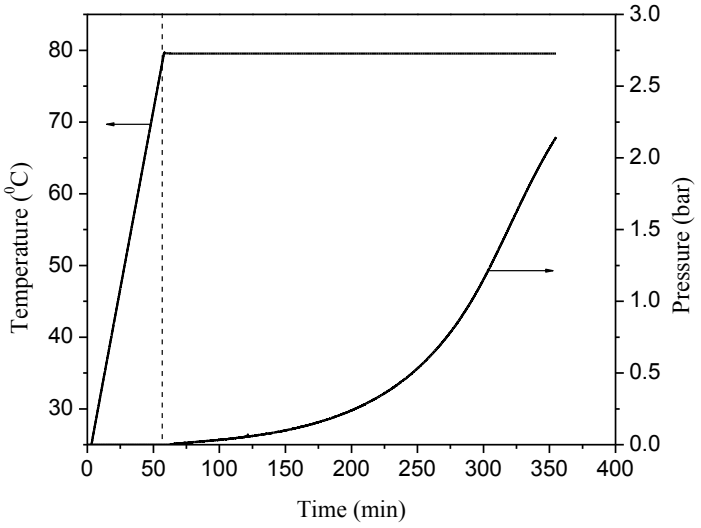

Figure 4.2 Profiles of temperature and pressure in preheating pristine AB.

Heldebrant et al.[5a] reported that hydrogen evolution is observed for pristine AB after maintaining a temperature of 80 °C for ca. 4 hours; 1 mole of hydrogen is desorbed in 17 hours, suggesting that the maximum preheating period at this temperature is less than 4 hours to minimize hydrogen loss during the thermal pre-treatment. Our results, however, indicate that hydrogen release is detected from pristine AB after maintaining the temperature at 80 °C for just 20 minutes, and the pressure increases to 0.16, 0.42 and 1.07 bar in 2, 3 and 4 hours,

respectively, after the temperature reaches 80 °C (Figure 4.2). The difference between our findings and prior results is likely attributable to the material of which the cell that holds AB is made of, since maintaining AB at 80 °C for 12 hours in an open alumina crucible has little effect on the dehydrogenation behavior (Figure 4.3) . However, we cannot exclude that the pressure built up in the close cell affect the hydrogen release, because Palumbo et al. found that the kinetic of hydrogen release from AB at a constant temperature is dependent on the pressure.

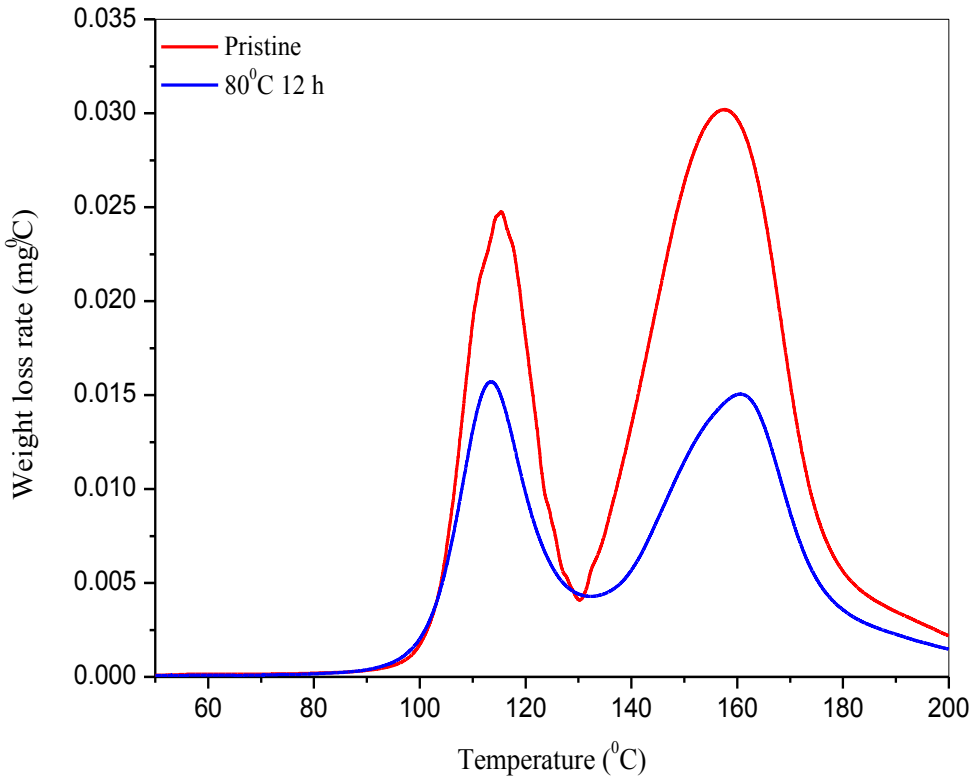

Figure 4.3 Weight loss rate of pristine and pretreated AB.

4.4.2 Preheated AB

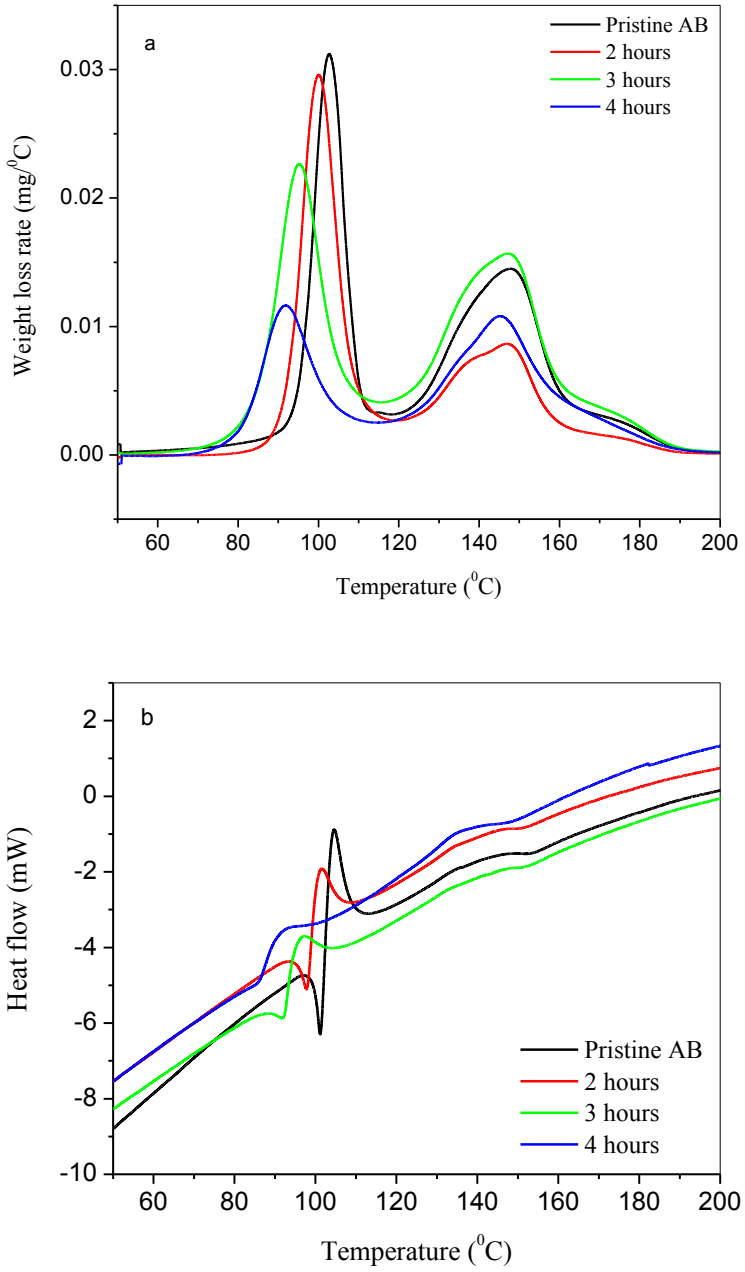

Figure 4.4 TGA-DSC data (a) weight loss rate and (b) thermograph of pristine and preheated AB with different treating periods.

In the thermogravimetric investigations for preheated AB, two principle peaks, attributed to two consecutive dehydrogenation steps, are observed at temperatures below 200 °C; the peak temperatures correspond to maxima in weight loss rates (Figure 4.4a). The first peak temperature shifts to low values as the preheating period increases, while the second peak remains almost stationary. The shift in the first peak temperature is due to the occurrence of other species that readily polymerize or react with AB to generate hydrogen. The existence of other species besides AB can also be inferred from calorimetric measurements. As shown in Figure 4.4b, the peak temperature of preheated AB melting decreases with increased preheating periods, indicating that a solid solution composed of crystalline AB and other species formed in the thermal treatment. Also, the heat adsorbed in preheated AB melting decreases as the preheating period increases from 2 to 4 hours.

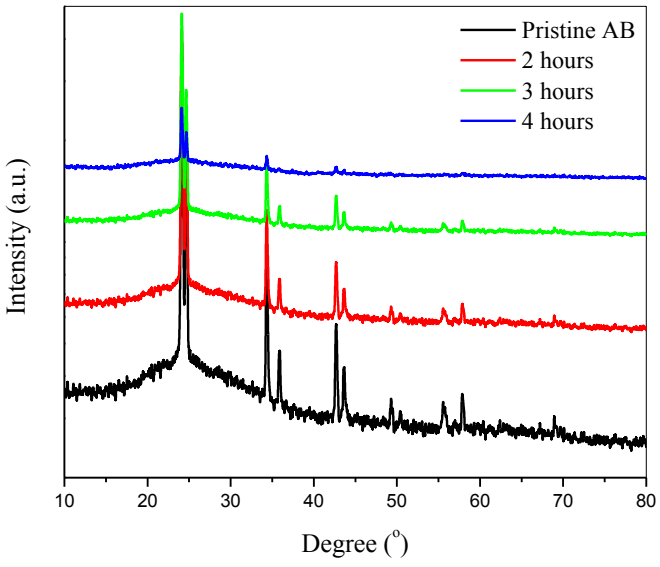

Figure 4.5 XRD spectra of pristine and preheated AB with different treating periods.

Further examination of the calorimetric data reveals that the melting event becomes less important at a preheating period of 4 hours. An explanation to this observation is that the heat desorbed from AB dehydrogenation, which is correlated to the hydrogen release, offsets the heat required for AB melting. However, crystalline AB is still well identified in XRD patterns (Figure 4.5) for the same sample.

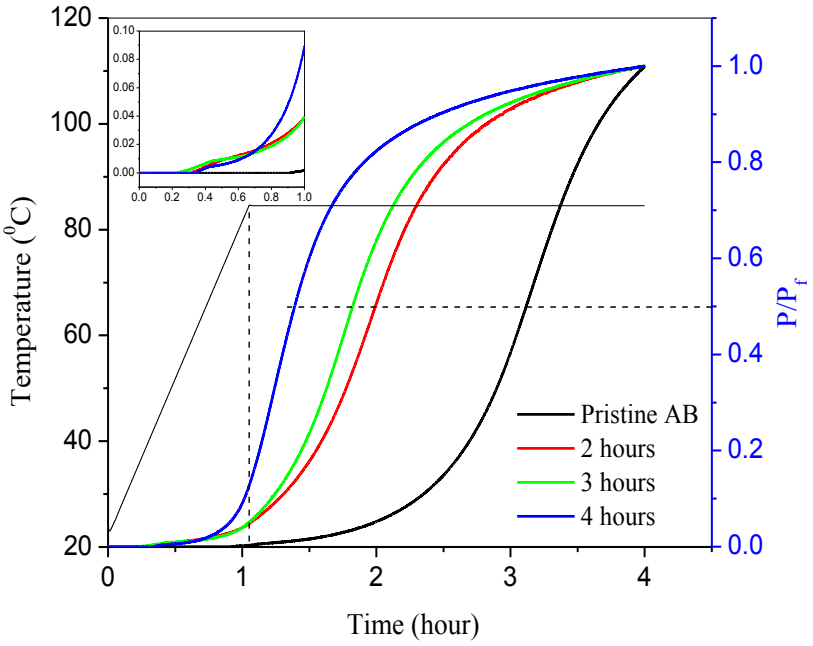

Figure 4.6 Dehydrogenation of pristine and preheated AB with different treating periods at temperatures of 25 to 85 °C.

Figure 4.6 shows the time-dependent relative pressure for pristine and pretreated AB at 85 °C. The finial pressures at the end of the runs are 3.03, 2.9, 2.8, and 2.7 bar for pristine AB and AB held at 80 °C for 2, 3, and 4 hours, respectively. For both pristine and preheated AB, the dehydrogenation kinetics displays a sigmoidal pattern. This behavior is interpreted as indicating

the presence of an active species that forms from AB, followed by reaction with AB to produce hydrogen gas. There are two notable effects associated with preheating: first, hydrogen release starts early for preheated AB compared with pristine AB (inset in Figure 4.6); second, the time, at which the dehydrogenation is 50 % complete (so-called half-time), decreases as the preheating period increases.

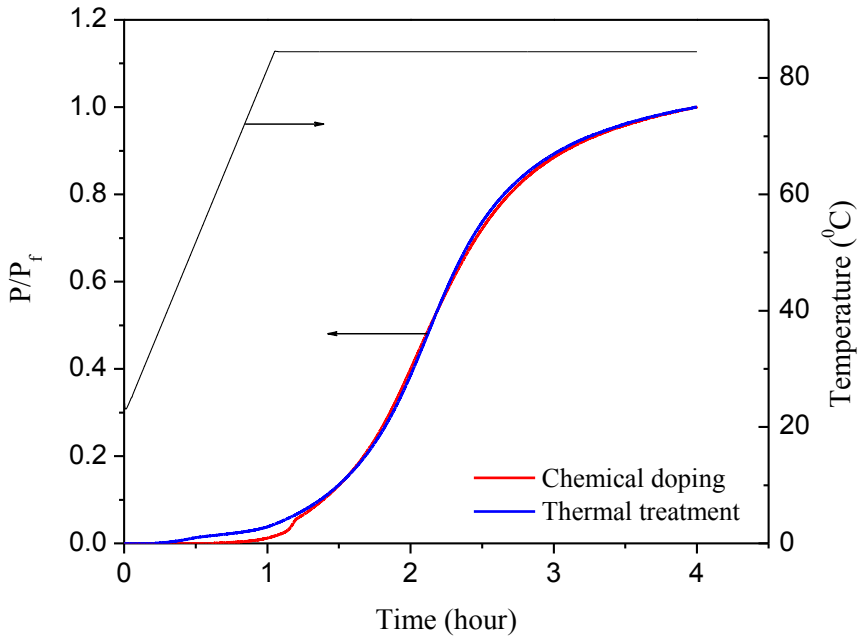

Figure 4.7 Dehydrogenation of chemical doped AB (5.3 wt. % NH4Cl) and thermal treated AB (3 hours at 80 °c) at temperatures of 25 to 85 °C.

As mentioned *supra*, a principal advantage of the thermal treatment over other options is that no other promoters are required to reduce the induction period and to enhance the hydrogen release rate at low temperatures. To clarify this issue more fully, here we compared two approaches: thermal treatment versus chemical doping. Figure 4.7 shows that the thermal

decomposition of preheated AB (3 hours at 80 °C) at 85 °C follows the same pattern as that of NH_4Cl (5.3 wt. %)-doped AB. Also, we observed that the final pressure at the end of run is the same for these two samples. The hydrogen yields for preheated AB (3 hours at 80 °C) and NH_4Cl-doped AB are 7.2 and 7.4 wt. %, respectively. Therefore, the thermal treatment is comparable to the chemical doping with respect to the release of the first equivalent of hydrogen.

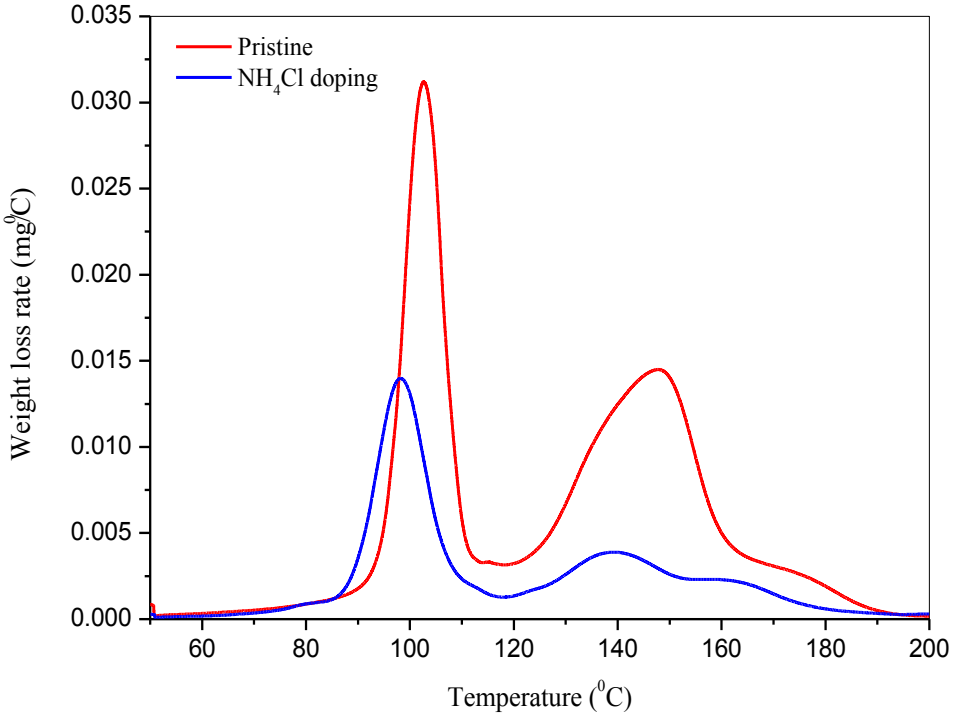

Figure 4.8 Weight loss rate of pristine and chemical-doping AB.

As a further point, it is noted that the chemical doping shifts both the first and second dehydrogenation peak temperatures to lower values (Figure 4.8), whereas the thermal treatment only affects the first dehydrogenation step.

4.4.3 Dehydrogenation mechanism

The results presented above support previous observations in the literature or provide additional mechanistic insight into the elementary processes that lead to hydrogen release during the thermal decomposition of solid AB. One of the recognized schemes is that of Autrey and coworkers[7], who proposed that the release of hydrogen proceeds via three consecutive steps: induction, nucleation, and growth, corresponding, respectively, to formation of a mobile phase, isomerization of AB to form DADB ($[(NH_3)_2BH_2]^+[BH_4]^-$), and bimolecular reaction between AB and DADB; with the net outcome being the liberation of hydrogen. They also proposed that the formation of an ionic polymeric DADB-like species (e.g., $[NH_3BH_2NH_2BH_2NH_3]^+[BH_4]^-$) is possible.[7]

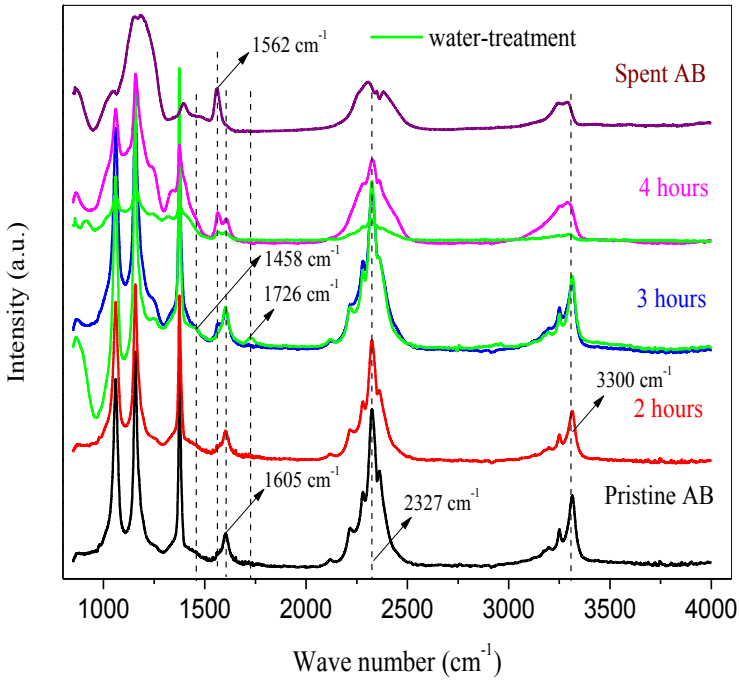

Figure 4.9 Measured IR spectrum pristine and preheated AB with different treating periods at 80 °C, water-treated preheated AB, and partially spent AB (after first mole of hydrogen released).

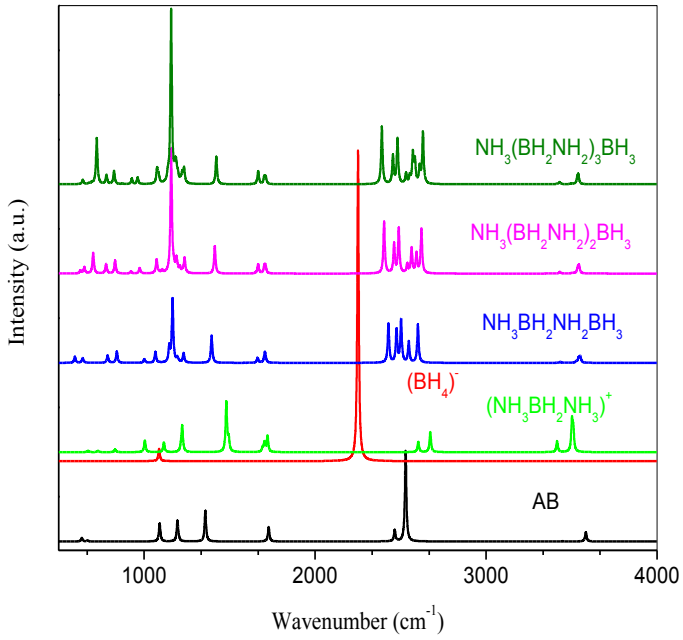

Figure 4.10 Calculated IR spectra of AB, DADB and oligomers of aminoborane.

The mechanism, implicitly, suggests that a polymeric DADB-like species should be detected in the preheated samples, since hydrogen evolution is observed for thermal pre-treatment periods of 2 to 4 hours at 80 °C. However, bands related to N-H bond of $[(NH_3)_2BH_2]^+$ or the B-H bond of $[BH_4]^-$ in the IR spectrum of preheated AB are merged with corresponding bands of AB (Figure 4.9). On the other hand, Figure 4.9 suggests that the polymeric species is not present in the preheated samples with thermal pre-treatment periods of less than 3 hours; moreover, the FTIR spectrum of one of the preheated samples (specifically, the sample pretreated for 4 hours at 80 °C) displays structural features of polyaminoborane (PAB). The major absorption bands in the spectrum of partially spent AB (after desorbing the first mole of hydrogen) matches that of PAB reported earlier.[10] Broad bands centered around 1168, 2300 and 3270 cm^{-1} are assigned to B-N, B-H and N-H bond stretching of PAB, respectively. DFT

calculated IR spectra of different molecular oligomers in Figure 4.10, are consistent with the bands assignment.

More detailed examination of Figure 4.9 reveals that a new band at 1562 cm^{-1} grows in for preheated samples and its intensity becomes strong with respect to the band at 1605 cm^{-1}as the preheating period increases. We assign the latter band to N-H bond bending of AB, and the former to N-H bond bending of the -NH_2- group of oligomers or polymers of aminoborane, based on comparison of calculated spectra of AB and possible oligomers shown in Figure 4.10. As mentioned above, the polymeric species is most likely absent if the preheated period is short, e.g., less than 3 hours. To confirm this point, we suspended preheated samples in water because the polymeric species is insoluble in water, and then dried them at room temperature. The spectrum of water-treated, preheated samples is also presented in Figure 4.9. A notable observation is that the band at 1562 cm^{-1} vanishes for the sample preheated for 3 hours with the water treatment. For the same sample, however, two new bands at 1458 and 1726 cm^{-1} appear that are assigned to H-O-H and the B-O vibration of borate hydrates, respectively. Figure 4.9 also reveals that water treatment has no significant effect on the spectrum of the sample with presentment period of 4 hours, consistent with polymers being present and inert with respect to water. Of course, we may not rule out that there are some oligomers in this sample that also do not react with water. However, according to the FTIR results with the water treatment, only oligomeric species occur in the samples with a presentment period of 3 hours, and they react with water to form borate hydrates; further, among the possible oligomers, only hydrolysis of the dimer of aminoborane causes the disappearance of -NH_2- group. Moreover, because the cyclic dimer is reported to be unstable,[6] we believe that linear dimers of aminoborane (LDAB,

$NH_3BH_2NH_2BH_3$) are the predominant oligomers if the preheated period is less than 3 hours at 80 °C.

Table 4.1 Hydrolysis properties and N-H deformation of ammonia borane and its derivatives.

		NH_2,NH_3 symmetric deformation (cm^{-1})	
	Hydrolysis in water	Experimental	Calculated [this work]
Amonia borane (NH_3BH_3)	No[11]	1600 [12]	1728
Diammoniate of diborane ($[NH_3BH_2NH_3]^+[BH_4]^-$)	Readily[11]	1610 [13]	1702,1721
Aminoborane (NH_2=BH_2)		1620 [13]	
Cyclodiborazanes($(BH_2NH_2)_2$)	No[14]	1567,1585,1605[14]	
Cyclotriborazane ($(BH_2NH_2)_3$)	No[14]		
Cyclotetraborazane ($(BH_2NH_2)_4$)	No[14]	1558,1587 [14]	
Poly(aminoboarne) ($(BH_2NH_2)_x$)	No[15]	1560,1600 [15]	
Linear dimer of ammonia borane ($NH_3BH_2NH_2BH_3$)			1664,1706
Linear trimer of ammonia borane ($NH_3(BH_2NH_2)_2BH_3$)			1667,1708

Table 4.1 lists possible species in preheated AB (< 3 h at 80 °C). As shown in the table, either cycloborazanes or poly(aminoborane) will not react with water, ruling out these two types of species as the predominant one in the preheated sample based on FTIR-ATR spectra (Figure 4.9). Additionally, aminoborane is readily polymerized at ambient conditions.[16] Also, the favorable dehydrogenation kinetic for pretreated AB over pristine AB indicates that DADB is the not main species. Therefore, the only possible species left are linear oligomers. Based on DFT calculated spectra, the band at 1562 cm^{-1} is assigned to the deformation of N-H in the B-NH_2-B group and the band at 1602cm^{-1} to deformation of N-H in the B-NH_3 group.

The calculated bond length of N-BH_3 shows that linear dimer of ammonia borane is more active than that linear trimer of ammonia borane in regard to hydrolysis (Table 4.2). Besides, hydrolysis of linear dimer causes disappearance of 1562 cm^{-1} band but hydrolysis of linear trimer does not. It is also to be noted the band length becomes shorter as the chain of the oligomers increases, resulting in longer oligomers less reactive. This finding is consistent with the fact that polyaminoborane does not react with water.

Table 4.2 Calculated bond distance of B-N with BH_3 terminal groups in linear dimers

Ammonia borane and linear oligomers	Calculated N-BH3 bonding length (Å)
NH_3-BH_3	1.6699
$NH_3BH_2NH_2$-BH_3	1.6750
$NH_3BH_2NH_2BH_2NH_2$-BH_3	1.6622
$NH_3BH_2NH_2BH_2NH_2BH_2NH_2$-$BH_3$	1.6564

Hence, it may indicate that the reaction between DADB and AB to produce hydrogen is not important at the early stage of hydrogen release from solid AB. Possible reactions for the formation of LDAB and its hydrolysis are provided in eq 1 and eq 2, respectively, shown below.

$$2NH_3BH_3\ (Mobile\,Phase) = NH_3BH_2NH_2BH_3 + H_2 \qquad (1a)$$

$$\left[(NH_3)_2BH_2\right]^+\left[BH_4\right]^- = NH_3BH_2NH_2BH_3 + H_2 \qquad (1b)$$

$$NH_3BH_2NH_2BH_3 + H_2O = \left[(NH_3)_2BH_2\right]^+\left[BO_2\right]^- + 3H_2 \qquad (2)$$

Eq (1a) and (1b) accounts for the formation of LDAB accompanied by hydrogen release, consistent with the fact that the pressure continuously increases upon maintaining pristine AB at 80 °C for 20 minutes (Figure 4.2). NMR spectroscopic studies have shown that a mobile phase forms at the very early stage during the thermolysis of solid AB.[6] This observation leads us to suggest that LDAB forms from the mobile AB based on the observation of hydrogen release during the pre-treatment. Besides, there is a possibility of forming LDAB via the dehydrogenation of DADB.

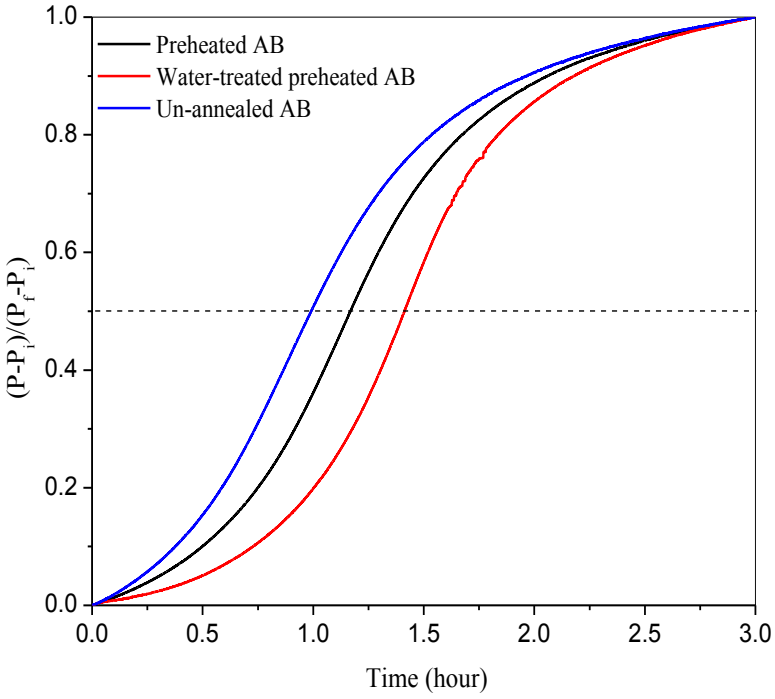

Figure 4.11 Effect of thermal history and water-treatment on dehydrogenation kinetic at 85 °C: P_i is the pressure at the beginning of isothermal stage; P_f is on at the end of isothermal stage.

There are two additional effects resulting from the oligomerization: First, defects occur in AB crystals, which may promote thermal decomposition. As figure 4.11 shows, water-treatment lengthens the half time; however, the decomposition kinetics of pretreated AB, which has been subjected to water-treatment, is still favorable compared with that for pristine AB. Furthermore, the half time of un-annealed AB (which refers to directly heating the sample to 85 °C to carry out thermal decomposition after maintaining pristine AB at 80 °C for 3 hours) is shorter than that of pretreated AB (which was subjected to a cooling step and storage period after maintaining pristine AB at 80 °C for 3 hours). The influence of water-treatment and thermal history on the dehydrogenation is interpreted as the result of minimizing the number of defects accompanying water-treatment and annealing. However, defects do not play a vital role in accelerating the dehydrogenation kinetics because water-treatment, which could eliminate defects, does not dramatically decrease the half-time (Figure 4.11). Second, oligomers form a solid solution with AB, shifting the melting temperature of AB to a lower value. This shift becomes more pronounced as the concentration of oligomers increases. Therefore, for preheated samples, the melting event occurs closer to the decomposition temperature as the preheating period become longer. It is expected that oligomerization and polymerization propagate rapidly via successive addition of AB molecules from the mobile phase to oligomeric and polymeric species, because low energy is required for these processes compared with those in solid state.

From thermal analyses, hydrogen release measurements, and IR spectroscopic data, we deduce that LDAB forms in thermal pretreated samples, and then it reacts with AB to liberate hydrogen. Also, we deduce that formation of oligomers or polymers disrupt the hydrogen-bonding network, resulting in defect formation in AB crystals. Such defects may also act as reactive sites for the dehydrogenation; however, they are not the predominant factor of

controlling hydrogen release. Oligomers or polymers, or their mixture form a solid solution with AB, thereby lowering the melting temperature of AB below the normal melting point. All these factors likely result in a sigmoidal dehydrogenation pattern as shown in this work and previous studies.[5a]

4.5 Conclusions

Thermal treatment of solid AB at 80 °C not only reduces the induction period for hydrogen release but also accelerates the rate hydrogen release at 85 °C. Although the dehydrogenation kinetics becomes more favorable as the preheating period increases, the hydrogen storage capacity of preheated AB slightly decreases at the same time because of hydrogen evolution during the thermal treatment. Our results also show that thermal treatment is comparable to chemical doping with respect to the release rate of the first mole of hydrogen. However, the former approach only affects the first step of dehydrogenation compared with the latter one, which affects the first two dehydrogenation steps.

New species including oligomers and polymers of aminoborane form during thermal pretreatment. Only linear dimers of aminoborane form for preheatment periods less than 3 hours, whereas other oligomers or polymers form for longer thermal pretreatment durations. The oligomerization or polymerization not only disrupts the hydrogen-bonding network to generate defects but also results in the formation of a solid solution. More effort is required to understand the formation of LDAB and its reaction with AB in the initial stage of thermal decomposition; we will example this issue in more detail in continuing work on the thermal pretreatment approach in promoting hydrogen generation from AB.

References

1. (a) Hu, M. G.; Geanangel, R. A.; Wendlandt, W. W., THERMAL-DECOMPOSITION OF AMMONIA-BORANE. *Thermochimica Acta* **1978,** *23* (2), 249-255; (b) Wolf, G.; Baumann, J.; Baitalow, F.; Hoffmann, F. P., Calorimetric process monitoring of thermal decomposition of B-N-H compounds. *Thermochimica Acta* **2000,** *343* (1), 19-25; (c) Baitalow, F.; Baumann, J.; Wolf, G.; Jaenicke-Roszler, K.; Leitner, G., Thermal decomposition of B-N-H compounds investigated by using combined thermoanalytical methods. *Thermochimica Acta* **2002,** *391* (1), 159-168.

2. Gutowska, A.; Li, L.; Shin, Y.; Wang, C. M.; Li, X. S.; Linehan, J. C.; Smith, R. S.; Kay, B. D.; Schmid, B.; Shaw, W.; Gutowski, M.; Autrey, T., Nanoscaffold mediates hydrogen release and the reactivity of ammonia borane. *Angew Chem Int Ed Engl* **2005,** *44* (23), 3578-82.

3. (a) Kim, H.; Karkamkar, A.; Autrey, T.; Chupas, P.; Proffen, T., Determination of structure and phase transition of light element nanocomposites in mesoporous silica: case study of NH3BH3 in MCM-41. *J Am Chem Soc* **2009,** *131* (38), 13749-55; (b) Paolone, A.; Palumbo, O.; Rispoli, P.; Cantelli, R.; Autrey, T.; Karkamkar, A., Absence of the Structural Phase Transition in Ammonia Borane Dispersed in Mesoporous Silica: Evidence of Novel Thermodynamic Properties. *Journal of Physical Chemistry C* **2009,** *113* (24), 10319-10321; (c) Sepehri, S.; Feaver, A.; Shaw, W. J.; Howard, C. J.; Zhang, Q.; Autrey, T.; Cao, G., Spectroscopic studies of dehydrogenation of ammonia borane in carbon cryogel. *J Phys Chem B* **2007,** *111* (51), 14285-9; (d) Feaver, A.; Sepehri, S.; Shamberger, P.; Stowe, A.; Autrey, T.; Cao, G., Coherent carbon cryogel-ammonia borane nanocomposites for H2 storage. *J Phys Chem B* **2007,** *111* (26), 7469-72; (e) Sepehri, S.; Garcia, B. B.; Cao, G. Z., Influence of Surface Chemistry on Dehydrogenation in Carbon Cryogel Ammonia Borane Nanocomposites. *European Journal of Inorganic Chemistry* **2009,** (5), 599-603; (f) Li, L.; Yao, X.; Sun, C. H.; Du, A. J.; Cheng, L. N.; Zhu, Z. H.; Yu, C. Z.; Zou, J.; Smith, S. C.; Wang, P.; Cheng, H. M.; Frost, R. L.; Lu, G. Q. M., Lithium-Catalyzed Dehydrogenation of Ammonia Borane within Mesoporous Carbon Framework for Chemical Hydrogen Storage. *Advanced Functional Materials* **2009,** *19* (2), 265-271; (g) Li, Z.; Zhu, G.; Lu, G.; Qiu, S.; Yao, X., Ammonia borane confined by a metal-organic framework for chemical hydrogen storage: enhancing kinetics and eliminating ammonia. *J Am Chem Soc* **2010,** *132* (5), 1490-1.

4. (a) Denney, M. C.; Pons, V.; Hebden, T. J.; Heinekey, D. M.; Goldberg, K. I., Efficient catalysis of ammonia borane dehydrogenation. *J Am Chem Soc* **2006,** *128* (37), 12048-9; (b) Keaton, R. J.; Blacquiere, J. M.; Baker, R. T., Base metal catalyzed dehydrogenation of ammonia-borane for chemical hydrogen storage. *J Am Chem Soc* **2007,** *129* (7), 1844-+.

5. (a) Heldebrant, D. J.; Karkamkar, A.; Hess, N. J.; Bowden, M.; Rassat, S.; Zheng, F.; Rappe, K.; Autrey, T., The Effects of Chemical Additives on the Induction Phase in Solid-State

Thermal Decomposition of Ammonia Borane. *Chemistry of Materials* **2008,** *20* (16), 5332-5336; (b) Bluhm, M. E.; Bradley, M. G.; Butterick, R., 3rd; Kusari, U.; Sneddon, L. G., Amineborane-based chemical hydrogen storage: enhanced ammonia borane dehydrogenation in ionic liquids. *J Am Chem Soc* **2006,** *128* (24), 7748-9.

6. Himmelberger, D. W.; Alden, L. R.; Bluhm, M. E.; Sneddon, L. G., Ammonia Borane Hydrogen Release in Ionic Liquids. *Inorg Chem* **2009,** *48* (20), 9883-9889.

7. Stowe, A. C.; Shaw, W. J.; Linehan, J. C.; Schmid, B.; Autrey, T., In situ solid state 11B MAS-NMR studies of the thermal decomposition of ammonia borane: mechanistic studies of the hydrogen release pathways from a solid state hydrogen storage material. *Phys Chem Chem Phys* **2007,** *9* (15), 1831-6.

8. Li, J.; Kathmann, S. M.; Hu, H. S.; Schenter, G. K.; Autrey, T.; Gutowski, M., Theoretical investigations on the formation and dehydrogenation reaction pathways of H(NH2BH2)(n)H (n = 1-4) oligomers: importance of dihydrogen interactions. *Inorg Chem* **2010,** *49* (17), 7710-20.

9. Stephens, P. J.; Devlin, F. J.; Chabalowski, C. F.; Frisch, M. J., Ab Initio Calculation of Vibrational Absorption and Circular Dichroism Spectra Using Density Functional Force Fields. *The Journal of Physical Chemistry* **1994,** *98* (45), 11623-11627.

10. Kim, D.-P.; Moon, K.-T.; Kho, J.-G.; Economy, J.; Gervais, C.; Babonneau, F., Synthesis and characterization of poly(aminoborane) as a new boron nitride precursor. *Polymers for Advanced Technologies* **1999,** *10* (12), 702-712.

11. Shore, S. G.; Parry, R. W., CHEMICAL EVIDENCE FOR THE STRUCTURE OF THE DIAMMONIATE OF DIBORANE .2. THE PREPARATION OF AMMONIA-BORANE. *J Am Chem Soc* **1958,** *80* (1), 8-12.

12. Xie, S. T.; Song, Y.; Liu, Z. X., In situ high-pressure study of ammonia borane by Raman and IR spectroscopy. *Canadian Journal of Chemistry-Revue Canadienne De Chimie* **2009,** *87* (9), 1235-1247.

13. Carpenter, J. D.; Ault, B. S., Infrared matrix isolation characterization of aminoborane and related compounds. *The Journal of Physical Chemistry* **1991,** *95* (9), 3502-3506.

14. Böddeker, K. W.; Shore, S. G.; Bunting, R. K., Boron-Nitrogen Chemistry. I. Syntheses and Properties of New Cycloborazanes, (BH2NH2)n1,2. *J Am Chem Soc* **1966,** *88* (19), 4396-4401.

15. Komm, R.; Geanangel, R. A.; Liepins, R., Synthesis and studies of poly(aminoborane), (H2NBH2)x. *Inorg Chem* **1983,** *22* (11), 1684-1686.

16. McGee, H. A.; Kwon, C. T., Cryochemical preparation of monomeric aminoborane. *Inorg Chem* **1970,** *9* (11), 2458-2461.

Chapter Five: Hydrogen Release from Ammonia-borane/MSN Nanocomposites

5.1 Introduction

In order to utilization of AB as an on-board hydrogen storage medium, many approaches have been proposed to accelerate the rate of low-temperature hydrogen release and to reduce the yield of borazane, which includes catalyzing the dehydrogenation over transition metals[1], dispersing AB in ionic liquids[2], and forming composites of AB with mesoporous materials like SBA-15[3], MCM-41[4], carbon cryogel (CC)[5], carbon frameworks[6], and metal organic frameworks (MOFs)[7]. Although the dehydrogenation kinetics of AB nanocomposites is favorable at temperatures < 85 ºC, e.g., the release of the first equivalent of hydrogen is relative fast compared with pristine AB, such composites release less than 3.5 wt.% of hydrogen since the weight of mesoporous materials, usually about half of nanocomposites, must be included (whereas pristine AB upon releasing 1 mole of hydrogen yields 6.5 wt.% hydrogen).[3, 5b] Thus, even without considering the weight of tanks, feed lines, temperature, and pressure control equipment, etc. (which will further decrease the hydrogen storage capacity of the total system by another factor), nanocomposites would not be able to achieve the current U.S. Department of Energy (DOE) 2010 system target of 4.5 wt.%.

Ultimately, to meet the above target for on-board applications, it would be advantageous to tune the composition of AB nanocomposites. Nonetheless, it is unclear how the AB loading level, also known the mass ratio of AB to matrix, affects the dehydrogenation of AB nanocomposites. Clearly, detailed information on the effect of composition is essential in designing novel AB nanocomposites for on-board hydrogen storage. In this report, we discuss the dehydrogenation of MCM-41/AB nanocomposites at specific loading levels. We find for the

loading level range 0.11 to 2.36, which as the loading level decreases the dehydrogenation maximum shifts to lower values. Also, at a loading level lower than 0.15, only one dehydrogenation step is observed at temperatures below 200 °C. Additionally, we investigated the structural state of nanoconfined AB (i.e., AB residing inside mesoporous channels) or adsorbed outside the mesoporous channels). We found that the former to be amorphous while the latter has a tetragonal structure. Moreover, the first dehydrogenation peak for adsorbed AB was found to be lower than that for pristine AB.

5.2 Experiments

5.2.1 MCM-41 synthesis and properties

The MCM-41 nanospheres were used in this research. A brief synthesis procedure is as follows: two grams of cetyltrimethylammonium bromide (CTAB, 99 +%, Alfa-Aesar) was dissolved in 960 mL of water; 12 mL of 1 M NaOH (98.7%, J.T.Baker) solution was then added. The solution was heated to 80ºC with constant stirring. A mixture of 13 mL of tetraethoxysilane (98%, Acros) and 14 mL of ethanol (HPLC Grade, Sigma-Aldrich) was added to the previous solution once the temperature stabilized; the mixture was maintained under the above conditions for 2 hours. The white precipitated was then cooled in air, filtered, washed 3 times with methanol, dried in air, and finally calcined at ~540 ºC for 3 hours to remove any residual CTAB.

The MCM-41 nanospheres were characterized by N_2-adsorption and TEM. The specific surface area found is 726 m^2 g^{-1} and the average channel diameter is 3.45 nm, based on the BJH method. The pore volume found is 0.72 mL g^{-1}, and the average diameter of the nanopsheres is around 200 nm.

5.2.2 Preparation of nanocomposite AB

Table 5.1 The composition of AB-MSN nanocomposites and the stepwise weight loss

AB Loading level	Total Weight loss /%		Weight Loss % Versus AB	
w_{AB}/w_{MCM-41}	1st step	2nd step	1st step	2nd step
0.11	1.10	N/A	11.17	N/A
0.15	1.71	N/A	13.05	N/A
0.21	1.29	4.45	7.51	25.90
0.35	1.50	3.06	5.83	11.88
0.50	2.20	4.66	6.60	13.99
1.00	5.10	9.63	10.22	19.30
2.03	9.70	23.70	14.48	35.38
2.36	7.70	25.50	10.99	36.38
Neat AB	19.93	49.93	19.93	49.93

Two hundred milligrams of AB (97%, Sigma-Aldrich) was dissolved in 10 mL of methanol (99.9%, Pharmco-AAPER). The methanolic solutions were added to appropriate amounts of MCM-41 in a 10-mL vial. The variation of mass ratios of AB to MCM-41 was achieved by changing the amount of methanolic solutions, and adding methanol, if necessary, to obtain a total liquid volume of 5 mL. The suspension in a sealed vial was kept overnight, then dried in a vacuum oven at room temperature for more than 8 hours to remove residual methanol.

The compositions of AB/MSN prepared are listed in table 5.1. The uncertainty of the AB loading levels is estimated to be ± 5 %.

5.3 Characterization

5.3.1 TGA-DSC analysis

A combined TGA-DSC (Q600) technique from TA was employed to detect the weight loss and heat flow, simultaneously, during the dehydrogenation. After loading pristine AB (~ 2 mg) or nanocomposite AB (8-13 mg) to the sample crucible, the sample and empty reference crucibles were heated from room temperature to 37 ºC at the rate of 1 ºC min^{-1}, and then they were kept at this temperature for 2 hours. Finally, the crucibles were heated to 247 at 5 ºC min^{-1}. All experiments were performed under a nitrogen flow of 100 mL min^{-1}.

5.3.2 H_2 release measurements

Hydrogen release was carried out on a HP Micro-DSC from Setaram. Typically, 35 mg of the 0.15 nanocomposite was loaded into the sample cell, and the reference cell was kept empty. The cells were heated from 25 to 90 ºC at 1 ºC min^{-1}, followed by maintaining this temperature for 2 hours. Finally, the cells were cooled to 25 ºC at 3 ºC min^{-1}. The time, temperature, heat flow, and pressure were recorded via the SETSOFT interface every 2 seconds. After the dehydrogenation was complete, 4.0 mL of ethane, at ambient conditions, was injected into the sample cell. The sample cell was held overnight to allow diffusion of various gas species, and then 5 mL of gas sample was withdrawn from the sample cell. It was bubbled through concentrated sulfuric acid in a sealed 10 mL vial that was manually vacuumed using a 10 mL syringe. The gas composition was analyzed using an HP 5890 SII GC equipped with a

MolSieve 5A Plot capillary column (30m×0.53mm, Sigma-Aldrich). The carrier gas was argon and its flow rate was set to 3.74 mL min^{-1}. The column temperature was maintained at 35 ºC for 4 minutes, and then it was programmed to 255 ºC at 10 ºC min^{-1}. The uncertainty in moles of hydrogen released was estimated to be within 8 % based on triplicate measurements.

5.3.3 Wide-angle XRD analysis

Wide angle X-ray powder diffraction (XRD) measurements were performed using a PANalytic X-ray diffractometer in a 2θ range from 10° to 80°, at a step size of 0.05°; graphite monochromatic Cu-Kα radiation with a nickel filter was used.

5.3.4 Micro-Raman analysis

Raman spectra were obtained using an HR800 Horiba Jobin Yvon Raman Microprobe. Samples were placed on a cover glass and excited with 632.8 nm HeNe laser radiation; an x100 object lens was used. The spectrum was recorded from 100 to 3500 cm^{-1}.

5.4 Results and discussion

We observed by thermogravimetric (TG) investigations, for nanocomposites with loading levels above 0.15, two principal peaks (Figure 5.1), attributable to two consecutive dehydrogenation steps, at temperatures below 200 ºC-the peak temperatures correspond to the local maxima in the relative rate of weight loss. Additionally, it is noted that there exists a single resolved temperature peak with a shoulder at ca. 120 ºC for the 0.15 nanocomposite (herein the number references the mass ratio of AB to MCM-41). And, a single peak for the 0.11

nanocomposite without any shoulders is observed below 157 ºC; this temperature matches that at which the second dehydrogenation rate of pristine AB maximizes. A further examination of TG data reveals that for the 2.36 and 2.03 nanocomposites another shoulder exists for temperatures below 110 ºC (inset in Figure 5.1). This latter shoulder is due to the presence of aggregated AB, which coexists with nanoconfined AB (Figure 5.2). The coexistence of the two types of AB may also be inferred from the pore volume of MCM-41 and the density of AB. The measured pore volume of our mesoporous matrix is 0.72 mL g^{-1}; the maximum amount of AB that can be confined in mesopores is 0.56 g AB/g MCM-41, assuming that the density of nanoconfined AB is equal to that of pristine AB (0.78 g mL^{-1}). Consequently, excess AB is present and would not reside inside mesopores with loading levels above 0.56. As a further point, it is to be noted that the first peak temperature for the 2.36 and 2.03 nanocomposites is slightly lower than that for pristine AB, while the second dehydrogenation step shows a peak at ca.157 ºC, indicating that the second dehydrogenation step is less affected by the matrix at relative high loading levels.

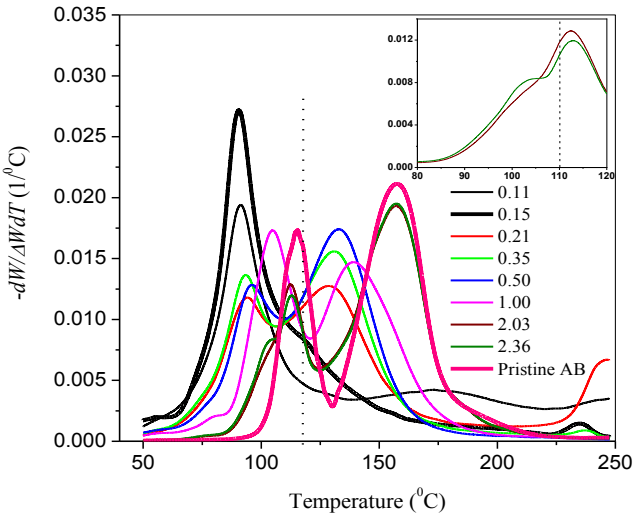

Figure 5.1 Relative weight loss rate of neat AB and nanocomposites with different loading levels. Insert: zoom in graph for the 2.36 and 2.03 nanocomposites; W is the mass difference between 50 and 247 °C.

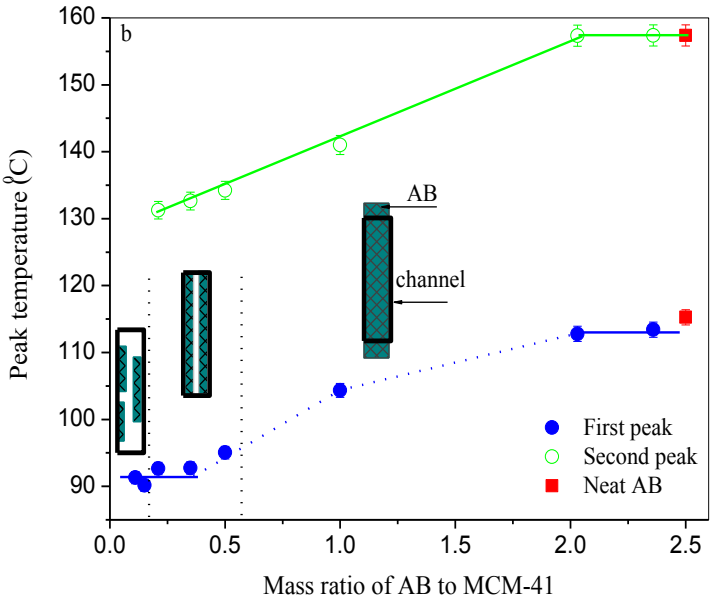

Figure 5.2 Variation of peak temperatures with loading levels.

As mentioned above, the first peak temperature for nanocomposites has a lower value than pristine AB does. And this peak temperature is found to shift even lower, in a monotonic fashion, as the loading level is lowered from 2.03 to 0.35; the shift ceases to a limiting value of 92 °C upon further decrease in the loading level (Figure 5.2); also, the second peak temperature shifts linearly to lower values as the loading level decreases from 2.03 to 0.21 (Figure 5.2).

To gain insight into the low dehydrogenation temperature of nanoconfined AB, we calcualted the apparent activation energy E_a for the first dehydrogenation step. Assuming that the dehydrogenation kinetics of AB residing within the mesoporous channels of MCM-41 and neat AB, the first hydrogen release step can be described by,

$$dx/dt = A\exp(-E_a/RT)(1-x),$$

where x is the conversion of AB, which can be computed from $x = (w_i - w)/(w_i - w_f)$, in which w, w_i and w_f are the weight at time t, onset of dehydrogenation, and the end of dehydrogenation step, respectively. At the first peak temperature, $d^2x/dT^2 = 0$, if a linear heating rate is employed. Therefore,

$$E_a = RT_P^{\,2}\left(dx/dT\right)_{T_P}/\left(1-x_P\right)$$

We found E_a values of 104 and 109 kJ mol^{-1} for the 0.5 and 0.35 nanocomposites, respectively, which is lower than that for pristine AB (151 kJ mol^{-1}). A low E_a has also been reported for nanoconfined AB in other nanocomposites.[3, 5a, 6] The lower E_a is likely due to a size effect. Indeed, for nanosized AB, less energy is required for the formation of an active species like diammoniate of diborane (DADB), which controls hydrogen release.[8] However, our findings cannot exclude the influence of the internal surface of the mesoporous channels on E_a, because nanosized AB is in contact with the internal surface. We interpret our observations as

suggesting that AB is layered on the internal surface of the mesoporous material (Figure 5.2), with thickness of the layered material decreasing with decreased loading levels; this, in turn, results in an increased number of active species, giving rise to a low peak temperature, even though E_a is almost unchanged as the loading level decreases from 0.5 to 0.35. This mechanism would also account for low dehydrogenation temperatures for what we refer to as aggregated AB. In this case, the small size of aggregated AB, inferred from the melting of aggregated AB, results in a large number of active species, a reduced energy barrier for dehydrogenation, or both when compared with pristine AB.

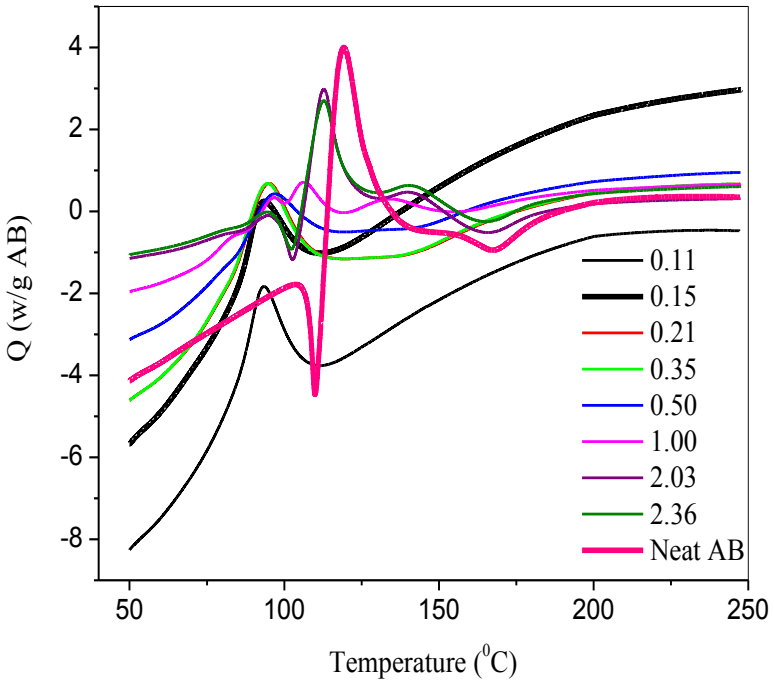

Figure 5.3 Thermographs of neat AB and nanocomposites with different loading levels.

For pristine AB, one endothermic peak is found at ca. 109 °C (Figure 5.3), and is attributable to the melting of AB. Two additional peaks, one exothermic the other endothermic, are observed at temperatures above 110 °C. These latter two maxima correlate with the two consecutive dehydrogenation steps. The second endothermic peak is also confirmed by

thermography of spent AB (i.e., polymeric AB) resulting from release of the first equivalent of hydrogen (Figure 5.4).

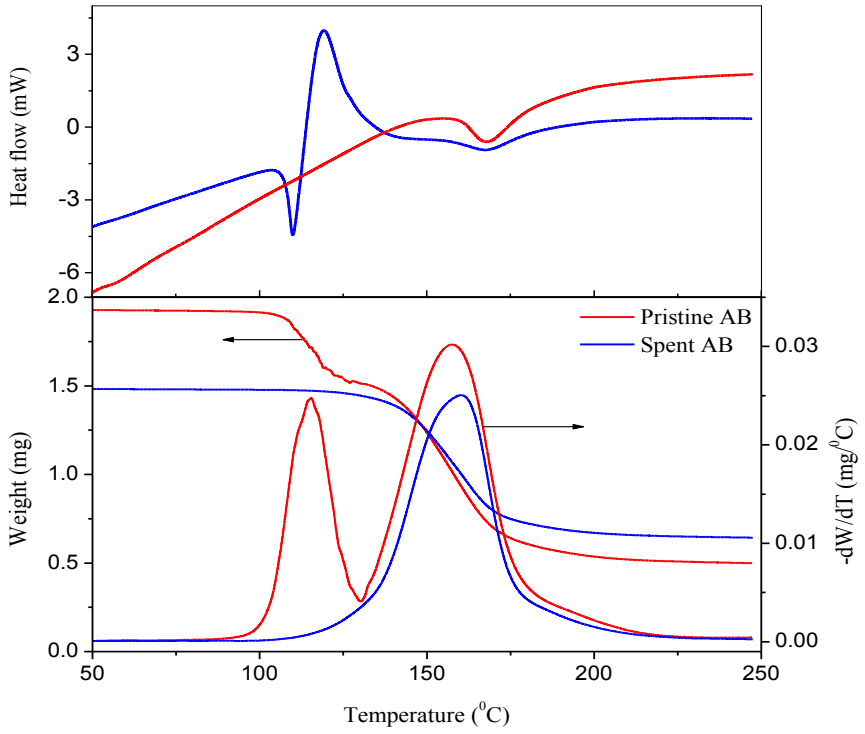

Figure 5.4 Temperature dependence of the weight, heat flow and weight loss rate for dehydrogenation of pristine and spent AB.

For nanocomposites, these peaks shift to lower temperatures and only one exothermic peak is observed at loading levels below 0.5. We observe that the melting event is absent for nanoconfined AB. And based on the melting point of nanosized AB, the relationship between the melting point depression and crystal size is given by

$$\Delta T_m = 814.85/d - 20.92,$$

in which ΔT_m (°C) is the melting point depression and d (nm) is the diameter of particles. The parameters of this equation are estimated from the data reported before by assuming that AB coats as a shell the spherical BN nanoparticles.[9] The size of aggregated AB is estimated to be less than 30 nm.

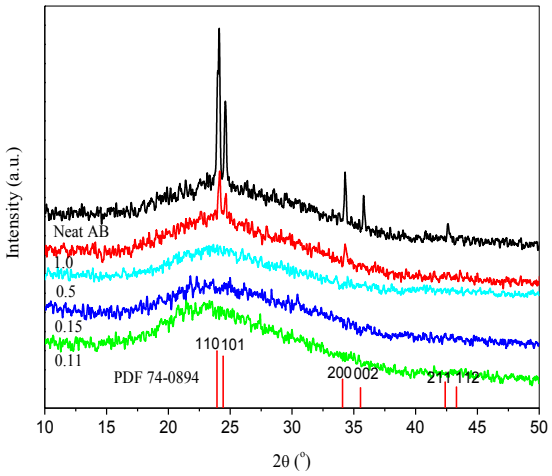

Figure 5.5 XRD patterns of neat AB and nanocomposites with different loading levels. Peaks in neat AB correspond to the PDF file 74-0894 that correspond to tetragonal AB.

Additionally, XRD patterns indicate that nanoconfined AB is amorphous while aggregated AB has a tetragonal structure (Figure 5.5), and the melting temperature of the latter is below 109 °C.

We have observed that the dehydrogenation pathway of the 0.11 and 0.15 nanocomposites is different from that of the others; the second dehydrogenation step of these two nanocomposites becomes undetectable. To obtain more insight into the dehydrogenation behavior of AB nanocomposites at low loading levels, the amount of hydrogen released from the 0.15 nanocomposite at 89.5 °C was measured using a high-pressure differential scanning calorimeter.

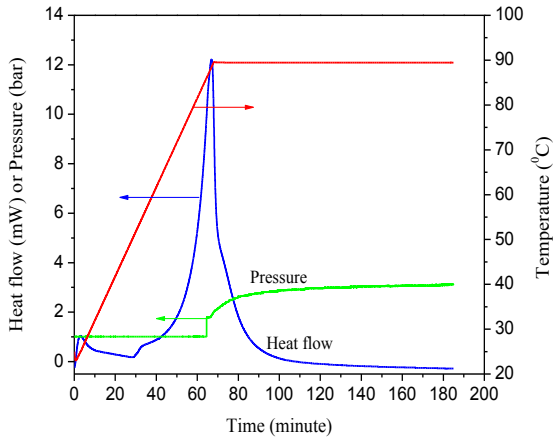

Figure 5.6 Temperature, heat flow, and pressure profiles during dehydrogenation of the 0.15 nanocomposite.

As Figure 5.6 shows, the onset of heat release was detected at 35 minutes, which correlates to the start of dehydrogenation, and the dehydrogenation is complete in 1 hour, after the temperature reaches 89.5 °C, as indicated by no significant change in both heat flow and pressure being observed after 127 minutes. The increase in the pressure is mainly due to hydrogen evolution, because the formation of other volatile products such as borazine is dramatically inhibited by confining AB in mesoporous channels of silica.[3] The yield of hydrogen is 12.6 wt.% with respect to AB, which corresponds to 1.9 mol H_2 per mol AB. This finding provides an approach to enhance the hydrogen storage capacity of AB nanocomposites, e.g., 5.5 wt. % of hydrogen (with respect to the total mass of nanocomposites) can be achieved for matrice with a surface area of 3800 m^2 g^{-1}, along with a favorable hydrogen release rate at temperatures below 85 °C, if the low-temperature release of two equivalents of hydrogen is mainly dependent on the surface area. Such a surface areas is well attainable for some porous materials like carbon[10], coordination polymers[11] and covalent organic frameworks[12].

A potential mechanism behind the low-temperature release of two moles of hydrogen is that the thickness of the AB nanostructured layer is subnanometer, requiring less energy for the second dehydrogenation step. For the 0.15 nanocomposite, the thickness is about 2.5 Å, assuming an AB density of 0.78 g mL^{-1}. Hence, given the molecular size of AB,[4a] only a thickness of one monolayer likely exists on the pore surface (Figure 5.2b). However, the reaction between AB or thermolysis products like polyaminoborane and SiOH groups on the silica surface, which produces hydrogen during the thermolysis, cannot be excluded. Verification of this reaction requires spectroscopic studies of spent AB nanocomposites. Experiments to obtain these data are in progress and will be reported in a subsequent work.

5.5 Conclusions

Thermal analysis show that the dehydrogenation peak temperatures for MCM-41-AB nanocomposites shift to low values as the loading level decreases. Moreover, only one dehydrogenation step is detected for 0.11 and 0.15 nanocomposites at temperatures below 200 ºC. For the 0.15 nanocomposites, 12.6 wt. % of hydrogen, in regard to AB, is liberated in 1 hours at 89.5 ºC. Our results show that AB confined within the mesopores is amorphous, while AB outside of the channels has a tetragonal structure. As mentioned, the first dehydrogenation peak for aggregated AB is lower than that for neat AB. Additionally, we deduce that the coating of AB as very thin layers (possibly even a monolayer covering) within the pores may contribute to the low-temperature release of two equivalents of hydrogen. The present work improves the understanding the nature of mesoporous matrix-AB nanocomposites and provides a strategy for enhancing the hydrogen yield without negatively impacting the kinetics of the dehydrogenation process at low temperatures.

References

1. (a) Blaquiere, N.; Diallo-Garcia, S.; Gorelsky, S. I.; Black, D. A.; Fagnou, K., Ruthenium-catalyzed dehydrogenation of ammonia boranes. *J Am Chem Soc* **2008,** *130* (43), 14034-5; (b) Wright, W. R.; Berkeley, E. R.; Alden, L. R.; Baker, R. T.; Sneddon, L. G., Transition metal catalysed ammonia-borane dehydrogenation in ionic liquids. *Chem Commun (Camb)* **2011,** *47* (11), 3177-9.

2. (a) Bluhm, M. E.; Bradley, M. G.; Butterick, R., 3rd; Kusari, U.; Sneddon, L. G., Amineborane-based chemical hydrogen storage: enhanced ammonia borane dehydrogenation in ionic liquids. *J Am Chem Soc* **2006,** *128* (24), 7748-9; (b) Himmelberger, D. W.; Alden, L. R.; Bluhm, M. E.; Sneddon, L. G., Ammonia Borane Hydrogen Release in Ionic Liquids. *Inorg Chem* **2009,** *48* (20), 9883-9889.

3. Gutowska, A.; Li, L.; Shin, Y.; Wang, C. M.; Li, X. S.; Linehan, J. C.; Smith, R. S.; Kay, B. D.; Schmid, B.; Shaw, W.; Gutowski, M.; Autrey, T., Nanoscaffold mediates hydrogen release and the reactivity of ammonia borane. *Angew Chem Int Ed Engl* **2005,** *44* (23), 3578-82.

4. (a) Kim, H.; Karkamkar, A.; Autrey, T.; Chupas, P.; Proffen, T., Determination of structure and phase transition of light element nanocomposites in mesoporous silica: case study of NH3BH3 in MCM-41. *J Am Chem Soc* **2009,** *131* (38), 13749-55; (b) Paolone, A.; Palumbo, O.; Rispoli, P.; Cantelli, R.; Autrey, T.; Karkamkar, A., Absence of the Structural Phase Transition in Ammonia Borane Dispersed in Mesoporous Silica: Evidence of Novel Thermodynamic Properties. *Journal of Physical Chemistry C* **2009,** *113* (24), 10319-10321.

5. (a) Sepehri, S.; Feaver, A.; Shaw, W. J.; Howard, C. J.; Zhang, Q.; Autrey, T.; Cao, G., Spectroscopic studies of dehydrogenation of ammonia borane in carbon cryogel. *J Phys Chem B* **2007,** *111* (51), 14285-9; (b) Feaver, A.; Sepehri, S.; Shamberger, P.; Stowe, A.; Autrey, T.; Cao, G., Coherent carbon cryogel-ammonia borane nanocomposites for H2 storage. *J Phys Chem B* **2007,** *111* (26), 7469-72; (c) Sepehri, S.; Garcia, B. B.; Cao, G. Z., Tuning dehydrogenation temperature of carbon-ammonia borane nanocomposites. *Journal of Materials Chemistry* **2008,** *18* (34), 4034-4037.

6. Li, L.; Yao, X.; Sun, C. H.; Du, A. J.; Cheng, L. N.; Zhu, Z. H.; Yu, C. Z.; Zou, J.; Smith, S. C.; Wang, P.; Cheng, H. M.; Frost, R. L.; Lu, G. Q. M., Lithium-Catalyzed Dehydrogenation

of Ammonia Borane within Mesoporous Carbon Framework for Chemical Hydrogen Storage. *Advanced Functional Materials* **2009,** *19* (2), 265-271.

7. (a) Li, Z.; Zhu, G.; Lu, G.; Qiu, S.; Yao, X., Ammonia borane confined by a metal-organic framework for chemical hydrogen storage: enhancing kinetics and eliminating ammonia. *J Am Chem Soc* **2010,** *132* (5), 1490-1; (b) Li, Y. Q.; Xie, L.; Li, Y.; Zheng, J.; Li, X. G., Metal-Organic-Framework-Based Catalyst for Highly Efficient H-2 Generation from Aqueous NH3BH3 Solution. *Chemistry-a European Journal* **2009,** *15* (36), 8951-8954.

8. Stowe, A. C.; Shaw, W. J.; Linehan, J. C.; Schmid, B.; Autrey, T., In situ solid state 11B MAS-NMR studies of the thermal decomposition of ammonia borane: mechanistic studies of the hydrogen release pathways from a solid state hydrogen storage material. *Phys Chem Chem Phys* **2007,** *9* (15), 1831-6.

9. Neiner, D.; Karkamkar, A.; Linehan, J. C.; Arey, B.; Autrey, T.; Kauzlarich, S. M., Promotion of Hydrogen Release from Ammonia Borane with Mechanically Activated Hexagonal Boron Nitride. *Journal of Physical Chemistry C* **2009,** *113* (3), 1098-1103.

10. Gaslain, F. O. M.; Parmentier, J.; Valtchev, V. P.; Patarin, J., First zeolite carbon replica with a well resolved X-ray diffraction pattern. *Chem Commun (Camb)* **2006,** (9).

11. Koh, K.; Wong-Foy, A. G.; Matzger, A. J., A Porous Coordination Copolymer with over 5000 m2/g BET Surface Area. *J Am Chem Soc* **2009,** *131* (12), 4184-4185.

12. Furukawa, H.; Yaghi, O. M., Storage of Hydrogen, Methane, and Carbon Dioxide in Highly Porous Covalent Organic Frameworks for Clean Energy Applications. *J Am Chem Soc* **2009,** *131* (25), 8875-8883.

Chapter Six: Hydrogen Release from Ammonia-borane/Mesoporous silica Nanocomposites - the effect of pore size

6.1 Introduction

Ammonina-borane (AB, NH_3BH_3) has a high gravimetric hydrogen density and is nonflamable and nonexplosive under standard conditions, which makes it a good candidate for chemical hydrogen storage.[1] The thermal decomposition of neat AB includes three steps which occur at around 110, 150 and > 500 ^oC respectively, and totally up to 19.6 wt. % hydrogen release in the procedure.[2] Moreover near thermal-neutral thermodynamics in the releasing process make the regeneration and usage of AB more favorable.[3]

Recently a significant number of research efforts are directed toward enhancing the decomposition kinetics, with respect to the releasing of hydrogen at low temperature ca. 85 ^oC and reduce violated product such as ammonia and borazine.[3-4] Many of recently reports are targeting on forming nanocomposites of AB with mesoporous materials, such as SBA-15,[3] MCM-41,[5] carbon cryogel (CC),[6] and carbon framework (CMK).[7] These mesoporous composites materials are found to be reliable media to enhance the decomposition of AB, and in the meantime, reduce the producing of borazine. While besides the improvement in kinetics, the introduction of the mesoporous materials as hosts would largely reduce the total hydrogen capacity in the whole system. So a balance in between the hydrogen capacity and releasing property should be compromised in order to serve best for the requirement in different applications.

Some interesting phenomena have been discovered in former researches on nanoconfined AB, which is AB loaded in mesoporous matrices. Autrey and coworkers, who were the first to

investigate AB mesoporous composites,[3] have discovered that when AB is loaded in the SBA-15 pores, lower H_2 releasing temperature will be achieved with almost no producing of borazine. In a more recently report, they also found that the melting point of AB disappeared when AB is loaded in the MCM-41 mesopores, meanwhile a structure phase transition of AB, that should be at around 225K, is also absented.[8] On the other hand, Feaver et al. found that the first two decomposition steps of AB can be merged into one at around 60 ^oC when AB is loaded in carbon cryogel.[6a] We performed further research on AB/MCM-41 nanocomposites, it is proved that there is also a critical loading level for AB/MCM-41 nanocomposites that the two dehydrogenation steps would merge into one. Our calculated critical loading level is more than 0.13g/g MCM-41 or 0.20mg/m^2 with respect to surface area base on the AB/MCM-41 nanocomposites.[5c] After investigation on wide range of loading levels (AB loaded in MCM-41), it reveals that both AB in the pores (referred as nanocomfined AB) and AB grown out from the pores (referred as aggregated AB), show enhance hydrogen releasing properties.

In this chapter, we extend our research to the ammonina borane/mesoporous silica (AB/MS) (including MCM-41 and SBA-15 mesoporous silica) nanocomposites with various mesopore sizes. The correlation of dehydrogenation temperature with pore size and loading level is investigated. It is found that critical loading levels are different in various mesoporous silica pore sizes, which is believed to be related to surface catalysis reaction. We also discovered that the melting point of AB will disappear only when AB crystal size is smaller than 11 nm. The relation between the mesopore size and AB thermochemical properties at different loading levels are also discussed.

6.2 Experiments

6.2.1 Properties of mesoporous silica

Preparation of MCM-41 sample (M-4) is discussed in chapter 5, and SBA-15 samples with different pore sizes (S-6, S-11, S-14, S-16, S-28) are acquired from Prof. Kruk, College of Staten Island. Detailed preparation and characterization can found in the reference.[9] The pore size, pore volume, and surface area of the mesoporous silica materials are calculated from N_2 adsorption-desorption isotherm results and listed in table 6.1.

Table 6.1 Properties of mesoporous silica materials

Sample	**PD** (nm)	**PV**(cm^3/g)	**ST** (m^2/g)
M-4	3.5	0.72	727
S-6	6.5	0.63	650
S-11	11.1	1.11	530
S-14	14.0	1.36	840
S-16	15.7	1.69	725
S-28	28.2	1.42	290

PD= pore diameter; PV= Pore volume; ST = surface area calculated by BET method

6.2.2 Preparation of ammonia borane/mesoporous silica nanocomposites

The method for preparation of Ammonia borane/mesoporous silica (AB/MS) nanocomposties can be summarized as following: first 200 mg of AB (97%, Sigma-Aldrich) was dissolved into 10 mL of methanol (99.9%, Pharmco-AAPER), then a certain amount of above methanolic solutions was added to an appropriate amount of mesoporous silica in a 25-mL vial. The variation of mass ratios of AB to mesoporous silica was achieved by changing the amount of methanolic solutions but adding more methanol, if necessary, to obtain a total liquid volume of 5 mL. After the suspension in the sealed vial was kept for more than 3 hours, it was dried in a vacuum oven at room temperature for more than 8 hours to remove methanol. AB/MS

nanocomposites are formed and keep in the sealed vial at around 4 ^{o}C before use. The compositions for the various samples are listed in table 6.2.

Table 6.2 Compositions of the AB/MS nanocomposites

Sample	AB/mg	M-4/mg	AB wt%	mgAB/m^2	gAB/mL	% Pore Volume
M4-f	50.5	101.0	33.3	0.69	0.69	88.46
M4-g	101.4	101.3	50.0	1.38	1.39	178.21
M4-a	15.2	100.1	13.1	0.21	0.209	26.79
	AB/mg	**S-6/mg**				
S6-f	4.8	10.1	32.4	0.74	0.76	97.44
S6-g	13.8	7.1	66.1	3.00	3.09	396.15
S6-a	4.6	35.7	11.4	0.20	0.205	26.28
	AB/mg	**S-11/mg**				
S11-f	15	15.1	49.8	1.87	0.89	114.10
S11-g	15	2.8	84.3	10.11	4.83	619.23
S11-a	14.2	81.2	14.9	0.33	0.16	20.51
	AB/mg	**S-14/mg**				
S14-f	7.67	7.8	49.6	1.17	0.72	92.31
S14-g	23.1	5.7	80.2	4.82	2.97	380.77
S14-a	2.5	14.5	14.5	0.20	0.125	16.03
	AB/mg	**S-16/mg**				
S16-f	15	15.1	49.8	1.37	0.59	75.64
S16-g	10	2.2	82.0	6.27	2.69	344.87
S16-a	6.4	49.3	11.5	0.18	0.077	9.87
	AB/mg	**S-28/mg**				
S28-f	20	20	50.0	3.45	0.70	89.74
S28-g	15	2.9	83.8	17.84	3.64	466.67
S28-a	2.13	34	5.9	0.22	0.044	5.64

6.3 Characterization

6.3.1 TGA-DSC analysis

A combined TGA-DSC (Q600) technique from TA was employed to detect the weight loss and heat flow, simultaneously, during the dehydrogenation. After loading pristine AB (~ 2 mg) or nanocomposite AB (8-13 mg) to the sample crucible, the sample and empty reference

crucibles were heated from room temperature to 37 ºC at the rate of 1 ºC min^{-1}, and then they were kept at this temperature for 2 hours. Finally, the crucibles were heated to 247 at 5 ºC min^{-1}. All experiments were performed under a nitrogen flow of 100 mL min^{-1}.

6.3.2 Wide-angle XRD analysis

Wide angle X-ray powder diffraction (XRD) measurements were performed using a PANalytic X-ray diffractometer in a 2θ range from 10° to 80°, at a step size of 0.05°; graphite monochromatic Cu-Kα radiation with a nickel filter was used.

6.3.3 High resolution transition electron microscopy (HRTEM)

High resolution transition electron microscopy (HRTEM) investigation was performed on a JEOL 2100 thermionic (tungsten) transmission electron microscope at accelerating voltage 200 kV. The samples used for TEM observations were prepared by dispersing sample in ethanol followed by ultrasonic vibration for 5 min, then placing a drop of the suspension onto a copper grid coated with a layer of amorphous carbon.

6.3.4 Scanning transmission electron microscopy (STEM)

Low voltage scanning transmission electron microscopy (STEM) was performed on a Zeiss Supra55VP Scanning Electron Microscope, which is a field emission SEM with a maximum resolution of 1 nm. The sample preparation is the same as the HRTEM sample.

6.3.5 N_2 adsorption-desorption measurement

Nitrogen adsorption-desorption measurement was carried out on a Micromeritics ASAP 2020 volumetric adsorption analyzer at -196 °C. Before the adsorption analysis, calcined samples were outgassed under a vacuum at 200 °C in the port of the adsorption analyzer.

6.4 Results and discussion

Based on our previous research on AB/MCM-41 nanocomposites, we know that different loading level of the ammonia borane in the AB/MS nanocomposites will lead to a series of change in hydrogen release properties. Hence we can divide the loading level of AB within mesoporous matrices into three stages from low to high: 1. Adsorption stage, where AB forms nanostructured layers on the surface of the mesopores; 2. Filling Stage, where AB fills in the pore until the pore volume is totally filled up; 3.Growth stage, where AB grow out from the pores forming nanowires or cluster of nanowires with much larger diameter compare to the pore size. Beyond the three stages, extra AB introduced to the system will be independent to the composites, as same as neat AB as respect to the thermal properties. Our discussion is then divided correspondently by the different loading stages.

6.4.1 AB/MS nanocomposites loading at adsorption stage

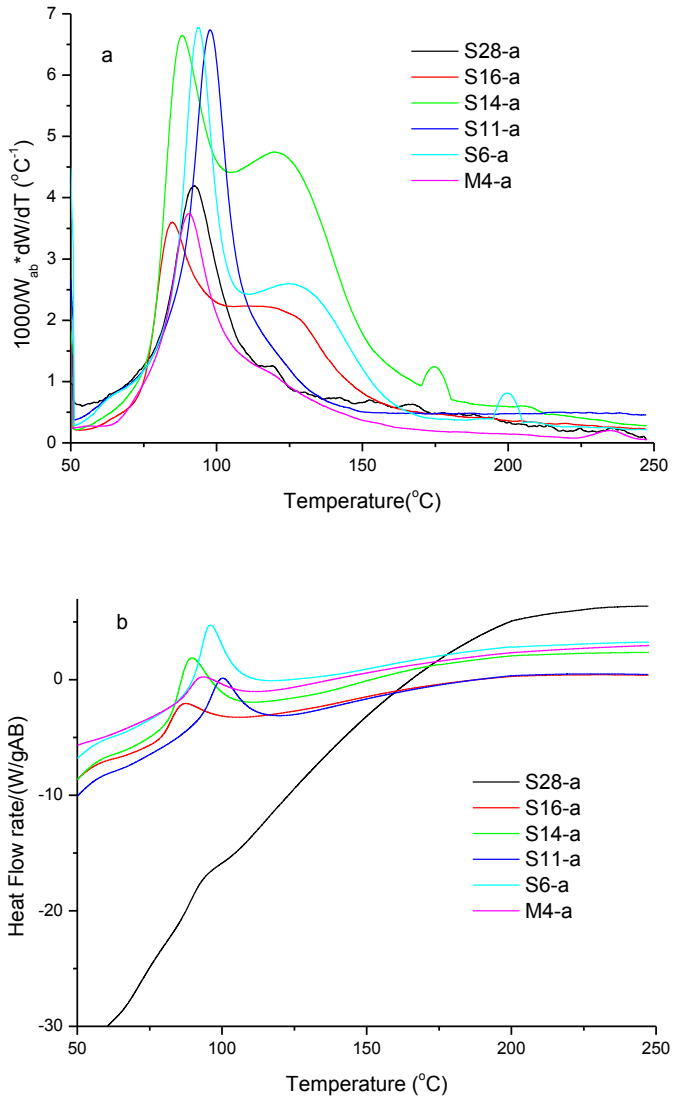

Figure 6.1. TGA graphs (a) and DSC graphs (b) of the AB/MS samples in adsorption stage

Figure 6.1a and b are TGA and DSC plots of the samples that have AB loading level around the adoption stage. The net amount of AB on based on the surface area of mesoporous silica were calculated and listed above in table 6.2

As it can be seen from TGA data in figure 6.1a, the weight loss peak of all samples are shifted to lower than 100 °C. Also the melting point of AB is missing and only one heat flow peak investigated from DSC plots in Figure 6.1b. This indicates no neat AB is occurred in AB/MS nanocomposites and the sample is really loaded to pore and filled to the adsorption stage. Analysis of TGA data shows, M4-a, S11-a, and S28-a samples have only one weight loss peaks, which is due to merging of the first two AB dehydrogenation steps, while sample S-6a, S14-a, and S16-a still show peaks of second dehydrogenation steps. Due to the face that all the sample are loading at around AB 0.20mg/m^2 base on the mesoporous surface area, this indicates, instead of the diameter of pore channel, the pore conditions, like secondary pore distribution, and surface functionalization may contribute more to merge of the first two dehydrogenation steps in AB/MS composition.

6.4.2 AB/MS nanocomposites loading at filling stage

Figure 6.2a and b are TGA and DSC plots of the samples that have AB loading level around the filling stage. Based on TGA graphs of the composites in figure 6.2a, the first and second dehydrogenation peaks are both shifted to lower temperature than neat AB. It is also observed in DSC graphs in figure 6.2b, that the melting point is missing in the sample M4-f and S6-f, which are samples with pore size less than 11 nm. This can own to amorphous phase of AB dominated in the pore smaller than 11 nm. In order to clarify the status of AB, we investigated the all samples loading around filling stage with XRD. Surprisingly, result from the XRD measurements indicates that crystalized AB is presented even in 6 nm pores (as been seen in figure 6.3), which means the melting point can be missing even when AB is crystallized in the pores.

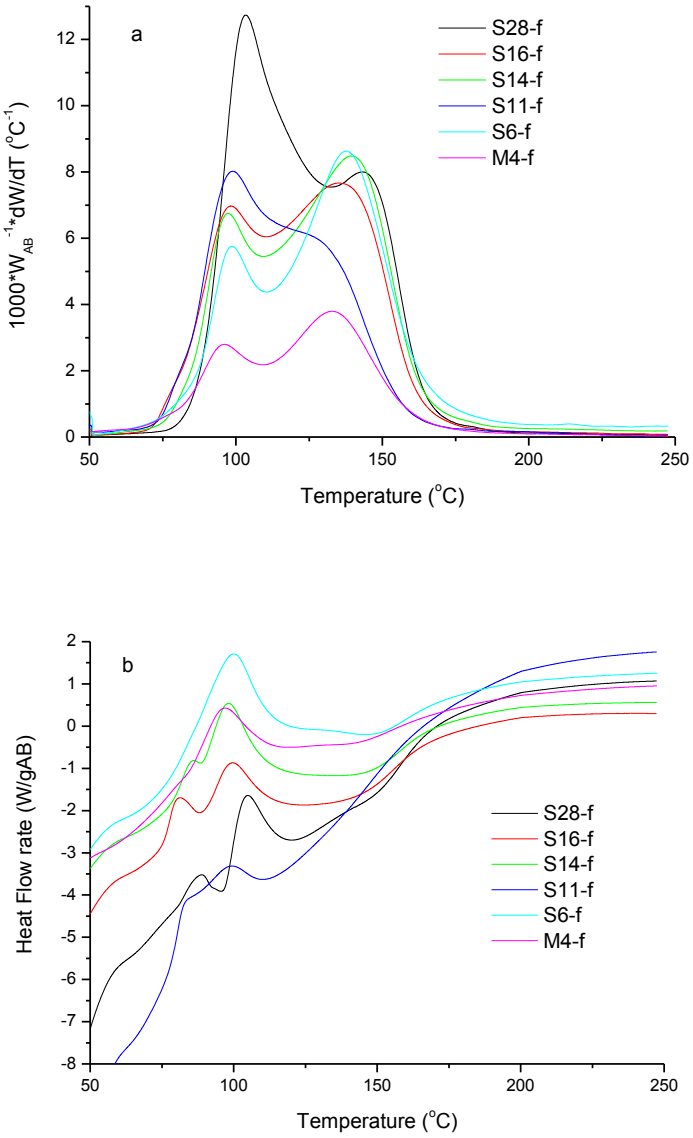

Figure 6.2. TGA graphs (a) and DSC graphs (b) of the AB/MS samples in filling stage

The disappearance of AB melting point are only related to size of the AB crystals, which means the mesopores that the size of AB crystal are the key reason that AB crystal didn't not show melting point in the samples with pore size smaller than 11 nm. Base on the evidence, we rationalize the possible kinetics for MS/AB composites to skip the melting point; it is believed

that when the pore size is less than 11 nm, the first dehydrogenation temperature of AB will drop to below the melting point. This will lead to decomposition of AB before melting.

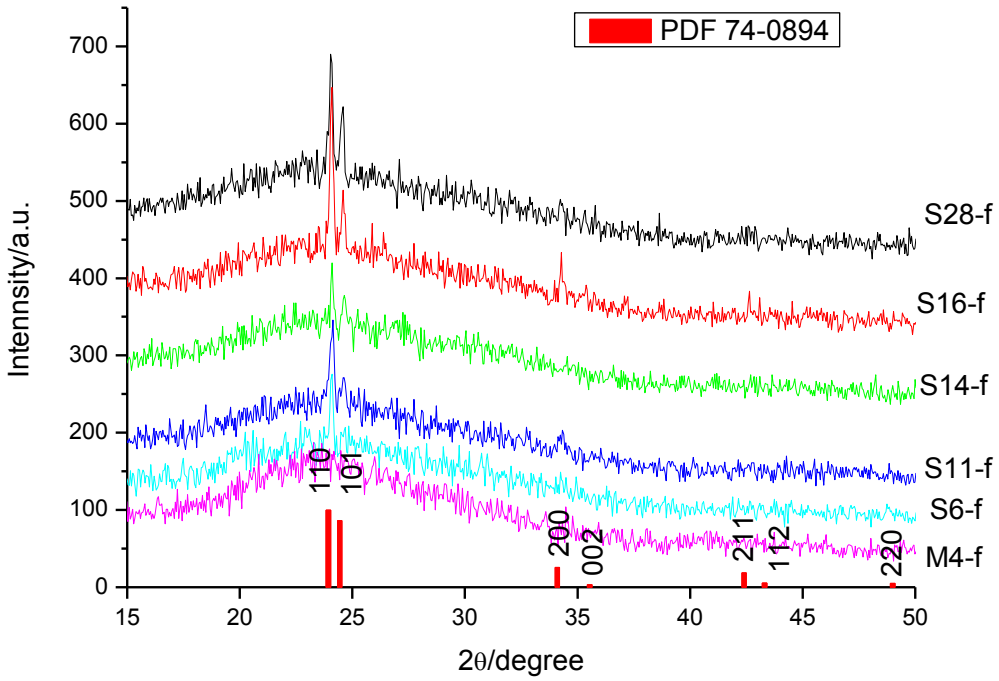

Figure 6.3 XRD patterns of AB/MS nanocomposites at loading level of filling stage

Base on the TGA result, the first and second dehydrogenation peaks of all samples are summarized and plotted versus the pore diameter of mesoporous silica. As figure 6.4, the first dehydrogenation peak is almost independent of the pore diameter up to 16 nm; however the second dehydrogenation peak is decreasing when the pore size is smaller. This can be explained by the forming of nanopatches in the pore. We compare the report by Zhang and co-worker on the forming of Au in the MCM-41 pores; the nanopathces are formed instead of continuous long nanowires. But when the pore diameter is large enough the forming of the nanowire would be

much easier and in this case the longitude axis of the wire will not be active to the dehydrogenation. The first dehydrogenation will induce the expansion of AB, which makes spent AB (i.e. Ployammoina borane) into continuous wire, and consequently the second dehydrogenation peak is dependent on the pore size only.

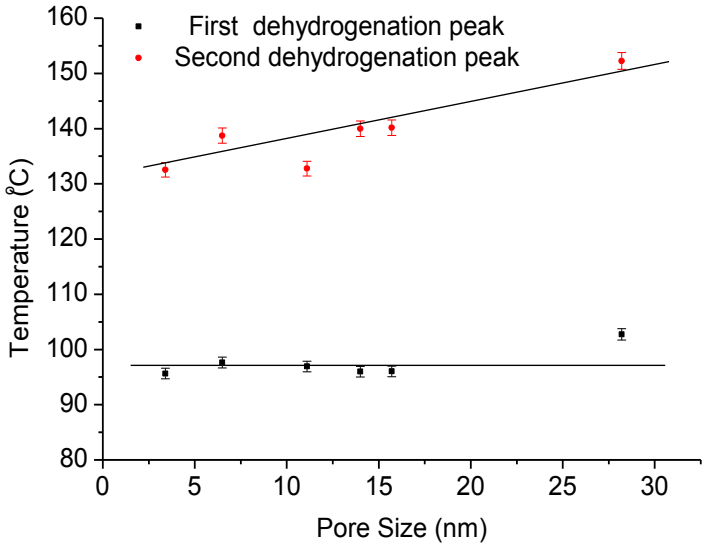

Figure 6.4. Temperature dependence of AB dehydrogenation on pore size in filling stage

6.4.3 Properties of the AB/MS composites at growth stage

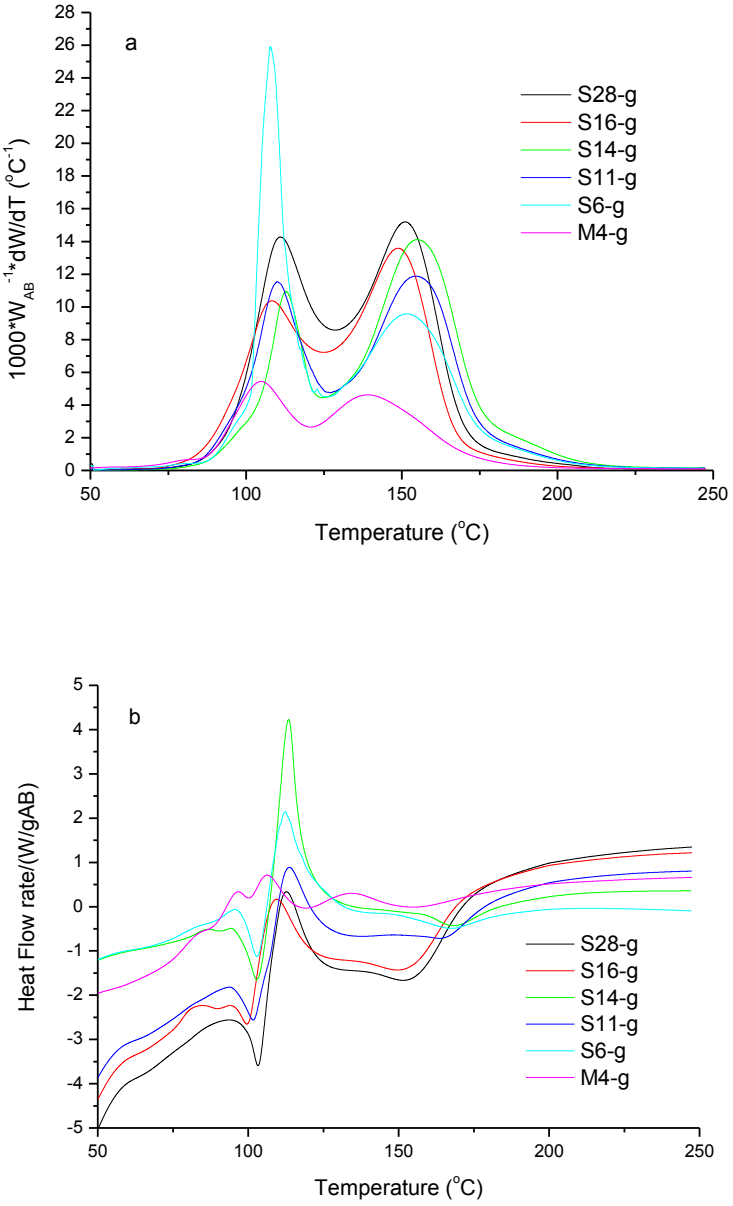

Figure 6.5. TGA graphs (a) and DSC graphs (b) of the AB/MS samples in the growth stage

The growth region is confirmed with the examining of the melting point and decomposition peak shift. When AB is still loaded in the growth region, melting point and

decomposition peak of neat AB is detected. The limit for the growth region is not that clear, due to the lack of research on the mechanism. But there is obvious evidence that as much as 4 times AB than the pore volume of mesoporous materials is able to loaded as the aggregated AB (term that we used to indicate the special condition). Due to the high loading ability, we would go further on this direction to uncover the mechanism and loading limits.

The growth stage samples have AB volume larger than the total pore volume of the mesoporous silica. Based on our theory and investigate, the extra amount of the AB will grow out from the pore, rather than form a separate AB crystal. In order to prove the structure of the MS/AB composites, scanning transmission electron microscope (STEM) measurement s were done with various samples. The results are listed from figure 6.6 to figure 6.11.

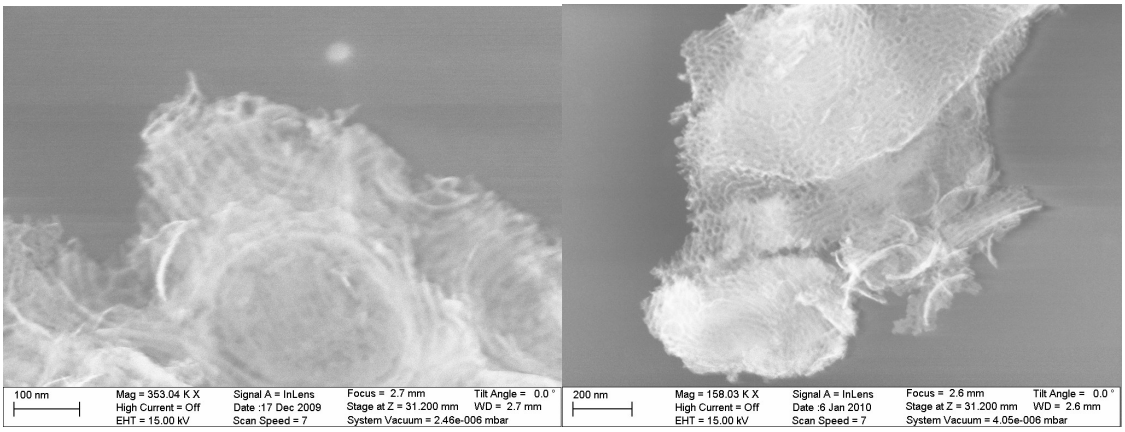

Figure 6.6 STEM images of sample S-28g

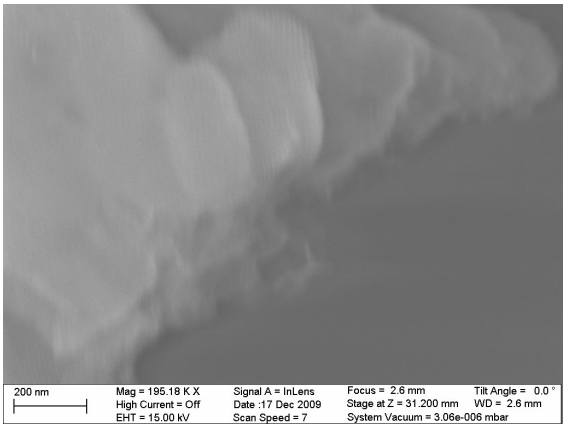

Figure 6.7 STEM image of sample S-16g

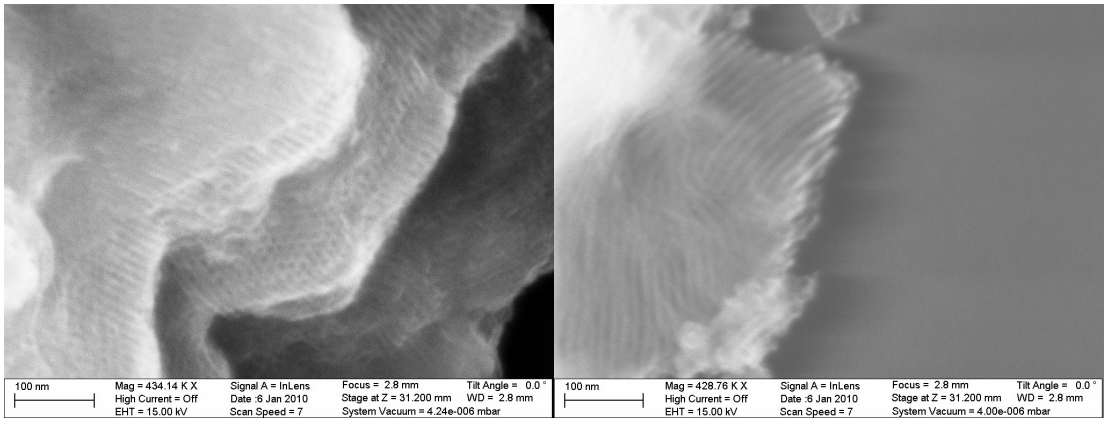

Figure 6.8 STEM images of sample S-14g

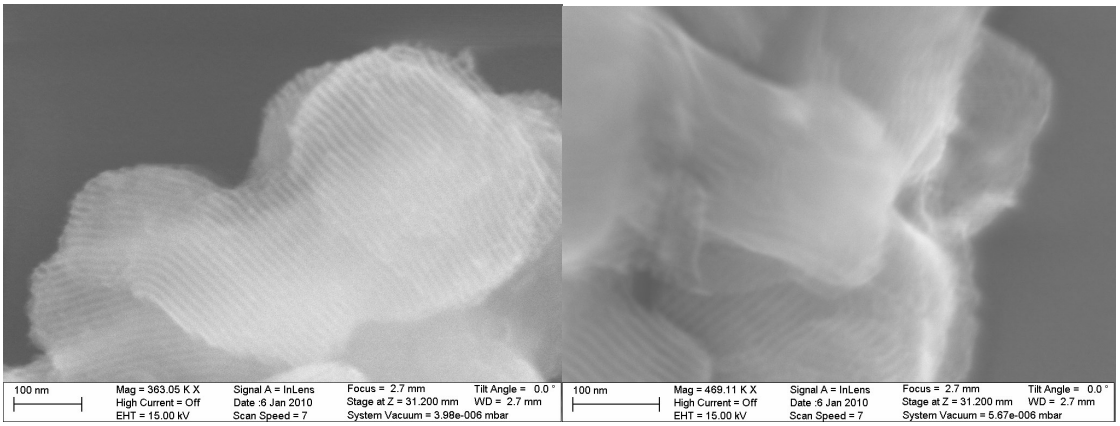

Figure 6.9 STEM images of mesoporous silica sample S-14

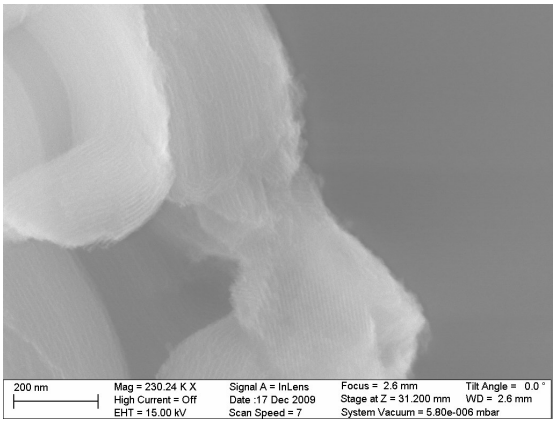

Figure 6.10 STEM images of sample S-11g

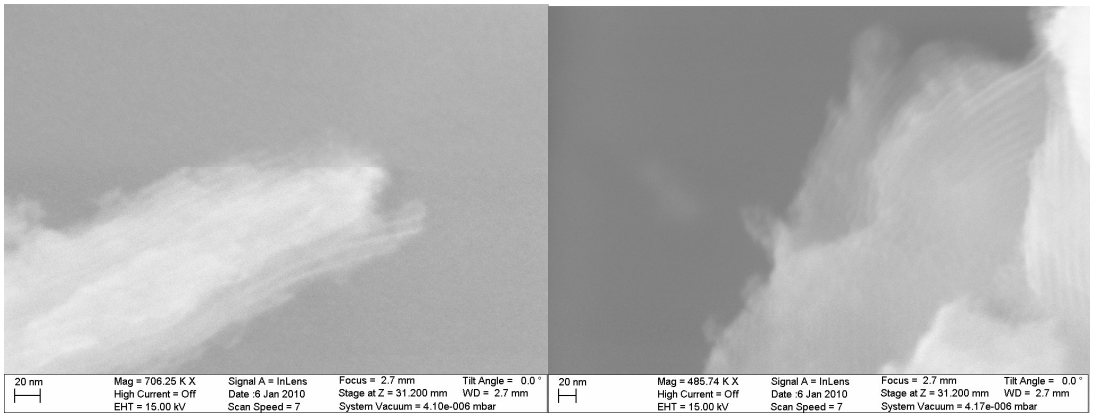

Figure 6.11 STEM images of sample S-6g

Figure 6.6 are the STEM images of sample S-28g, which have AB volume 466.67% of the total mesoporous volume of sample S-28, based on the neat AB density. Also AB are weakly scattering the electrons, there are still blur image of wires like structure growing out from mesoporous structures. Figure 6.7 is the STEM image of sample S-16g, which also shows AB wires grow out from the pore of the mesoporous silica. Figure 6.8 are the STEM images of sample S-14g and figure 6.9 are the STEM images of sample S-14. It is clear show that no wire like feature extends from the pores before AB is introduced in sample S-14, but the AB/MS

nanocomposites S-14g will have AB packed and grow out from the pores. The STEM image of sample S-11g and S-6 (figure6.10 and figure 6.11) also support the same conclusion.

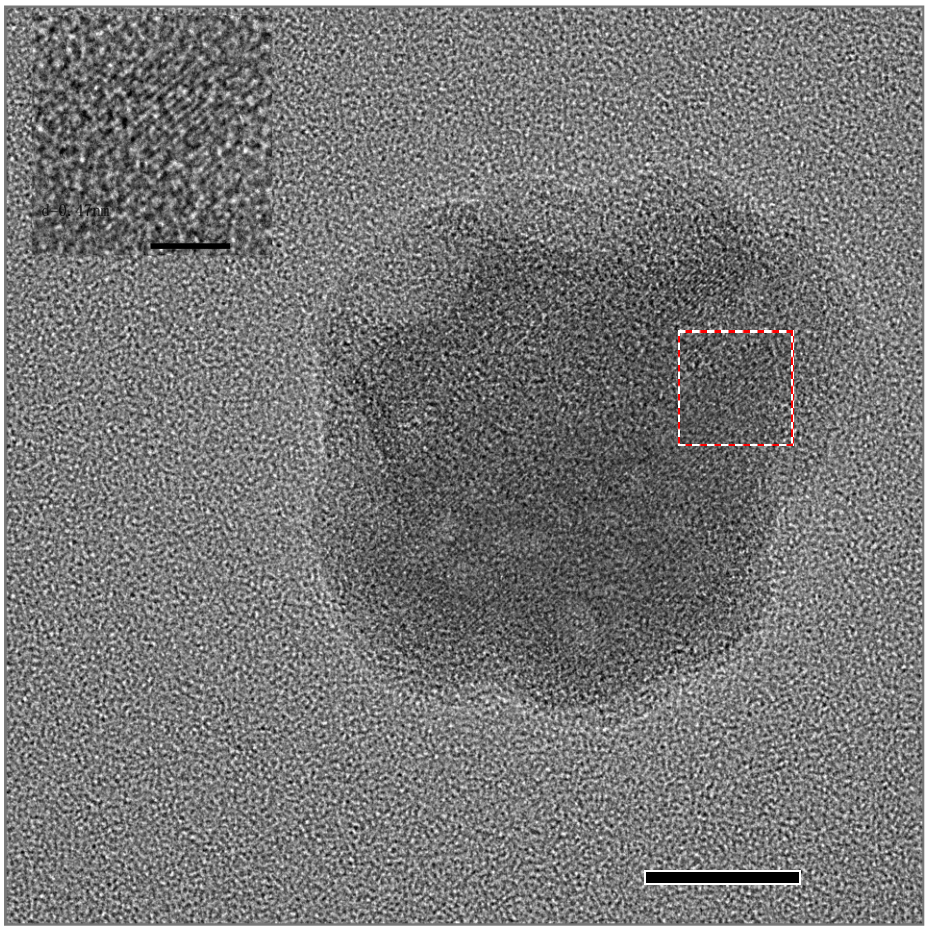

Figure 6.12 HRTEM image of sample S28-g

A further investigation is also done by high resolution TEM. Figure 6.12 is the HRTEM image of sample S28-g, which shows around 28nm pores on the sample and insert image is the enlarged pore structure. It is clearly shown that there are crystal feature in the pore, which is AB crystal grow in the pore and the size of the crystal are restricted by the pore wall.

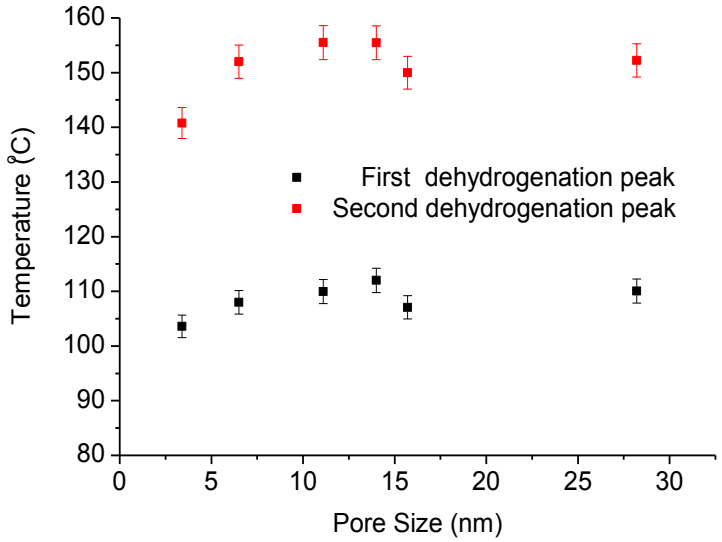

Figure 6.13. AB dehydrogenation peak of various pore sizes in growth stage

6.5 Conclusions

In summary, we discussed the pore size effect on the AB in mesoporous matrix. The three stages of AB loading is confirmed in different system with various pore size. And it is determined that the filling region is not depend on the pore size, but the surface loading level. In the filling region, we found that the melting point is disappear at pore size smaller than 11nm. And the first dehydrogenation is almost constant at pore size less than 28nm, while the second dehydrogenation is dependent linearly on the pore size

References

1. (a) Staubitz, A.; Robertson, A. P.; Manners, I., Ammonia-borane and related compounds as dihydrogen sources. *Chem Rev* **2010,** *110* (7), 4079-124; (b) Grochala, W.; Edwards, P., Thermal decomposition of the non-interstitial hydrides for the storage and production of hydrogen. *Chem Rev* **2004**, 1283-1315; (c) Smythe, N. C.; Gordon, J. C., Ammonia Borane as a Hydrogen Carrier: Dehydrogenation and Regeneration. *European Journal of Inorganic Chemistry* **2010,** (4), 509-521.

2. Frueh, S.; Kellett, R.; Mallery, C.; Molter, T.; Willis, W. S.; King'ondu, C.; Suib, S. L., Pyrolytic decomposition of ammonia borane to boron nitride. *Inorg Chem* **2011,** *50* (3), 783-92.

3. Gutowska, A.; Li, L.; Shin, Y.; Wang, C. M.; Li, X. S.; Linehan, J. C.; Smith, R. S.; Kay, B. D.; Schmid, B.; Shaw, W.; Gutowski, M.; Autrey, T., Nanoscaffold mediates hydrogen release and the reactivity of ammonia borane. *Angew Chem Int Ed Engl* **2005,** *44* (23), 3578-82.

4. (a) Bluhm, M. E.; Bradley, M. G.; Butterick, R., 3rd; Kusari, U.; Sneddon, L. G., Amineborane-based chemical hydrogen storage: enhanced ammonia borane dehydrogenation in ionic liquids. *J Am Chem Soc* **2006,** *128* (24), 7748-9; (b) Denney, M. C.; Pons, V.; Hebden, T. J.; Heinekey, D. M.; Goldberg, K. I., Efficient catalysis of ammonia borane dehydrogenation. *J Am Chem Soc* **2006,** *128* (37), 12048-9; (c) Keaton, R. J.; Blacquiere, J. M.; Baker, R. T., Base metal catalyzed dehydrogenation of ammonia-borane for chemical hydrogen storage. *J Am Chem Soc* **2007,** *129* (7), 1844-+; (d) Wu, H.; Zhou, W.; Yildirim, T., Alkali and alkaline-earth metal amidoboranes: structure, crystal chemistry, and hydrogen storage properties. *J Am Chem Soc* **2008,** *130* (44), 14834-9; (e) Zhao, Y.; Zhang, J.; Lee, J. W.; Akins, D. L. In *Promote hydrogen release from preheated ammonia boraneand spectroscopy study*, 241st American Chemical Society National Meeting, Anaheim, CA, Anaheim, CA, 2011; (f) Guo, Y.; He, X.; Li, Z. S.; Zou, Z. G., Theoretical Study on the Possibility of Using Frustrated Lewis Pairs as Bifunctional Metal-Free Dehydrogenation Catalysts of Ammonia Borane. *Inorg Chem* **2010,** *49* (7), 3419-3423.

5. (a) Wang, L. Q.; Karkamkar, A.; Autrey, T.; Exarhos, G. J., Hyperpolarized Xe-129 NMR Investigation of Ammonia Borane in Mesoporous Silica. *Journal of Physical Chemistry C* **2009,** *113* (16), 6485-6490; (b) Paolone, A.; Palumbo, O.; Rispoli, P.; Cantelli, R.; Autrey, T.;

Karkamkar, A., Absence of the Structural Phase Transition in Ammonia Borane Dispersed in Mesoporous Silica: Evidence of Novel Thermodynamic Properties. *Journal of Physical Chemistry C* **2009,** *113* (24), 10319-10321; (c) Zhao, Y.; Zhang, J.; Akins, D. L.; Lee, J. W., Effect of Composition on Dehydrogenation of Mesoporous Silica/Ammonia Borane Nanocomposites. *Industrial & Engineering Chemistry Research* **2011,** *50* (17), 10024-10028.

6. (a) Feaver, A.; Sepehri, S.; Shamberger, P.; Stowe, A.; Autrey, T.; Cao, G., Coherent carbon cryogel-ammonia borane nanocomposites for H2 storage. *J Phys Chem B* **2007,** *111* (26), 7469-72; (b) Sepehri, S.; Feaver, A.; Shaw, W. J.; Howard, C. J.; Zhang, Q.; Autrey, T.; Cao, G., Spectroscopic studies of dehydrogenation of ammonia borane in carbon cryogel. *J Phys Chem B* **2007,** *111* (51), 14285-9; (c) Sepehri, S.; Garcia, B. B.; Zhang, Q. F.; Cao, G. Z., Enhanced electrochemical and structural properties of carbon cryogels by surface chemistry alteration with boron and nitrogen. *Carbon* **2009,** *47* (6), 1436-1443; (d) Sepehri, S.; Garcia, B. B.; Cao, G. Z., Influence of Surface Chemistry on Dehydrogenation in Carbon Cryogel Ammonia Borane Nanocomposites. *European Journal of Inorganic Chemistry* **2009,** (5), 599-603.

7. Li, L.; Yao, X.; Sun, C. H.; Du, A. J.; Cheng, L. N.; Zhu, Z. H.; Yu, C. Z.; Zou, J.; Smith, S. C.; Wang, P.; Cheng, H. M.; Frost, R. L.; Lu, G. Q. M., Lithium-Catalyzed Dehydrogenation of Ammonia Borane within Mesoporous Carbon Framework for Chemical Hydrogen Storage. *Advanced Functional Materials* **2009,** *19* (2), 265-271.

8. Kim, H.; Karkamkar, A.; Autrey, T.; Chupas, P.; Proffen, T., Determination of structure and phase transition of light element nanocomposites in mesoporous silica: case study of NH3BH3 in MCM-41. *J Am Chem Soc* **2009,** *131* (38), 13749-55.

9. Cao, L.; Man, T.; Kruk, M., Synthesis of Ultra-Large-Pore SBA-15 Silica with Two-Dimensional Hexagonal Structure Using Triisopropylbenzene As Micelle Expander. *Chemistry of Materials* **2009,** *21* (6), 1144-1153.